Constitutive and Friction Characterization and Simulation of AA7075 Aluminum Alloy Sheet under Die Quenching Conditions

by

Raphael Boulis

A thesis
presented to the University of Waterloo
in fulfilment of the
thesis requirement for the degree of
Master of Applied Science
in
Mechanical and Mechatronics Engineering

Waterloo, Ontario, Canada, 2022

Author's Declaration

I hereby declare that I am the sole author of this thesis. This is a true copy of the thesis, including any required final revisions, as accepted by my examiners. I understand that my thesis may be made electronically available to the public.

Abstract

This thesis investigates the die quench forming of AA7075 aluminum alloy sheet, including the constitutive and friction behaviour at elevated temperatures. Experiments examining characterization of friction behaviour and models to simulate sheet forming were developed for conditions corresponding to the die quench thermal process window, comprising solutionizing of the material at 480ºC, followed by simultaneous forming and quenching in a cooled die.

A modified version of the temperature- and rate-dependent Zerilli-Armstrong model [136] was developed and calibrated as part of this work. This model was fit to die quench material characterization data for AA7075 from two sources, due to Omer *et al.* [54] and Wang *et al.* [119], designated the Omer-fit and Wang-fit models, respectively. Both models captured the measured constitutive data relatively well, with the worst fit condition for the Omer-fit corresponding to the 470°C, 0.1 s^{-1} test with an R^2 value of 0.7798, whereas the worst case for the Wang-fit was the 400°C, 0.1 s^{-1} test condition with an R^2 value of 0.8992. All other tests conditions exhibited R^2 values closer to unity.

A numerical model of tensile testing under DQ conditions was developed using the tensile geometry from Wang *et al.* [119] in conjunction with the Omer-fit to perform a direct comparison between the Omer *et al.* [54] and Wang *et al.* [119] material characterization data. The tensile model using the Omer-fit predicted a significantly higher hardening response when compared to experimental measurements by Wang *et al.* [119].

A numerical model of limiting dome height (LDH) experiments, performed under DQ conditions by George *et al.* [130], was developed to assess the constitutive models comprising the Omer- and Wang-fits. The Wang-fit demonstrated accurate load-displacement and strain path predictions with slight over-softening at high forming strokes. The Omer-fit model demonstrated

significant overprediction of the loads, while having accurate predictions for the strain path at lower displacement. The predicted thermal history and temperature distributions reveal a significant temperature differential within the formed part between the centre of the punch (colder) and the unsupported region (hotter) between the punch and die for the 25.4 mm and 76.2 mm wide specimens. The temperature differential resulted in these specimens localizing within the hotter unsupported region. The 152.4 mm wide specimen also exhibited a temperature differential, making the unsupported region the hottest part of the specimen. However, for this geometry the unsupported region encompasses the full circumference of the punch. This lowers the stress in the unsupported region, forcing strain localization to the punch tip.

Under DQ test conditions, an average steady-state coefficient of friction (COF) of 0.02 for the Fuchs Forge Ease AL278 lubricant versus 0.15 for the Boron Nitride was obtained in the Twist Compression Test (TCT). The Renoform 10 [90] experienced early breakdown while the Renoform 25 [117] experienced gradual breakdown for the DQ test conditions. For experiments using tooling pre-heated to 200ºC, all lubricants experienced breakdown in at least two of three repeats, except for the Fuchs AL278, which experienced an average steady state COF of 0.015.

The Fuchs AL 278 was tested with DLC coated cups at various tooling temperatures. The addition of the DLC coating was found to increase the COF for room temperature tooling to 0.059, however, at 200 and 300ºC tooling temperatures the addition of DLC was found to decrease the COF. At a tooling temperature of 350°C, breakdown of the DLC coating starts to occur.

Acknowledgements

First and foremost, I would like to thank God for always standing by my side. “But those who wait on the Lord shall renew their strength; they shall mount up with wings like eagles, they shall run and not be weary, they shall walk and not faint.” (Isaiah 40:31)

Secondly, I would like to express my gratitude to Professor Michael Worswick for giving me this amazing opportunity to be part of the team and work on this interesting research project. His dedication to his students, attention to detail and enthusiasm, patience are unparalleled given his important role as University Research Chair.

Special thanks to Sante DiCecco, Ryan George and Kenneth Cheong for performing the experimental high temperature LDH testing, which was used for validating the numerical forming model.

Special thanks to Eckhard Budziarek, one of the most resourceful, hard working and patient laboratory technicians any graduate student can ask for. Thank you for all the help you provided to me and all the long hours spent troubleshooting.

I would like to also thank Tom Gawel, Neil Griffett, Andy Barber and Richard Gordon for their eagerness to help and all the advice they have given me in their respective fields.

Our machine shop has provided me great support and accommodated all my rush orders, thank you Mark Kuntz and all the guys at the machine shop for all the machining advice and willingness to help.

Special thanks to Dr. Jaqueline Noder for numerical modeling help and coaching. Your encouraging words, honest advice and overall expertise has surely helped my performance to excel.

The support of our sponsors, Honda R&D Americas LLC, Arconic Ground Transportation Group, and Promatek Research Centre, the Natural Sciences and Engineering Research Council (NSERC), the Canada Foundation for Innovation, the Ontario Advanced Manufacturing Consortium (AMC) and the Canada Research Chairs Secretariat, is profoundly appreciated.

Thank you to all the other graduate students and research engineers, specifically Hossein Pishyar Cameron Jeffery Tolton, Matthew Tummers, Pedram Samadian, Amir Zhumagulov and Chi-Hsiang Liao.

Je voudrais remercier ma mère Dalia Boulis (Beng) pour son support émotionnelle et logistique, tu es véritablement la seule personne qui ma guider à travers chaque défi.

Lastly, I would like to thank one of the smartest men I know, my father Eugene Boulis (BSc, MSc) a true inspiration and one that would make any son proud.

Table of Contents

List of Figures

List of Tables

List of Abbreviations

ARM	Area reduction method
CVD	Chemical vapour deposition
COF	Coefficient of Friction
DAQ	Data acquisition (system)
DOF	Degrees of freedom
DLC	Diamond like carbon
DQ	Die quench
DIC	Digital image correlation
FE	Finite Element
FEM	Finite Element Method
FLC	Forming limit curve
FLD	Forming limit diagram
GHGE	Greenhouse gas emission
GPI, GPII	Guinier-Preston zones
HTC	Heat transfer coefficient
LDH	Limiting Dome Height (test)
PLC	Portevin–Le Chatelier
PVD	Physical vapour deposition
HRC	Rockwell C Hardness
RD	Rolling direction
SHT	Solution heat treatment
SSSS	Supersaturated solid solution
TD	Thermoreactive diffussion
TTP	Time temperature property
TD	Transverse direction
TCT	Twist compression test
UTS	Ultimate tensile strength
VRC	Vacancy rich clusters
VH	Vickers Hardness

List of Symbols

A_{ap}	Apparent contact area
P	Contact pressure
T_{cr}	Critical temperature
C'_{AB}	Curvature evolution along line A-B
$D_{1, 2, 3}$	Deformation rate tensor eigen values
ε_{eng}	Engineering strain
σ_{eng}	Engineering stress
F_{draw}	Draw force
T_f	Flash temperature
σ	Flow stress
F_f	Force of Friction
H	Hardness of the softer material
r_0, r_{45}, r_{90}	Lankford coefficients along rolled sheet 0, 45 and 90° directions
ε_1	Major strain
$\dot{\varepsilon_1}$	Major strain rate
r_m	Mean radius of the test cup
MSR_{AB}	Mean square root error of curvature
ε_2	Minor strain
s	Shear strength of the softer material
$\dot{\varepsilon}_1^A$	Strain rate at the border of the neck region
F_N	Normal force
ε_p	Plastic strain
T	Resistance torque
ε_3	Thickness strain
ε_{total}	Total elongation
ε_T	True strain
σ_T	True stress
σ_θ	True stress in any direction in the plane of the material
$\sigma_{0°}$	True stress in the sheet rolling (0º)

σ_y	Yield Stress

1 Introduction

1.1 Motivation

Greenhouse gas emission (GHGE) reduction is an ongoing goal for many governments around the world. In Canada, as well as in the USA, vehicle manufacturers are expected to comply with progressively stringent GHGE targets across their fleet of vehicles. The target values are measured based on the footprint of the vehicle (Eq. 1). Figure 1 presents the target values in g of CO_2 per mile for a given passenger vehicle footprint in m^2 (ft^2) for the years 2011, 2016, and 2025 [1].

$$Footprint = \frac{front\ track\ width + rear\ track\ width}{2} \times wheelbase \quad \text{(Eq. 1)}$$

With an average footprint of 4.23 m^2 (45.5 ft^2) for all relevant (high volume) vehicles manufactured in 2017, it is clear (Figure 1) that the average CO_2 emission level must stay below 90 [MW1] g CO_2/km (145 g CO_2/mile) for a given manufacturer to comply with the 2025 target levels. This requires an approximately 4% annual reduction in CO_2 emissions. The European Union has very similar goals for GHGE.

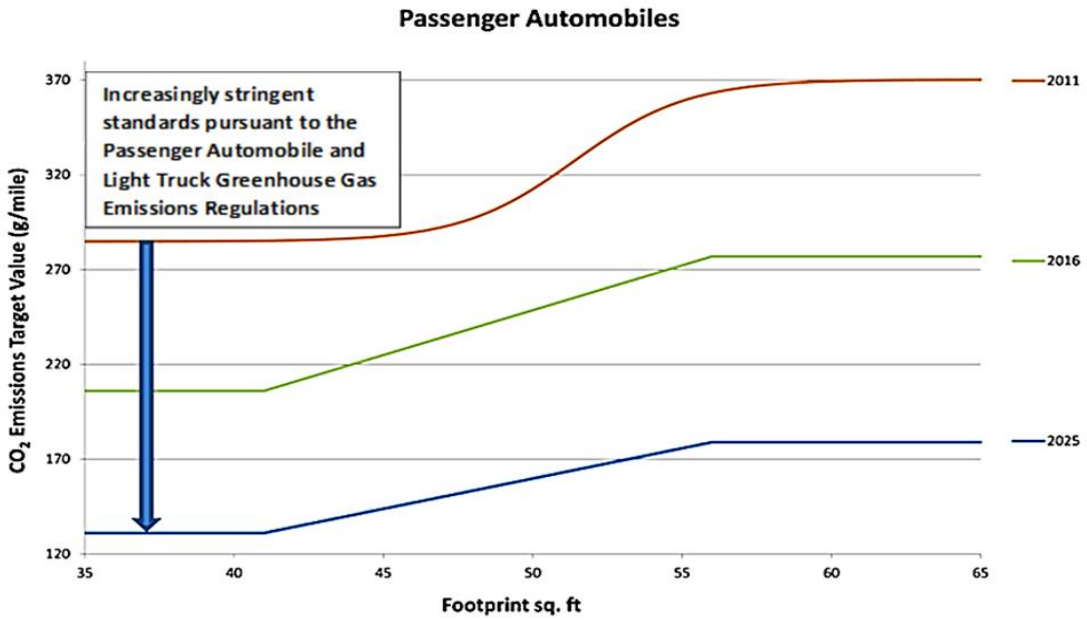

Figure 1: CO2 emission target values (g/mile) vs. passenger vehicle footprint (sq. ft.) [1]

The EUCO27 and EUCO30 are two central scenarios developed by the October 2014 European Council to reach 2030 targets, these targets include reaching CO_2 emissions of 75 g CO_2/km (120.75 g CO_2/mile) under EUCO27 and 70 g CO_2/km (112.7 g CO_2/mile) under EUCO30 for passenger vehicles [2]. These increasingly strict regulations demand a high level of innovation and ingenuity from vehicle manufacturers to meet these targets. Automotive weight reduction or lightweighting is one of the most effective methods to increase fuel economy and reduce emissions for a given vehicle footprint [107-109]. Automotive lightweighting can be achieved by utilizing alloys with high specific strength (high strength and low density) for vehicle structures. Aluminum high strength alloys are good potential candidates for this lightweighting objective; however, they tend to have lower ductility and are difficult to form at room temperature. To overcome this limitation, high strength aluminum alloys can be formed more easily at higher temperatures using the die quench process, a non-isothermal forming process. This thesis aims to develop numerical simulation techniques to model the die quench forming process for high strength AA7075 aluminum alloy sheet metal for vehicle body-in-white applications.

1.2 Background

Automotive lightweighting is achieved primarily using materials that offer a high strength to weight ratio. The mass of a vehicle body structure can be reduced by 40% or more by utilizing high-performance sheet metals such as high strength aluminum alloys [3]. Among these materials are the 6000- and 7000-series high strength aluminum alloys, which have seen extensive use in the aerospace industry [4]. Unlike mild steels, aluminum alloys have limited formability at room temperature [5-7]. For this reason, the aerospace industry utilizes forming techniques such as superplastic forming to help increase their formability. Superplastic forming for aluminum is executed by heating the blank to about 470-520°C inside a female die, after which inert gas is pressurized and used to progressively force the blank onto the female die, slowly taking its shape [8]. While this process has its advantages, such as an excellent surface finish, high accuracy and virtually no spring back due to annealing during forming, it is, however, very time consuming and only feasible for low-volume production [9]. One of the more recent high-volume forming techniques gaining traction is warm forming. Warm forming is a process that involves heating the blank to an intermediate temperature (about 150-300°C) and isothermally forming the material. Figure 2 shows forming limit curves (the locus of limit major strain at necking during forming as a function of minor strain) for a range of forming temperatures for AA5182. It is evident from the figure that warm forming can only offer good formability gains as compared to room temperature forming [10]. An improvement of approximately 69% relative to room temperature is seen at 260°C. When applied to precipitation hardening alloys (*e.g.* 6000- and 7000-series alloys), it is important to note that warm forming conditions takes place at an intermediate temperature (150-230°C), the precipitates in the material are largely undissolved. Therefore, formability gains using this forming process will be dependent on the as-received material temper.

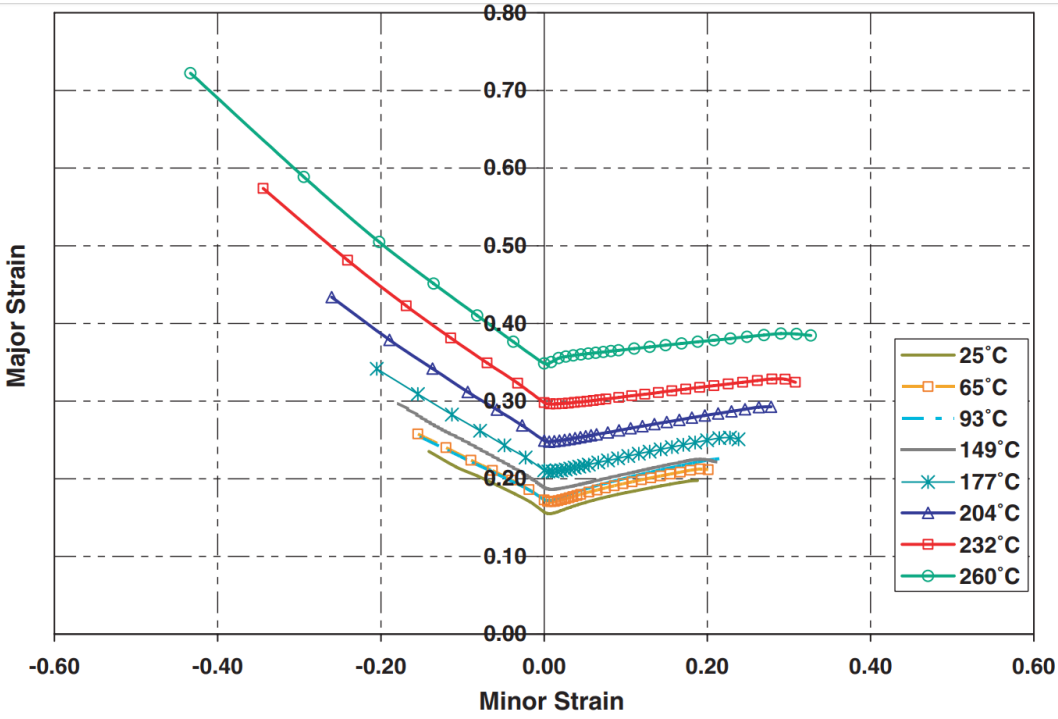

Figure 2: AA5182-O temperature dependent FLD [10]

1.3 Die Quench Forming Processes

Hot stamping or die quenching (DQ) has long been used to manufacture steel body structural members for automotive applications and is well documented [11-13]. The steel DQ process offers a high degree of formability combined with a relatively short process time [6]. This process is illustrated in Figure 3. For steel, the process starts by heating the blank to the austenitic temperature (normally around 920-930 °C) and holding it at temperature until the material is homogenized. At this point, the material is quickly transferred to the forming die, which is at room temperature, in which it is simultaneously formed and quenched making this a non-isothermal forming process.

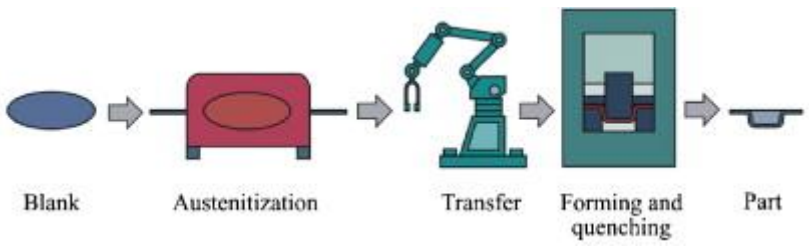

Figure 3: Hot stamping process [13]

A somewhat similar process can be conducted for aluminum alloys and the DQ time-temperature history used for DQ processing of heat treatable aluminum alloys is shown in Figure 4. This process was first introduced by Lin *et. al.* [123-126]. The process begins with the solution heat treatment (SHT) of the blank in the temperature range of 470-560 °C, depending upon the alloy. During solution treatment, the precipitates present in the matrix are dissolved and the material is reduced to a single phase. SHT nullifies the initial temper of the as-received material and increases ductility by dissolving dislocation-impeding precipitates and reducing the elastic modulus due to the elevated temperature [14-16, 9]. Following SHT, the blank is quickly transferred to the die, which is at room temperature; during this time, the material loses some heat. The blank is then formed and simultaneously quenched in the die. If quenching is performed at an adequate rate, the material enters a supersaturated solid solution (SSSS) state, for which it has a very high driving force for precipitation [17-19]. Heat treatable alloys have the potential to regain their strength post-quench through natural (room temperature) and/or artificial ageing (elevated temperature). The ageing process is performed to promote the nucleation of precipitates that strengthen the material and achieve the desired temper [20].

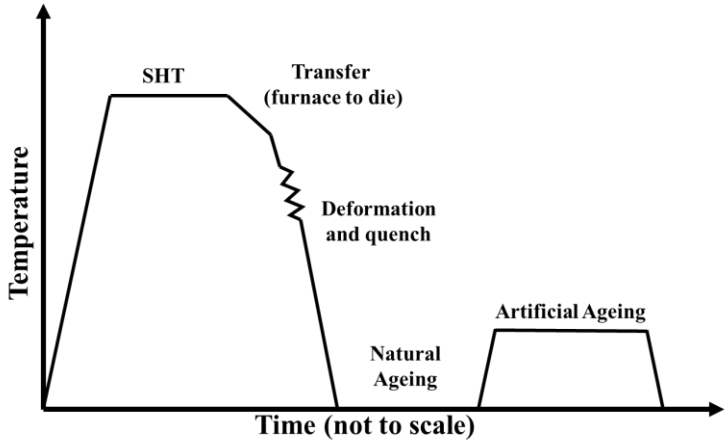

Figure 4: Die quenching thermal cycle diagram

The DQ process for heat treatable aluminum alloys has several process parameters that must be characterized and controlled, to ensure the integrity of the formed parts. These parameters are:

- SHT time
- SHT temperature
- Transfer time
- Quench rate
- Ageing schedule

The optimum SHT temperatures for many 6000- and 7000-series aluminum alloys have well documented standards [21-23]. Typically, this temperature is below the melting point of aluminum but above the solvus temperature of all precipitates that are present in the given alloy system. The optimal SHT temperature for AA7075 is 470°C [23], on the other hand, for AA6013 it is 560°C [23]. The temperature for AA6013 is higher since the solvus temperature for the equilibrium beta phase, composed of Mg_2Si, is around 530°C, and this precipitate is not present in AA7075 due to the lack of Si [24-25].

Regarding the SHT time, the available published data varies considerably, some publications suggest a time of 5 to 10 min [6-7, 14, 26], others advocate around 30 min [9, 27], and some go as far as 60 or 100 min [28-29]. A parametric study performed by Omer et al. [30], based on measured hardness after quenching following various SHT durations, reported that the minimum SHT time for AA7075 is 8 min at the SHT temperature. This finding was consistent with previous work by Boulis et al. [31]. The determination of minimum SHT time is very important since it reduces the processing time, which in turn reduces cost.

1.3.1 Transfer Time

The transfer time can be a critical parameter when designing a hot stamping operation; this is especially true for quench sensitive heat treatable alloys. Figure 5 shows the time temperature property (TTP) curves for some 7000-series aluminum alloys. In general, TTP curves are used to

indicate the critical time available before precipitation starts to take place at any specific temperature. From these isothermal curves, it can be observed that for almost all alloys (except AA7055) the transfer time is not critical if the material does not cool excessively below 400°C prior to quenching [32]. This prevents diffusion driven quench-induced precipitation from occurring during transfer of the blank from the furnace to the die [33].

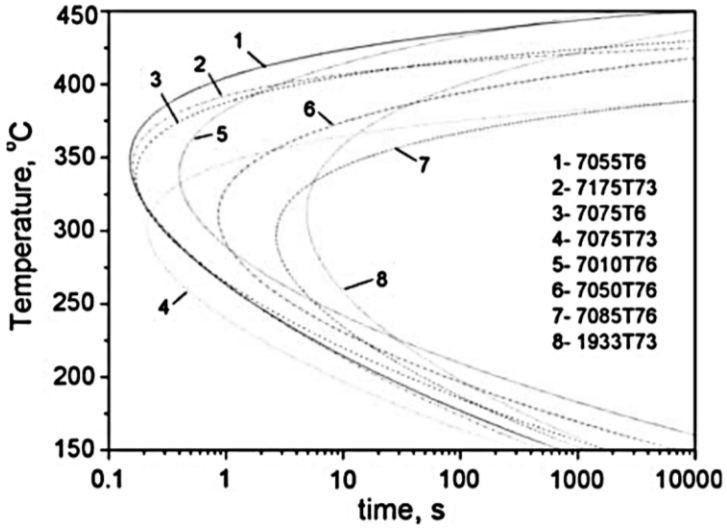

Figure 5: TTP for Al-Zn-Mg-Cu alloys [32]

1.3.2 Quench Sensitivity

The alloys shown in Figure 5 are numbered in sequence according to their level of quench sensitivity, with 7055 being the most quench sensitive. In general, the more quench sensitive an alloy is, the closer the nose of the TTP curve is to the ordinate axis. Figure 5 also helps to highlight the critical cooling rate needed to avoid quench-induced precipitation for each alloy. Quench-induced precipitation typically results in precipitation of the equilibrium phase of a material system [25]. The equilibrium phase is not a strengthening phase and the more of it formed during quenching, the lower the level of supersaturation in the material post-quench [34-36]. This reduction in supersaturation reduces the potential for strengthening during subsequent ageing heat treatments since it depletes the solutes available in the matrix for precipitation of the strengthening

phase. Omer *et al.* [30] identified the critical cooling rate for several alloys, including AA7075, which was 50°C/s [54]. This characterization was done experimentally by attaching a thermocouple to a piece of sheet metal and quenching it using flat dies. In a real forming operation, however, it is very difficult to know the local cooling rate, given that the cooling rate is primarily a function of contact pressure, which can vary considerably within a complex component. For this reason, accurate modeling of the part must be performed to identify areas with critically low cooling rates; this approach will be shown in Chapter 2 of this work.

1.3.3 Ageing

After a blank is SHT and then formed and die quenched, it will be in a SSSS state. Artificial ageing is performed to regain the strength that was lost due to SHT. The precipitation sequence for a 7000-series aluminum alloy is as follows:

$$\text{SSSS} \rightarrow \text{VRC} \rightarrow \text{GPI and GPII zones} \rightarrow \eta' \rightarrow \eta \text{ [37]}$$

in which VRC are vacancy rich clusters that form during quenching, GPI and GPII zones stand for Guinier-Preston zones which are a metastable, coherent strengthening phase, η' is another metastable strengthening phase which is semi coherent in nature and η is the equilibrium phase which results in coarsening of the material and is incoherent [38-39]. Coherency of precipitates refers to the extent to which the lattice of the precipitate matches the lattice of the matrix material, the higher the similarity in the lattices, the lower the interfacial free energy. For automotive body structure application, the goal is often to achieve a peak age T6 strength or the highest strength possible post ageing [7, 40]. A T6 temper is typically characterized by the presence of GPI and GPII zones as well as η' phase [37]. Andreatta *et al.* [41] as well as Jegdić, and Bobby [42-43] have shown that the corrosion behaviour of 7000-series alloys is dependent on microstructure,

which is susceptible to change during heat treatment. Therefore, for better corrosion resistance and paintability, Andreatta *et al.* has showed that a T76 temper is desired, since it is less susceptible to exfoliation corrosion. The T76 temper is a slightly overaged condition; for AA7075, the main phases present for this temper are the strengthening η' phase as well as the equilibrium η phase [41]. Many ageing schedules are available to achieve a T76 temper with varying degrees of over-ageing. As for T6, the usual schedule for most 7000-series aluminum alloys is 120°C for 24 hr [28, 44-45], however, proprietary ageing schedules are also thought to exist.

1.4 Finite Element Simulation of the DQ Forming Process

At the heart of every finite element (FE) forming simulation lies the constitutive model, which predicts material mechanical behaviour during forming A complete constitutive model should capture the material stress-strain behavior under the conditions experienced during the given process. The DQ process for aluminum alloys requires a constitutive model that captures strain rate dependency, temperature effects and material anisotropy. The model should also capture the interplay between these parameters. To do this successfully, tensile tests performed to characterize material properties should accurately mimic the real forming process parameters.

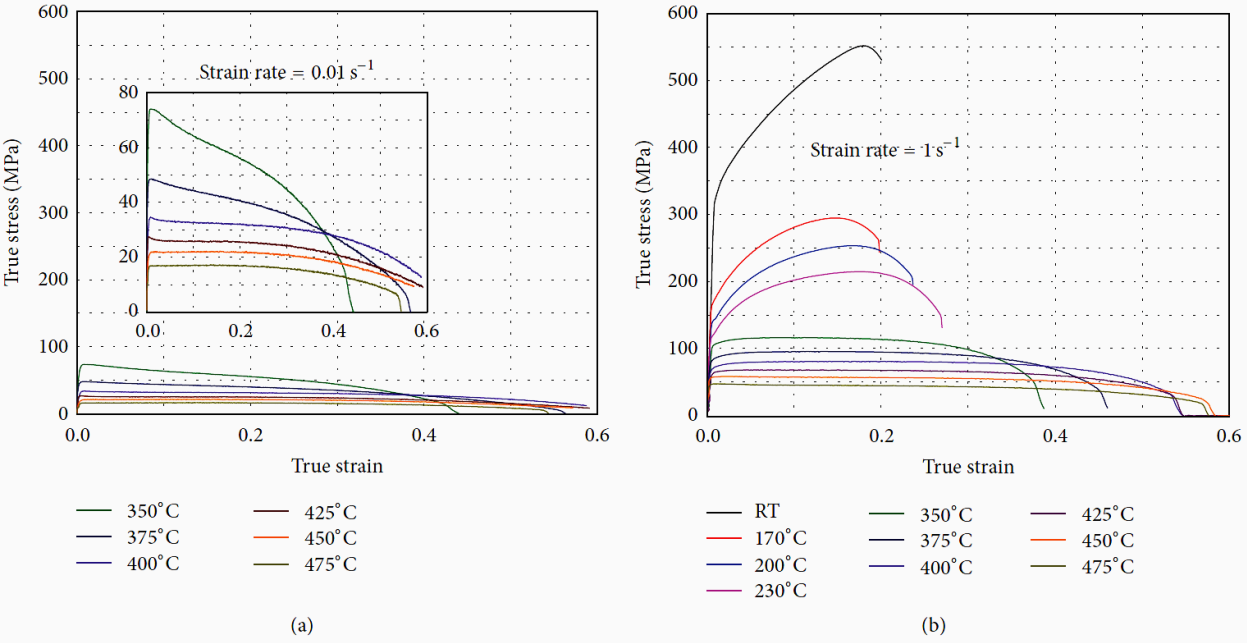

Figure 6: Hot flow curves of AA7921-T4 a) different strain rates b) different temperatures [46]

Figure 6 from Kumar *et al.* [46], displays the general trends expected for temperature and strain rate effects on stress-strain behaviour. In general, there is a decrease in the flow stress and an increase in total elongation with increasing temperature. A decrease in the total elongation and an increase in the flow stress with an increase in the strain rate. The latter trends are however amplified in the lower temperature regime (*i.e.* RT to 230°C). The trends in Figure 6 serve to highlight the advantages of the DQ process over warm forming; forming at a higher temperature requires a lower forming force (as temperature increases the average stress level drops) and results in higher formability (higher elongation prior to fracture).

As often seen in literature, tensile tests to characterize mechanical properties during hot stamping applications are performed in the same fashion as in a warm forming application. That is, the tensile test specimen is heated to a certain temperature and then tested at that temperature, as was the case for the data in Figure 6. In the study by Kumar *et al.* [46], as well as work by Zang *et al.*

[47] Wang *et al*. [48] and Beland *et al.* [49], the full thermo-mechanical history of the material was not accounted for. In the real DQ process the material is SHT and then quenched which results in a SSSS material, however the processing history considered in [46-49] do not consider a SHT condition nor was the material quenched immediately prior to testing. Depending on the temper of the as-received material, certain precipitates may not be dissolved prior to deformation at temperatures lower than SHT temperature. In addition, SHT has other effects on the material such as an increase in vacancies, which will certainly affect the stress-strain behavior [50-52]. Generally, the lack of super saturation post-forming will greatly affect a material's age hardening potential.

Another shortcoming in the literature [49, 52-53] is the conversion of engineering stress-strain to true stress-strain by using equations 2 and 3 past the necking point.

$$\varepsilon_T = \ln(1 + \varepsilon_{eng}) \text{ (Eq. 2)}$$

$$\sigma_T = \sigma_{eng} \times \ln(1 + \varepsilon_{eng}) \text{ (Eq. 3)}$$

These equations are only true when volume constancy applies, which is up to the necking point. The usage of these equations past the necking point will result in a negative hardening response, as seen in Figure 6. At elevated temperature, the onset of localized necking takes place at very low levels of plastic strain 3-4% [54] therefore, a better approach is needed to compute the true stress-strain at these temperatures.

There are some publications [9, 55] on constitutive modeling of 6000-series aluminum alloys, which do account for SHT as well as quenching effects on their tensile behaviour. These studies consider solutionizing the material, quenching to an intermediate temperature (350-525°C), and isothermally forming the part. Although, quenching and forming are not done simultaneously, as

in the real forming operation, forming isothermally results in better experimental control and ease of model fitting and implementation in FE software. However, the quench rate considered by Liu *et al.* [55] is 20°C/s, which is too low and could possibly result in formation of equilibrium phase precipitates during tensile testing which would affect the mechanical behavior. As for Delghani *et al.* [39], the quench rate was not mentioned. In addition, the studies by Mohammed *et al.* [9] and Liu *et al.* [55] only tested the mechanical behavior for a limited number of temperatures (*i.e.* 3-4); this limitation means the software must interpolate to capture the behavior in-between the temperatures tested, resulting in potential inaccuracies in the predicted constitutive behavior. More importantly, both studies did use equations 2 and 3 to compute their true stress-strain past the necking point which would likely result in errors.

In the study by Liu *et al.* [55], a Cowper-Symonds [136] material model was used, which was implemented in FE software and provided accurate predictions for the neck location when forming a B-pillar. Figure 7 presents a comparison between the FE simulation and the actual formed part. The model identifies areas where rapid cooling occurs which locally reduces the ductility of the material, the reduced ductility results in fracture initiation in those areas. When comparing the FE model to the formed part, it is clear that the locations that exhibited rapid cooling in the FE model are the same locations where fracture occurred in the real part are. In addition, Liu *et al.* [55] found that friction played a major role in thinning prediction. Therefore, accurate friction characterization must be implemented to better model the forming process. This topic will be discussed in detail later in this chapter.

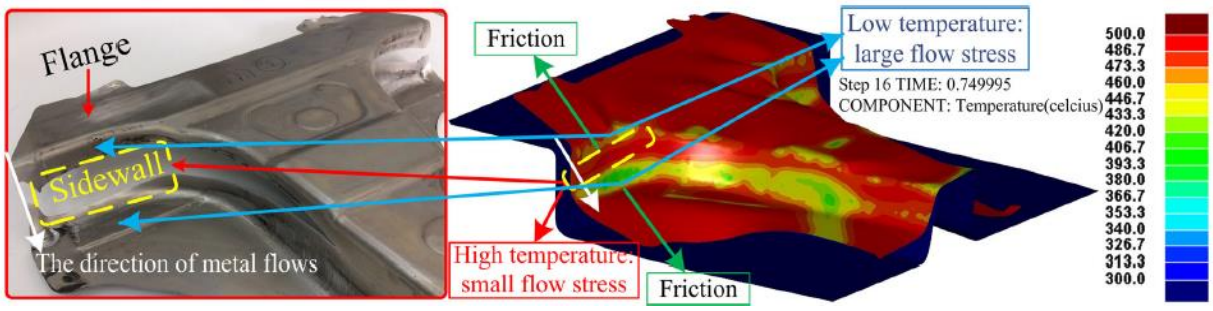

Figure 7: Crack mechanism in hot stamping without lubrication comparing the actual formed part (on the left) and simulation (on the right) [55]

Studies considering accurate constitutive characterization of 7000-series aluminum alloys for DQ application are very limited. Xiao *et al.* [14] accounted for SHT and quench effects in their study and developed a unified dislocation-driven material model coupled with a multiaxial continuum damage mechanics model for AA7075. However, the plasticity model in this work failed to accurately capture stress-strain behavior at higher temperatures (500 and 525°C) and plastic strains beyond 0.6. Past a plastic strain of 0.6, the damage model helped to capture the stress-strain behavior more accurately. Omer *et al.* [54] characterized two 7000-series aluminum alloys subjected to hot forming. In their paper, SHT was carried out on all tensile specimens, which were quenched at a rate of at least 56°C/s to the desired testing temperature and then tested. The constitutive model used in this work consisted of a Modified Voce hardening model and a Barlat YLD 2000 [121] yield surface (Figure 8). This paper also introduced a novel area reduction method (ARM) that captures localized necking by computing the instantaneous area of the tensile specimen using digital image correlation (DIC) technology. Using the ARM the true stress *vs.* true strain can be calculated post-necking, often resulting in a positive hardening response. The Modified Voce model, in conjunction with the ARM, captured the stress-strain behaviour reasonably accurately at most elevated temperatures as well as at room temperature.

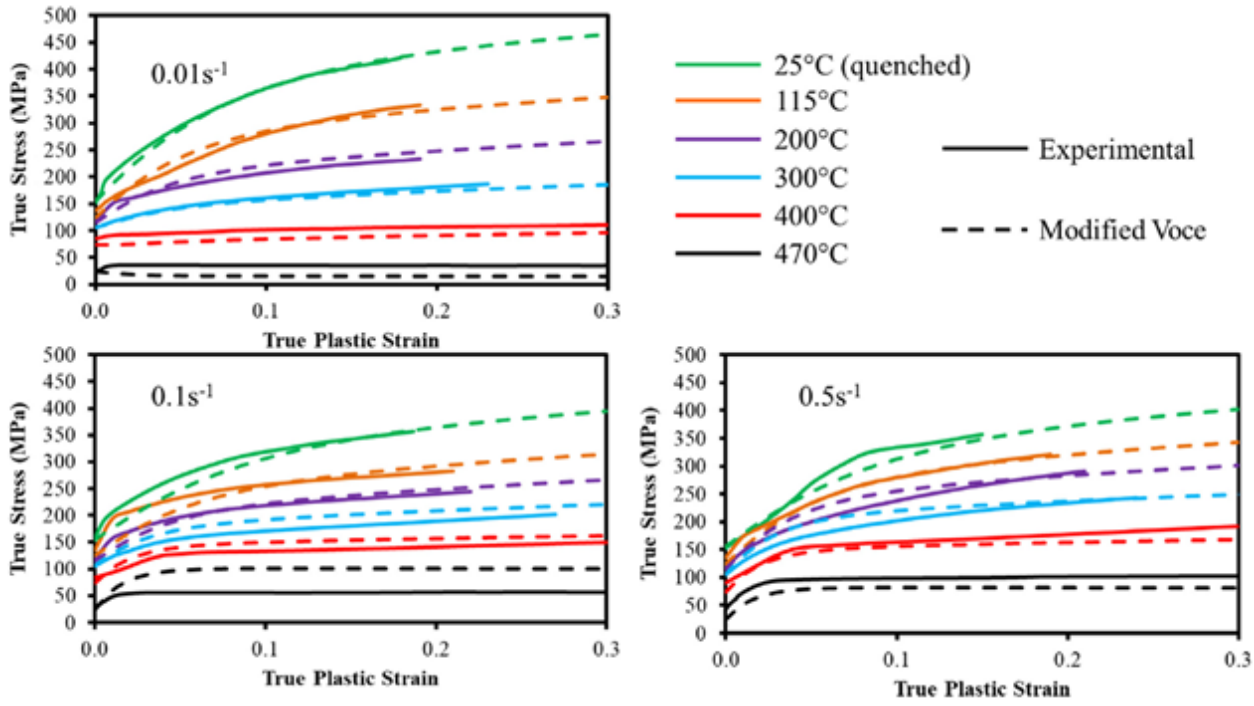

Figure 8: AA7075 Flow curves for strain rates: 0.01, 0.1 and 0.5 s^{-1} and temperatures: 25, 115, 200, 300, 400 and 470°C with a modified Voce curve fit [54]

As an alternative to ARM, Rahman *et al.* [56] have shown that a shear stress-strain data can be used to extend the measured stress-strain response beyond the point of localized necking seen in a uniaxial tension test. The shear specimen in that study [56] was adopted from Peirs *et al.* [57-59]; this specimen geometry forces the material to deform under simple shear conditions up to fracture, thereby supressing necking. If necking is supressed, the true stress-strain can be obtained very easily for large values of plastic strain. Since, the stress ratios (ratio between true stress in the sheet rolling (0º) direction *vs.* true stress in any direction in the plane of the material) for most commercially available aluminum alloys such as AA7075 maintain a fairly constant value as the material hardness (*i.e.* $\frac{d(\frac{\sigma_{0^\circ}}{\sigma_\theta})}{d\varepsilon} \approx 0$). This isotropic shear assumption was demonstrated by Omer *et al.* [54] and Rahman *et al.* [56]. Therefore, the shear stress-strain response can be converted to true stress-strain response seen in unixial tension by virtue of plastic work equivalence.

1.5 Formability

Formability characterization provides an important design tool for effective selection of forming process parameters. The specimen geometries used for formability testing, according to the ISO12004-2:2008 [107] standard, are designed to selectively achieve a certain strain path at the necking point. When the forming limit curve (FLC) is plotted in "in-plane principal strain space", the figure is referred to as a forming limit diagram (FLD). The major and minor strain values prior to instability (necking) for any specimen geometry are plotted as a point on the FLC. Figure 9 shows an FLD in which a number of different strain paths are labled, along with a schematic representation of the specimen geometries required to achieve them. This diagram for a given material becomes an effective tool to use when analyzing sheet formability,

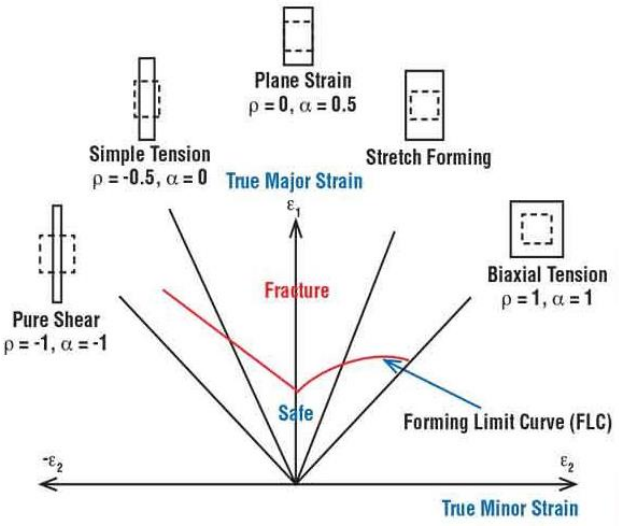

Figure 9: FLC schematic [60]

The strain exibited during formability testing is obtained by analyzing the geometrical changes in a given test specimen; this can be achieved in multiple ways with differing levels of accuracy. Traditionally the strain was obtained with the help of circular [61- 63] or square grids [64] etched on the test specimen, which would alter geometrically during deformation. The deformed grid

would then be compared to the original geometry and thus the logarithmic strain can be determined. The etched grid approach allows for the strain to be measured once post-fracture, unless inturrupted testing (test is stopped at specific times) is conducted; consequently, these methods tend to have lower accuracy and do not reveal changes in strain path during deformation. Digital image correlation (DIC) is the most common current approach for analyzing the strain field in a laboratory setting. DIC analysis utilizes a stereoscopic camera system making full-field 3D image analysis possible [65]. Typically, specimens are painted white in the gauge region, followed by a layer of random black speckles. The image analysis software then tracks the relative movement of every speckle to compute the logarithmic strain. Thus, DIC analysis provides the full strain history of the specimen as opposed to a single strain value at fracture, which also allows for a higher level of accuracy and the possibility of computing the strain path and strain rate history. The latter becomes very useful when exploring different forming limit detection methods.

1.5.1 Forming Limit Detection

One of the most important topics with regard to formability characterization is the criteria used to define the forming limit or initiation of necking. One of the first methods used to determine the forming limit is the ISO 12004-2 parabolic fit method. This method records strain values on either side of a crack along line slices oriented perpendicular to the crack. While omitting strain values directly adjacent to the crack, the major and minor strain *vs.* location on the specimen are fit using a parabolic curve. The peak value of the parabolic fit is then used to deduce the forming limit strain value at the neck location, as illustrated in Figure 10.

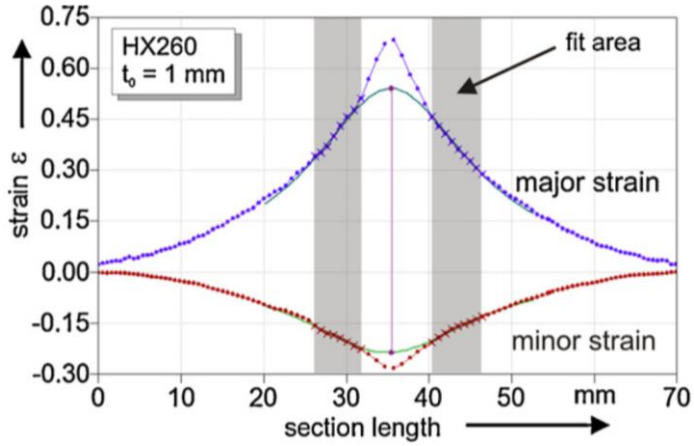

Figure 10: ISO 12004-2 parabolic fit for limit strain determination for HX260 steel with 1 mm sheet thickness [106]

One of the issues with the ISO method is that the forming limit strain measurement is done post-fracture and not *in situ* during the test. However, with the arrival of DIC technology, *in situ* strain measurements are possible, thus allowing for more complex and accurate methods of necking or forming limit detection. There are many other approaches found in the literature that tackle this issue. Some are based on strain rate or thinning rate stability, as proposed by Volk *et al.* [66]. Other approaches use local curvature evolution as an indicator of necking onset (DiCecco *et al.* [127-128], Wang *et al.* [67]), or predictive techniques, which utilize test data to create an empirical or numerical model that can predict limit strains, as proposed by Danckert *et al.*[62], Swift *et al.* [68] and Hora *et al*. [69-70].

Volk *et al.* [66] developed a time dependent method for identifying the point of instability, in which the onset of increased rate of thinning of the sheet material is adopted as an indicator of instability. The thinning rate is defined by equation 4 in which $D_{1,2,3}$ are the eigen values of the deformation rate tensor D_{ij}.

$$\dot{\varepsilon} = |D_3| = -(D_1 + D_2) \text{ (Eq. 4)}$$

As the sheet metal starts to neck, the through-thickness strain rate increases dramatically [66]. Figure 11 displays the thinning rate as a function of the frequency of DIC data acquisition. It is noticeable that the thinning rate increases dramatically past the 23rd DIC image at a constant rate; meanwhile prior to this, the thinning rate is very modest but again remains approximately constant. The onset of instability is taken as the intercept of two straight lines fit to the thinning data, as seen in the Figure 11.

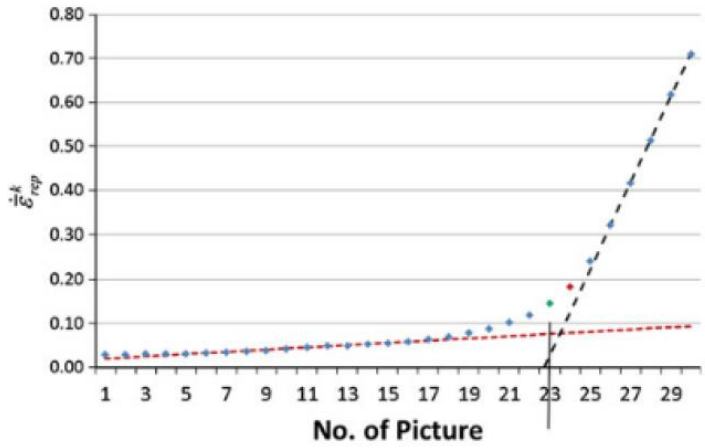

Figure 11: Time dependent FLC method. Number of picture vs strain rate [66]

The previous forming limit detection method is focused on the local strain rate (thinning rate) within the necking region. Martínez-Donaire *et al.* [71] looked at the unloading or drop in major strain rate ($\dot{\varepsilon_1}$) seen in regions adjacent to the neck. When the strain rate increases locally at the neck, regions adjacent to the neck start to unload and the strain rate in those regions decreases. This decrease can be monitored and used as a criterion for forming limit detection. Figure 12 shows experimental results of the evolution of major strain rate at different positions in the specimen. It can be observed that the strain rate at the border of the neck region ($\dot{\varepsilon}_1^A$) significantly drops past the 127 second mark. One of the major advantages of this method is that no additional processing of the DIC images is needed, since the DIC analysis already provides the evolution of $\dot{\varepsilon_1}$.

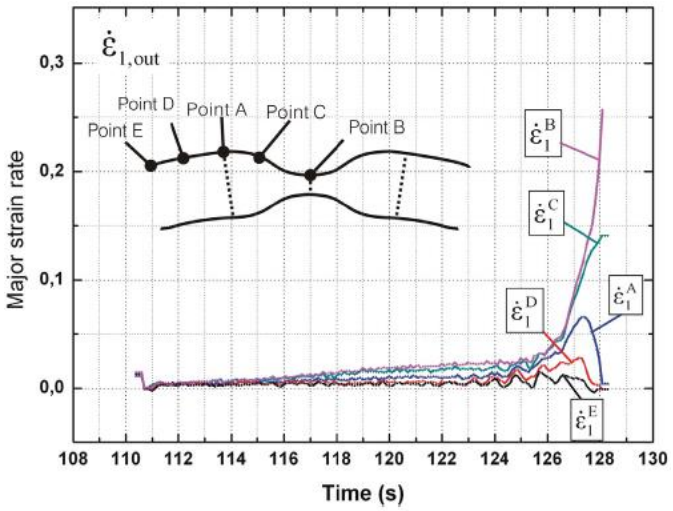

Figure 12: Martínez-Donaire Strain rate unloading method. Strain rate vs. time of points adjacent to crack locus [71]

Another, method of limit strain detection considers the curvature evolution of the test specimen during deformation. The local curvature of the sheet material changes as necking takes place. This method was explored by DiCecco et al. [127-128] and Min *et al*. [72], who observed a sudden increase in the surface curvature given by a 2D curvature fit along the specimen surface. Figure 12 describes the geometrical location of the line fit A-B that goes across the neck region as necking progresses on a given test specimen. Figure 13 shows the curvature evolution along line A-B (C'_{AB}), the material used is AA6022 utilizing a Marciniack punch. The curvature is seen to increase noticeably past the 34.5 second mark. The MSR_{AB} curve represents the mean square root error describing the quality of the fit. As it is observed the error associated with the curve fit increases as the surface topography gains complexity during necking. Martínez-Donaire *et al.* [71] also used this approach as a comparison to the strain rate unloading approach described previously. Both methods produced similar results with the maximum deviations oscillating 5-10% from the average value.

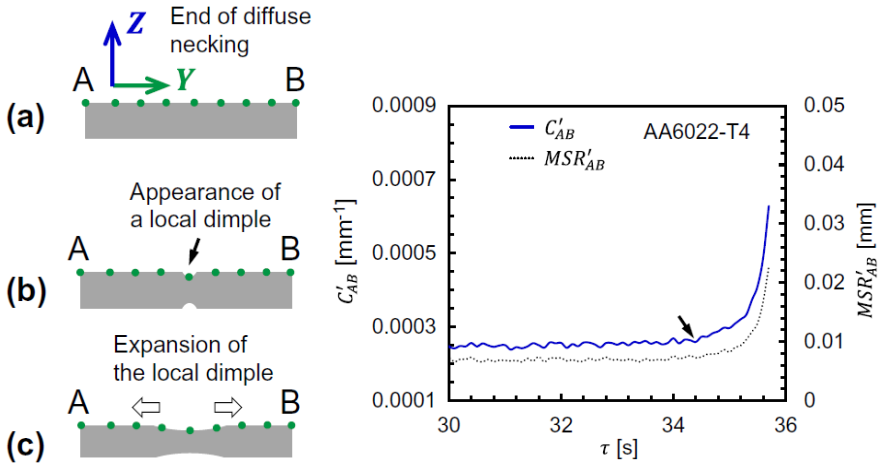

Figure 13: Min et al. curvature evolution vs time [72]

Formability testing for aluminum in warm forming applications has also been presented in the literature [5, 73-74]. However, similar to constitutive modeling, the current literature lacks formability testing that mimics the same thermal cycle present in die quenching. Parameters specific to the die quenching process route, such as testing of the material in a SHT condition and the effect of quench rate have not received attention within the formability characterization literature, with the exception of studies by DiCecco *et al.* [129] and Zheng *et al.*[136]. Formability testing should be performed using the same thermal processing route as used in real industrial die quenching processes. This gap in the current literature is a key focus of the current research.

1.6 Role of Friction in Sheet Metal Forming

1.6.1 Background

In total, about 23% of the world's total energy consumption is due to friction [75]. Tribology is the science and engineering of interacting surfaces in relative motion. It has diverse implications in the sheet metal forming world, affecting localized thinning, forming force, forming temperature, tool life and process cost.

Accurate characterization and control of the friction response becomes paramount in any sheet metal forming operation, and is equally important for robust FE forming simulation development. In order to effectively control the friction response, one must consider all factors that make up the tribological boundary condition. Kim *et al.* [76] summarized these factors for high speed steel, as seen in Figure 14 which clearly highlights the complexity of the interactions that make up the tribological interface state. The factors that can be altered if needed, are the production conditions, lubricant and the forming tool. The work piece on the other hand is a fixed variable in this framework since it is supplier-dependent. All of these factors amount to potential sources of tribological related failures in sheet metal forming. Lubricant failure is the least severe tribological failure and it simply describes the point at which the lubricant used in a particular forming process is considered ineffective. Lubricant ineffectiveness is not concretely defined and is application specific, different methods of lubricant failure determination will be explored in this section of the chapter. Galling is an adhesive wear mechanism in which sheet metal is deposited on the tool via adhesion, this deposit then hardens which causes scoring (abrasive wear) of subsequent material being formed [77]. Finally, since the majority of sheet metal forming operations are done in an industrial setting, tool life is often a major concern with regards to the feasibility and cost of the

process. Therefore, mild galling that may not present a direct threat to the formed parts may, over time, result in shorter tool life.

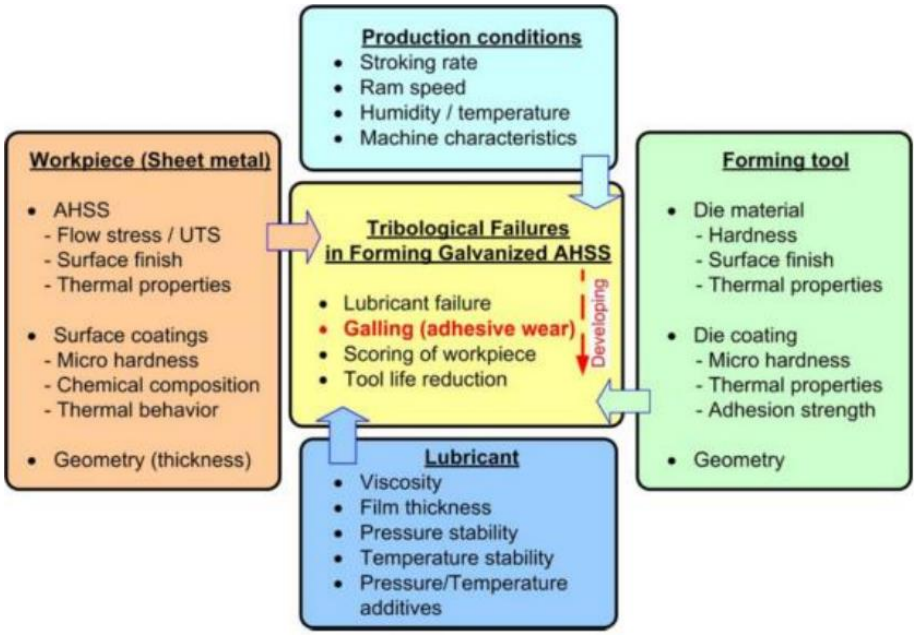

Figure 14: Tribological factors that affect a forming process [76]

1.6.2 Friction Theory

There have been many theories over the years that aim at explaining the fundamental physics of friction present between two bodies having relative sliding. Figure 15 shows the progression of friction theory over time. DaVinci was the first to study friction systematically [78] and Amontons [80] explained that the magnitude of the friction force is influenced by the degree of mechanical interlock between convex and concave mutually fitted surfaces having relative sliding. Coulomb [81] subsequently, built on Amontons' work to make the Amontons-Coulomb law which states that the friction force is proportional to the compressive force (normal force) used to push two surfaces together. Desaguliers [82] was the first to introduce the concept of adhesive friction. He studied the friction force for finely polished material (smooth surfaces), and postulated that some surfaces can be polished to an extent as to increase the adhesion between them, hence increasing the friction force as they slide past each other. Bowden and Tabor [83] shed some light on this

concept of adhesion proposed by Desaguliers, by making the important distinction between apparent and true contact area.

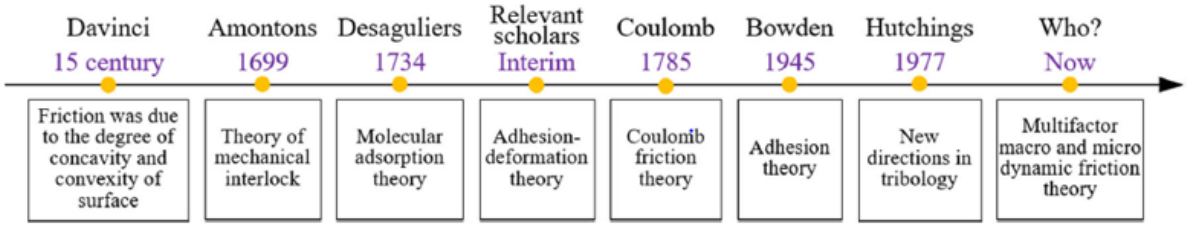

Figure 15: Evolution of friction theory over time [79]

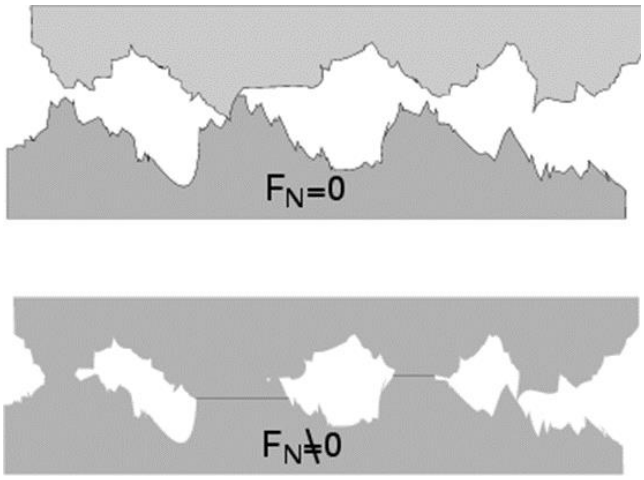

Figure 16: Schematic of surface asperities [84]

The true contact area is in actuality a fraction of the apparent contact area. Figure 16 illustrates this concept.The points in contact between the two surfaces are called junction points or asperities. Bowden postulated that due to the small surface area of asperities, intense interface pressures will act under compressive loading, thus, plastic deformation will take place when the surfaces in contact slide relative to each other. In this case, the friction force can be described by Eq. 5 [81-82].

$$F_f = F_N \frac{s}{H} \quad \text{(Eq. 5)}$$

where F_N is the normal force, s is the shear strength of the softer material and H is its hardness. This theory sheds light on some important concepts regarding friction phenomenon, however, it is not comprehensive enough to explain the interfacial complexities seen in sheet metal forming. For instance, it only considers plastic deformation and ignores possible elastic-plastic deformation. Depending on the surface condition, material hardness, temperature, normal force, *etc.*, some percentage of asperity deformation may be purely elastic. Suh [85] developed a more comprehensive theory that accounts for elastic-plastic deformation of asperities amongst other things as well as the abrasive plowing effect seen in Figure 17. Abrasive plowing is exhibited when the asperities of a harder material plow through the softer material which is an important factor to consider when analyzing wear mechanisims. So far, the interfacial interactions discussed (plastic/elastic deformation of asperities and plowing effect) do not include the addition of lubrication and its effects.

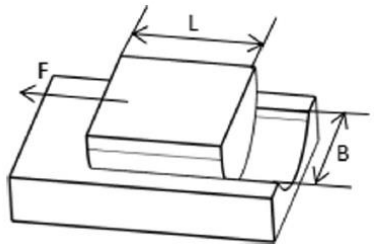

Figure 17: Plow model for abrasive wear [79]

1.6.3 Lubrication Regime

Generally, lubrication is used in sheet metal forming operations to reduce friction, to improve the surface condition of the part post forming and to reduce tool wear. Lubrication adds another layer of complexity to the interface boundary condition. There are four primary lubrication mechanisms or regimes between two contacting surfaces, as summarized in Figure 18. The dry condition is encountered when no lubricants are used in the forming operations, the friction boundary condition

in this case is reduced to the mechanisms discussed above. Some forming operations which consider a simple geometry, such as bending of steel using materials with high formability, do not require lubricants to ensure the integrity of the surface condition post forming. The boundary lubrication regime is one of the most prevalent in sheet metal forming operations. In this regime, the interface load is carried through contact between the asperities of the blank and the tool. Direct metal-to-metal contact is however prevented, due to the lubricant film being tightly adhered to the surface, preventing adhesion between the asperities of the contacting partners [87]. Mixed film lubrication also occurs in sheet metal forming operations. In this regime, pockets of lubricants form in the valleys of the contacting surfaces in these regions such that no direct contact occurs between the work piece and the tooling and the friction becomes a function of the lubricant properties; the asperities in this case however, still experience boundary lubrication. Thus, as sliding occurs fresh lubricant can supplied from the valley to the tip of the asperity [76]. Lastly, hydrodynamic lubrication is very rarely seen in sheet metal forming, except for solid film lubricants such as boron nitride. In this regime, no direct contact is exhibited between the work piece and the tooling and the friction force becomes entirely a function of lubricant properties such as viscosity and shear strength.

The curve seen in Figure 18 is coined the Stribeck curve [88] and plots the coefficient of friction as a function of the viscosity n of the lubricant, relative sliding velocity, v, and pressure, p, at the interface. The viscosity and velocity are inversely proportional to the coefficient of friction, while the interface pressure is directly proportional. In general, a more viscous lubricant will have a thicker film, resulting in greater prevention of metal-to-metal contact at the asperities. In addition, a higher velocity does not allow enough time for adhesion of asperities to take place, while, a

higher interface pressure results in an increased true contact area and thus increased friction coefficient.

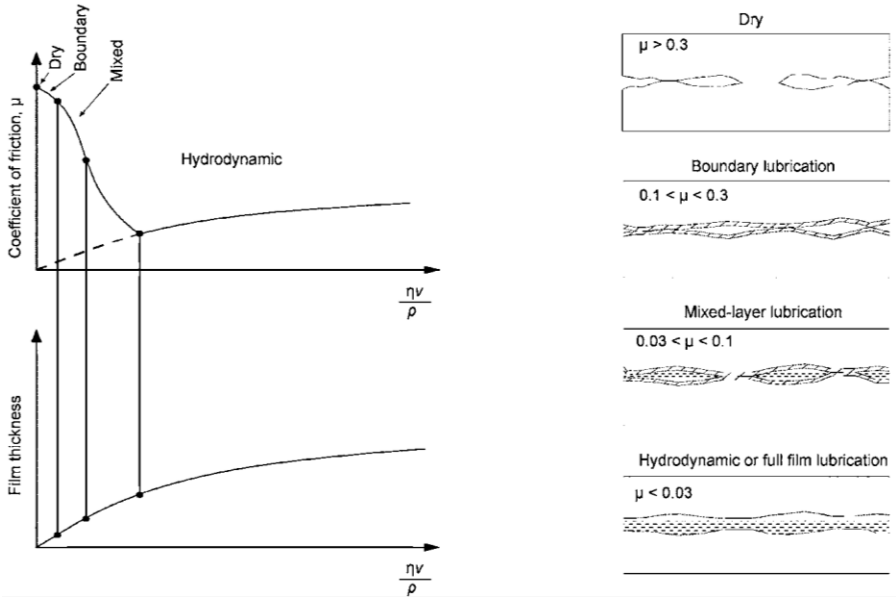

Figure 18: Lubrication regime schematic [86]

1.6.4 Die Coatings

Die coatings are used in many forming operations to improve the surface condition of the forming tool and reduce wear. Generally, a harder surface is desired for the tool which reduces the compliance of the surface asperities thereby reducing their plastic deformation and limiting adhesion between asperities of the tool and the work piece [91]. The hardness of the tool steel substrate is also important, as demonstated by Eriksson *et al.* [92], who reported that a hard die coating on a soft steel substrate will result in coating failure. Wang *et al.* [93] analyzed the performance of some common industrial die coating methods. Figure 19 illustrates the effect of thermoreactive diffussion (TD), physical vapour deposition (PVD) and chemical vapour depositon (CVD) coatings on tooling wear rate. The TD coating was the best performer since it had the lowest

wear rate, it can also withstand temperatures of up to 1875°F (1024°C) [94] which makes a viable option for die quenching of aluminum.

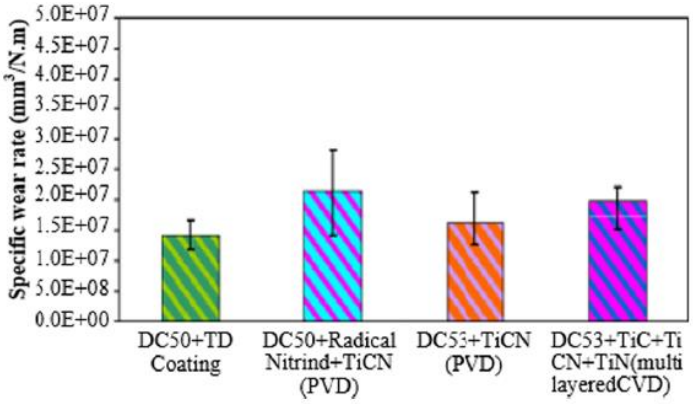

Figure 19: Wear rate performance of TD, PVD and CVD coatings [93]

Diamond like carbon (DLC) is another good candidate for the end process since it can also withstand elevated temperatures. Riahi *et al.* [95] compared the tribological performance of DLC and TiN coatings for hot forming of AA5182. More specifically, the study investigated the strength of adhesive junctions formed between tool and work piece at blank temperature 420 °C and 25 °C. Figure 20 shows the tangential force required to break junctions made between asperities *vs.* sliding distance at 25°C (a) vs 420°C (b). The experimental setup featured a counterface steel ball on a rotating platform which enabled measurement of the tangential force required to break juction between the ball and sheet specimen. The force increase due to temperature increase is dramatic for all coating conditions. DLC is the best performer since it has the lowest force and sliding distance required to break the junctions.

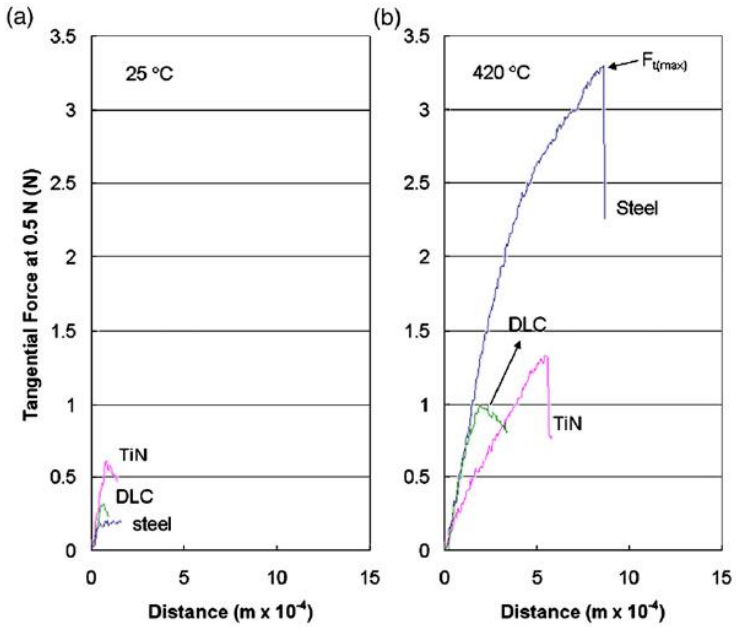

Figure 20: Sliding distance vs tangential force to break junction for DLC, TiN coatings and bear tool steel a) 25°C b) 420°C [95]

Riahi *et al.* [95] also performed a second set of experiments using a ball-on-disc tribometer to obtain the coefficient of friction of the interface for different die coatings, as shown in Figure 21. Again, the DLC coating was the best performer having a coefficient of friction less than one-half of the TiN coating for the 25 °C temperature condition. As for the 420 °C temperature condition, the DLC coating showed better overall stability and lacked the fluctuations in COF seen in the TiN and barer steel conditions, for high sliding distances up to about 1100 mm. The behavior exhibited is expected since the tangential force necessary to break the adhesion is much smaller, thus slip-stick effect is less pronounced.

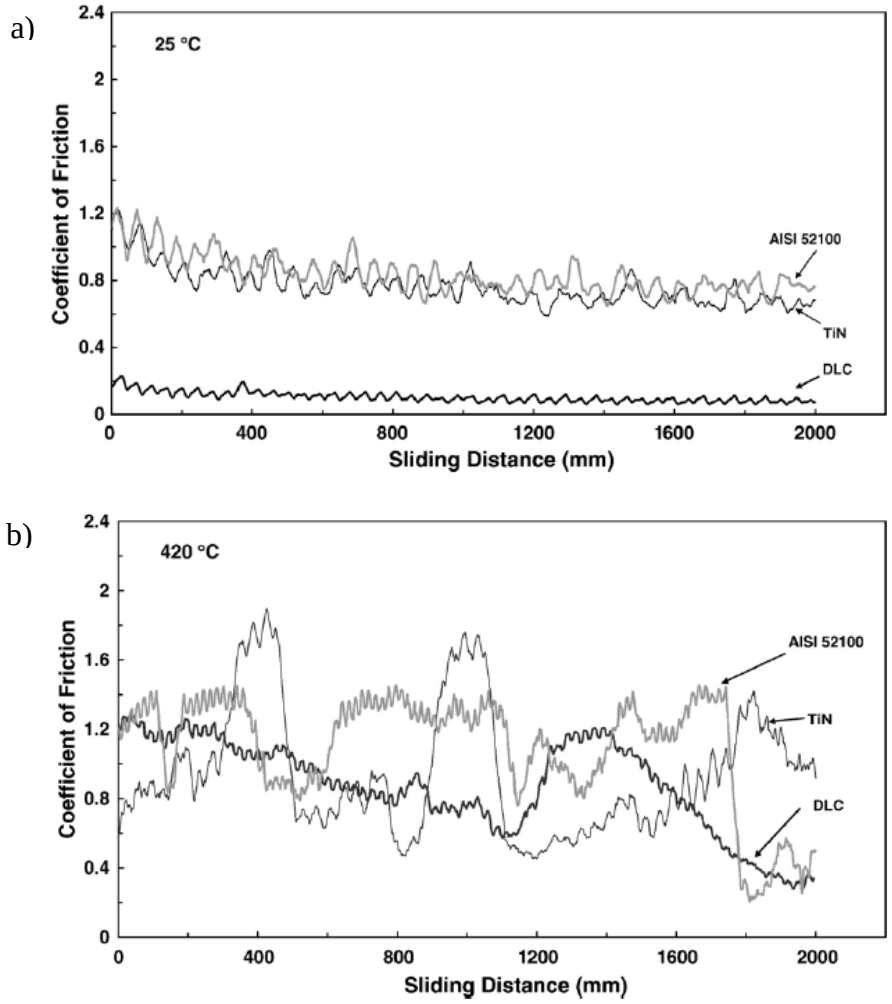

Figure 21: Sliding distance vs coefficient of friction (ball-on-disc tribometer) for DLC, TiN coatings and bare tool steel a) 25°C b) 420°C [95]

Podgornik *et al.* [96] investigated different test methods for evaluation of galling; this study contained an interesting comparison between available die coatings, as seen in Figure 22. The DLC coating offers the lowest coefficient of friction out of all coatings as well as the highest critical load for galling resistance. The DLC coating was also on par with the VANADIS 6 coating in terms of sliding distance prior to galling. For this reason DLC will be the coating of choice in the current work.

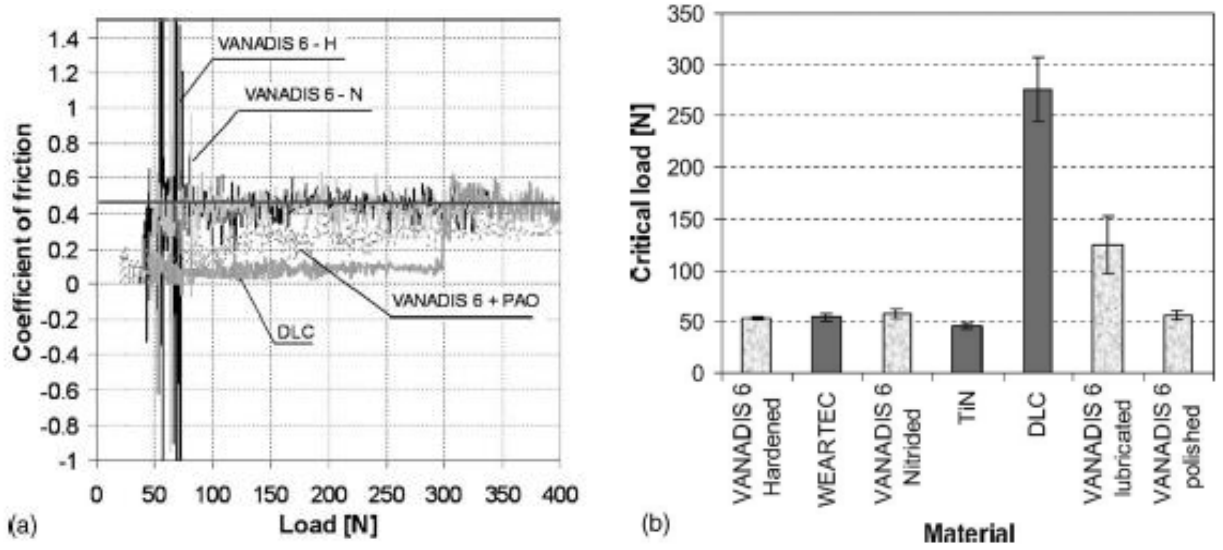

Figure 22: a) Normal force vs coefficient of friction for different coatings (cylinder on cylinder tribometer); b) critical load prior to galling for different coatings [96]

In effect, a realistic boundary condition between the work piece and the tool will likely resemble that in Figure 23. In general, when all of the friction and sliding mechanisms discussed above are present, a very complex system will result, that may prove difficult to model. Therefore, most available commernical FE codes use a simplified boundary condition that is mainly routed in Coulomb friction theory [79]. In applications where the tribological boundary condition is a sensitive parameter, accurate multifactor models can be used such as available in Triboform [97] developed at the University of Twente and implemented within AutoForm® software.

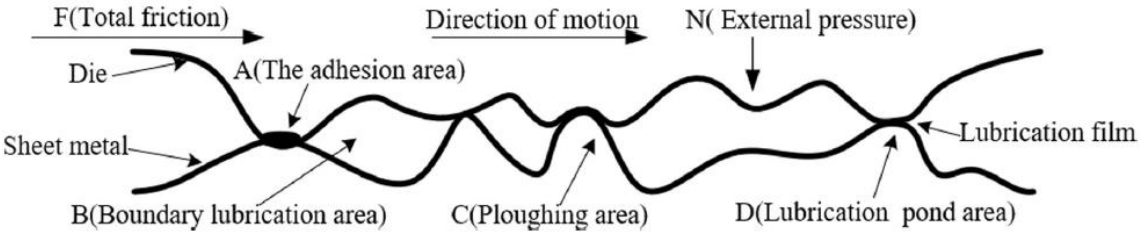

Figure 23: Schematic of realistic contact boundary condition [79]

1.6.5 Experimental Characterization of Tribological Phenomena

There exists a wide range of tribological tests aimed at quantifying and understanding interface interactions as well as aiding in the selection of process parameters such as lubricant, die coating, forming speed and temperature. Two general types of tests exist, simulative and process tests. Simulative tests mimic certain aspects of the end process without actually performing it, whereas process tests perform the exact process seen in the end application on a smaller or full size scale [98]. Since, the end application in the current research is die quenching, the tribology tests considered all required elevated temperature capability. To understand the pros and cons of the various available simulative tribological tests, a set of additional criteria are considered to help ensure that representative interface physical parameters are captured. The ideal tribological test should:

1. Operate in the boundary or mixed lubrication regime.
2. Have the capability of utilizing the actual tooling material as well material coatings.
3. Include some form of deformation of material.
4. Measure sliding friction and not rolling friction since, this is the dominant frictional mechanism seen in sheet metal forming applications.
5. Be a closed system, meaning no fresh lubricant can enter the local interface; this will ensure proper characterization of lubricant.

The first tribological simulator is the famous pin-on-disc first patented by Kobayashi *et al.* [111], which is a simulative test, as seen in Figure 24. The ball or pin (d), representative of the tooling material, is placed perpendicularly on a disc (D) that represents the sheet metal material intended for the end process. The disc is driven and rotates about its axis while the pin applies a normal force. This test meets criteria 1, 2 and 4 and lacks all other criteria and can be modified to include elevated temperature [99]. In addition, the contact area is very small in this test allowing minimal asperity interaction.

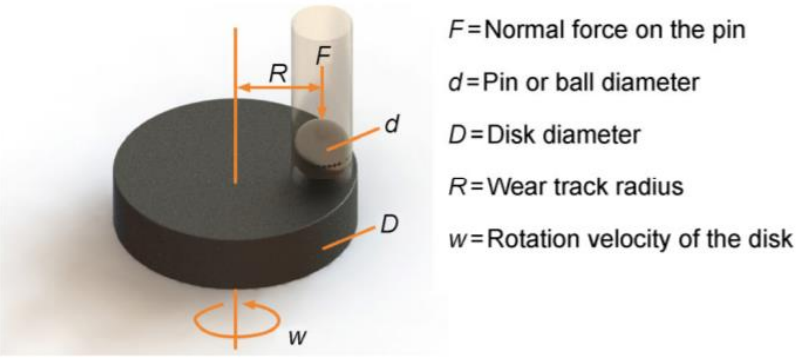

Figure 24: Schematic of pin-on-disc tribometer [91]

Another friction characterization test is the strip draw or flat die test, shown in Figure 25. The flat die test works by drawing a strip of sheet metal at a constant speed, through a furnace and a clamp (representative of the tooling) applying a normal force. The drawing force is then measured and the coeffient of friction is computed in Eq. 6.

$$COF_{Flat\ die} = \frac{F_{draw}}{2F_N} \quad \text{(Eq. 6)}$$

This test operates in the mixed lubrication regime, thereby fulfilling criterion number 1. It also fulfills 2 and 4. This test was used to characterize the friction response of two steel alloys in dry and lubricated condition by Yanagida *et al.* [100] The relationship between the compression load, drawing tension, coefficient of friction and drawing distance were obtained for different temperatures.

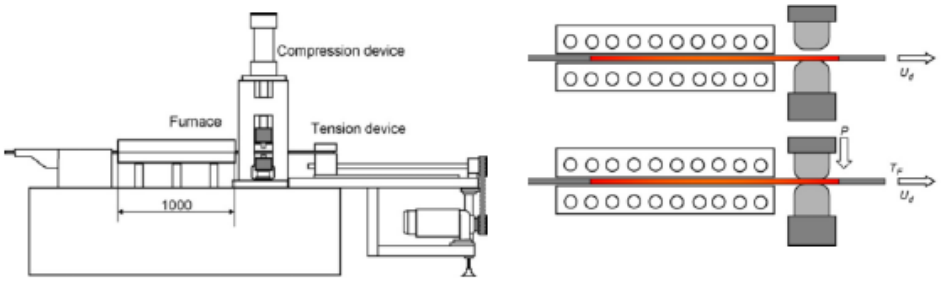

Figure 25: Schematic of flat die test tribometer [100]

The twist compression test (TCT), seen in Figure 26, is another laboratory test aimed at measuring the cofficient of friction though the resistance torque, this apparatus was developed around 1960 by Schey [110] at the University of Waterloo. Noder *et al.* [101] performed friction measurements using this apparatus to measure the interfacial friction for aluminum alloys under warm forming thermal cycles. The TCT functions by applying a normal force via a rotating test cup acting on the lubricated sheet specimen which is constrained not to rotate, thereby generating a reaction torque between between the cup and the sheet. The resistance torque T is measured and the coefficient of friction is calculated using Eq. 7 [101],

$$COF_{TCT} = \frac{T}{r_m P A_{ap}} \quad \text{(Eq. 7)}$$

where r_m is the mean radius of the test cup, P is the contact pressure and A_{ap} is the aparent contact area. This apparatus operates in the boundary lubrication regime and fulfills criteria number 1, 2, 4 and 5. This makes the TCT the only test that does not allow fresh lubricant into the interface, making lubricant breakdown and associated performance measurements possible. This tribological test actually imposes harsher conditions than seen in a real forming operation due to criteria 5, since new lubricant is usually allowed to flow onto the interface since the tooling does not slide over the same surface repetitively. Despite the lack of plastic deformation, the TCT is the tribological test considered in the current research due to its fulfillment of the rest of the test criteria.

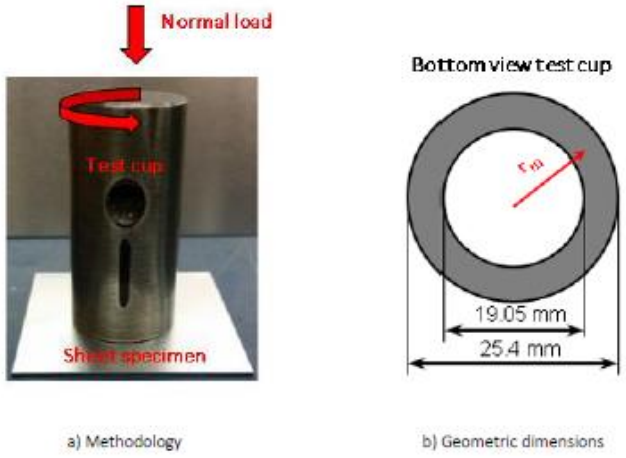

Figure 26: Twist compression tribometer a) methodology b) geometry of cup contacting surface [101]

The deep draw test, shown schematically in Figure 27, is a process test since it mimics an actual part being formed. This test uses a flat punch to form a circular blank which is clamped via a binder with a known interface pressure allowing material to flow into the die without wrinkling. This test fulfills all the criteria mentioned above since it is a representative test, however, there is no way of directly measuring the coefficient of friction; however, it is possible to infer the severity of the tribological condition through parameters such as the punch force and binder load. The severity of the tribological condition can be controlled through the die entry radius, blank diameter, forming speed, binder load, and temperature.

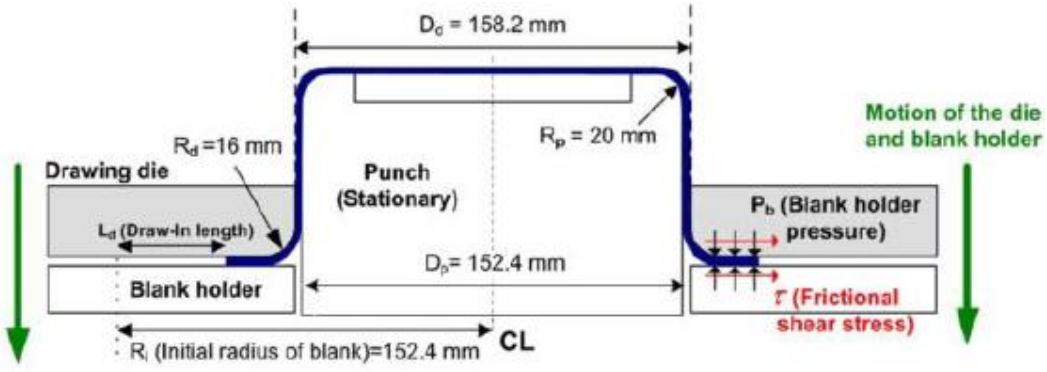

Figure 27: Schematic of deep draw test [76]

Pradip *et al.* [102] found that surface roughening of the work piece increased with plastic deformation and this resulted in a lower coefficient of friction due to a decrease in the contact area of asperities thereby suppressing adhesion.

There are no standardized methods for measuring tribological performance. Van der Heide [103] identified in his thesis titled "Lubricant failure in sheet metal forming processes" three wear mechanisms:

1. Cutting mode I; material is removed from the soft surface in the form of long ribbon-like chips;
2. Wedge formation mode; a wedge of material flows in front of the asperity;
3. Ploughing mode; material of the soft surface is displaced to the ridges of the wear track and no material is removed from the surface.

A failure criterion for lubricant and galling initiation was added to his frictional heating model. The criterion stated the following:

$$T_f > T_{cr}$$

in which T_f is the flash temperature (temperature at local interface of an asperity) and T_{cr} is the critical temperature of the lubricant. However, the flash temperature is not measurable experimentally and can only be estimated using additional parameters, thus, rendering this method complex and unfeasible for implementation.

Andreasen *et al*. [104], on the other hand, used surface roughness measurements with 2D and 3D profilometers to quantify the amount of galling exhibited in strip drawing and deep drawn cups respectively. Andreasen identified five categories for surface condition:

1. As received
2. Smooth
3. Scratched
4. Lightly galled
5. Medium galled

where, as received, refers to the un-deformed material, smooth is forming done under well lubricated surface condition in which the only interfacial interaction is the flattening of the work piece asperities and conditions 3-5 are different levels of galling. By analyzing the surface roughness of the cup wall, the surface condition can be assigned to a category. This method is very useful in assessing the lubricant and die coating lifecycle in an industrial setting, in which the surface condition of formed parts can be systematically checked to predict when lubricant reapplication will be needed. This method can be used for cup drawing tribological assessment performed in this work.

Hanna [105] presented an experimental method for determining the onset of metal-to-metal contact in a lubricated simulative tribological test. This was done using contact potential measurements (between tooling and specimen) in conjunction with friction coefficient measurement. The significance of this work is that metal-to-metal contact is only exhibited if lubricant failure has occurred; thus, a criterion for lubricant breakdown can be retained, which can quantitatively infer the level of asperity interaction. The experimental set-up and results for this method are shown in Figure 28. As made evident by Figure 28 b), the sudden drop of electrical contact potential is accompanied by a significant increase in the coefficient of friction.

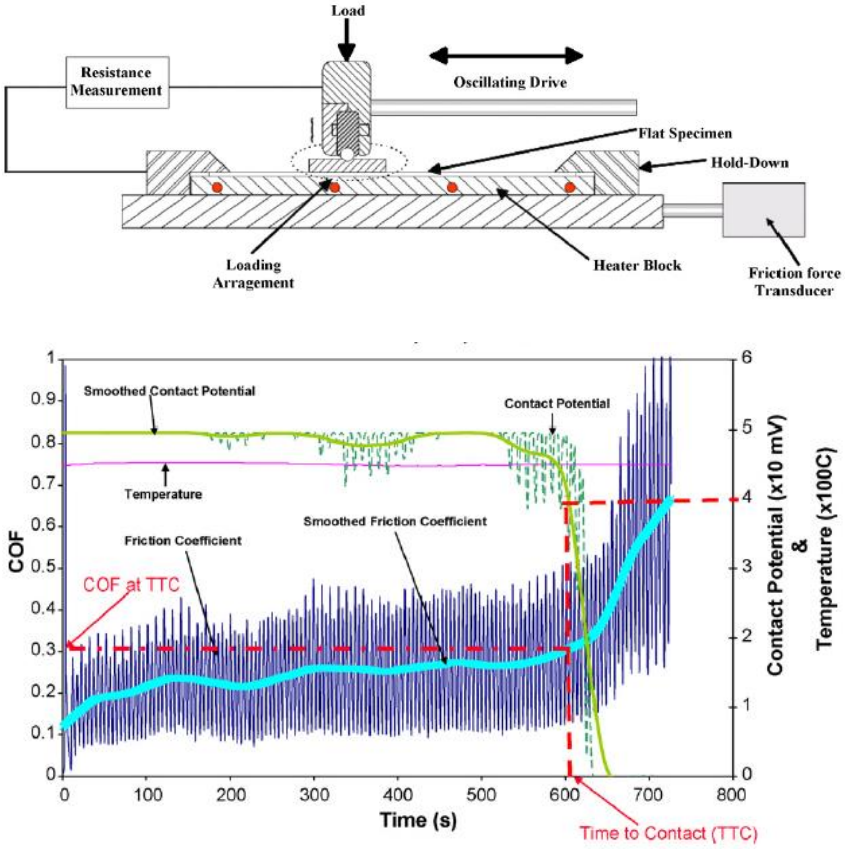

Figure 28: a) Reciprocating tribometer b) Time vs COF (left axis) and contact potential (right axis) [105]

1.7 Summary of Literature Review and Scope of Current Work

The foregoing literature review has served to highlight the potential benefits of utilizing 7000-series aluminum alloys in automotive structural components to reduce overall vehicle mass. A number of prior studies have demonstated that hot forming in a solutionized state followed by the die quenching (DQ process) can result in increased formability of these alloys, but that subsequent ageing is required to achieve peak strength. The DQ process is known to be sensitive to process parameters, such as quench rate and solutionizing time, which must be controlled when forming these materials in a high volume production setting. The constitutive modeling literature has shown the importance of testing specimens in a solutionized condition, that must be accompanied by

quenching rapidly to the test temperature followed by immediate testing, and that methods of avoiding negative hardening rates for high temperature tensile testing must be employed.

While forming limit detection methods have become more sophisticated with the advent of DIC technology, very little attention has been given in the published literature to die quench formability characterization, as well as the development of numerical models to simulate the DQ process. In particular, there exists a need to further refine and validate the existing constitutive models and formability criteria currently available to simulate the DQ process. Lastly, elevated temperature tribology studies have been receiving more attention recently due to the key role of friction in warm and hot forming of aluminum alloys; however, most studies focus on room temperature or intermediate temperature (150-200°C) conditions and do not consider the fully-solutionizized high temperature conditions corresponding to DQ forming.

To address these shortfalls in the published literature, this thesis addresses the simulation of AA7075 under die quench processing conditions. One focus of the thesis is on experimental friction characterization and lubricant selection, highlighting the effects of temperature, tool hardness and die coating. The second focus is on improved constitutive modeling for DQ conditions. Finally, the improved friction and constitutive treatments are implemented within a numerical model of a series of available DQ forming experiments performed by George *et al.* [130] that are used for model validation.

The key objectives of the study are:

- Characterization of friction behaviour and COF determination for AA7075 using coated and un-coated tools under elevated temperature DQ processing conditions;

- Development of a metal physics-based temperature and strain rate dependent constitutive model;
- Development of a numerical model for the die quench process and validation of the model against available formability experiments.

The research presented herein is part of a larger project undertaken by the University of Waterloo in collaboration with Honda Development & Manufacturing of America, Promatek Research Centre and Arconic Ground Transportation Group. The overarching goal of this project is to support the implementation of high strength aluminum alloys in the fabrication of automotive structural components under high volume production.

The balance of this thesis is organized as follows. Chapter 2 presents the experimental methods used in the friction characterization experiments. Chapter 3 discusses the experimental friction characterization results. Chapter 4 presents the development of a new constitutive model for DQ forming operations, while Chapter 5 presents the numerical model used to simulate the formability experiments performed by George *et al.* [130]. Chapter 6 shows the numerical predictions and comparison to the formability experiments as part of the model validation process. Lastly, Chapter 7 provides the conclusions and recommendations stemming from this work.

2 Friction Characterization - Experimental Methodology

This chapter presents the experimental set-up for the friction characterization experiments that focused on die quench forming process conditions and were performed as part of this research.

2.1 Material Selection

The material considered in this study is 2 mm thick AA7075 high strength aluminum alloy sheet. The as-received material condition corresponded to a T6 or peak aged temper, with the room temperature mechanical properties [131] and chemical composition shown in

Table 1.

Alloy	Mechanical Properties			Chemical Composition (wt. %)								
	σ_y (MPa)	UTS (MPa)	ε_{total}	Mn	Si	Cr	Mg	Ti	Cu	Zn	Fe	Zr
7075	503	572	11	0.04	0.08	0.19	2.27	0.03	1.38	5.63	0.15	0.01

Table 1: Material Mechanical Properties and Chemical Composition [131]

2.2 Friction Characterization Experiments

The friction characterization of AA7075 under die quenching conditions was conducted using the TCT apparatus available at the University of Waterloo. Here, the TCT apparatus is described, followed by the choice of lubricants, tooling, coatings and process parameters that affect the tribological response.

2.2.1 TCT Apparatus

The TCT apparatus was first developed at the University of Waterloo around 1960 by Schey [62] and a modified version of the apparatus was used in the current study. The modifications were developed by George [150] and Noder *et al.* [101] to incorporate heated tooling and a solutionizing

furnace for elevated temperature friction characterization. A schematic of the test apparatus is shown in Figure 29.

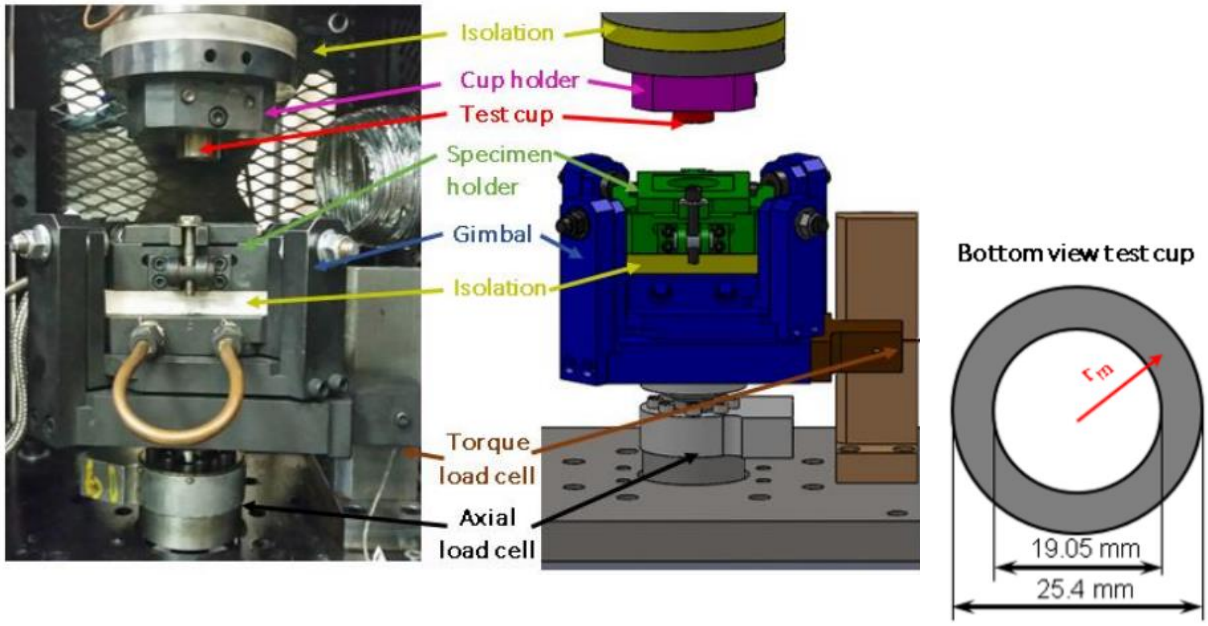

Figure 29: TCT apparatus (left) and the CAD drawing for the apparatus (middle) bottom of the test cup (right) [101]

The TCT apparatus uses an annular test cup, which is pressed on a piece of lubricated sheet metal that is clamped by the specimen holder. Once the desired clamping load is applied, the test cup then proceeds to rotate at a constant sliding speed. The test cup applies an axial force downward on the sheet specimen, while the rotation of the cup produces a torque reaction load due to friction. The resistance to sliding (the reaction torque) obtained from the torque load cell (T), is used to calculate the COF based on the mean radius (r_m) of the test cup, the test cup contact area (A_{cont}) and the interfacial pressure (P) measured by the axial load cell, as given by Eq. 8.

$$COF = \frac{T}{r_m P A_{cont}} \qquad \text{(Eq. 8)}$$

The test cup (shaded red) in Figure 29 is held in the cup holder (pink) by a setscrew, which prevents it from rotating within the holder under the action of the reaction torque due to friction. The specimen holder (green) holds the sheet metal specimen in place and prevents it from rotating during the test. The gimbal assembly (blue) has a self-aligning mechanism, which ensures parallel contact between the test cup and test specimen. The axial load applied during the test is measured by a 2,270 kg capacity load cell (black), while the torque load due to the resistance to sliding is determined using a 45.5 kg capacity load cell (brown) and torque arm radius of 114.58 mm. The specimen holder and the cup holder can be heated using embedded cartridge heaters for test conditions corresponding to elevated temperature forming conditions.

2.2.2 Lubricants

Several lubricants were considered for AA7075 die quenching application. These lubricants are intended to ensure a low friction coefficient between the tooling and the sheet metal, while tolerating the elevated working temperature. The lubricants tested were the Fuchs AL278 [89], the Fuchs Renoform 25 [117], the Fuchs Renoform 10 [90] and boron nitride [112]. Lubricant details, application method and specimen preparation are discussed in the following sections.

2.2.2.1 Fuchs AL278 Forge ease

The Fuchs AL278 is a synthetic elevated temperature lubricant primarily targeted for warm forming applications. The lubricant is applied as a liquid onto the test cup. The recommended dilution ratio is four parts lubricant and one part isopropanol or water depending on whether fast drying is a priority. The service temperature of this lubricant is rated up to 350°C, although lubricity can be compromised at temperatures above 275°C, which is the melting temperature of a wax ingredient [101], [116]. Replacing water with alcohol resulted in a more even wetting of the

blank [101]; this is desirable since it will ensure lubricant reaches all locations on the blank. Therefore, a dilution ratio of four parts isopropanol and one part lubricant was used.

2.2.2.2 Fuchs Renoform 25

The Fuchs Renoform 25 ALWF is a water-based lubricant for hot and warm forming of aluminum. This lubricant can operate in temperature ranges of 200 to 500℃; it also enhances die cooling during hot and warm forming [117]. The recommended mixture is 4:1 to 9:1 parts water to lubricant [117]. Again, for better wetting and faster drying isopropanol was used instead of water to dilute the lubricant.

2.2.2.3 Fuchs Renoform 10

The Renoform 10 ALWF is a concentrated water-based lubricant specially made for metal flow in warm or hot forming of aluminum for temperature ranges of 200 to 500°C. The recommended mixture is four parts water and one part lubricant [107]. Again, for better wetting and faster drying isopropanol was used instead of water to dilute the lubricant.

2.2.2.4 Boron Nitride

Boron nitride is a synthetically produced crystalline compound with chemical formula BN. The crystalline structure of this compound is hexagonal. ZYP Coatings is a boron nitride lubricant manufacturer, which provided the boron nitride lubricant used in this study [112]. The product name is the BN Lubricoat, which has a maximum operational temperature of 1000°C.

2.2.3 Tooling and Specimens

The annular test cups used in this study are made from Dievar tool steel, which is specifically intended for hot tools and elevated temperature-forming applications. The cups were hardened to a hardness of 52 HRC. Following hardening, the cups were prepped using a specific polishing procedure described in Section 2.2.3.1 to ensure surface roughness is consistent. After polishing,

some cups were shipped for coating; these cups received a diamond-like carbon (DLC) coating, which is intended to enhance tool durability by reducing pickup. Pickup is a phenomenon that takes place during high temperature forming of aluminum; at temperatures close to solutionization, the aluminum becomes very soft and as a result can adhere easily to the tool and die. When pickup takes place over many production parts, the tool surfaces start to wear quickly and part defects become apparent. The sheet metal surface roughness was also measured to account for possible variability and assess the surface condition of the as-received material. Details of the roughness measurement process are highlighted in the following section.

2.2.3.1 Cup heat treatment and surface roughness

To ensure the repeatability, prior to coating, all cups received the same polishing treatment. The cups were polished using the Struers TegralPol-15 automated sanding wheel with 220, 500, 800, 1000 and 1200 grit wet sandpaper. Each cup was held carefully with its annular surface parallel to the sanding wheel and light to moderate pressure was applied with frequent turning to ensure even polishing of the test cups. Test conditions using uncoated cups also received the same polishing treatment in-between tests to reuse cups. After polishing, the surface roughness of the cups was measured using a Taylor-Hobson Surtronic 3+ profilometer, the results of which are shown in Table 2 for two representative cups. Each cup was measured 6 times at different locations of the cup face; results of both cups were then averaged to get a nominal surface roughness for the specified polishing sequence. The surface roughness values presented in Table 2 are the Ra which is the arithmetic mean of surface heights measured across a surface, the lower the number the smoother the surface. The average surface roughness value in Ra for both cups was 0.08 µm with a standard deviation of 0.012 µm; this value corresponds to an N2-N3 Lapping surface roughness grade number [114].

	Roughness (Ra) (µm)	
Cup	1	2
	0.12	0.1
	0.1	0.1
	0.06	0.08
	0.06	0.08
	0.06	0.08
	0.1	0.06
Average (Ra) (µm)	0.08	0.08
Standard deviation	0.02	

Table 2: TCT cup surface roughness (Ra) measurements after polishing in µm

The cups sent for coating received the same polishing sequence prior to coating as the uncoated cups.

2.2.3.2 Sheet surface roughness

The sheet specimen surface roughness was also measured. Two categories of specimens were identified: smooth and scored. The smooth specimens had smooth and scratch-free surfaces based on visual inspection; on the other hand, scratched specimens had mild scoring on the surface due to handling. Three surface roughness measurements were taken in both the rolling (RD) and transverse (TD) directions of the sheet for both categories of specimens. The TD in all cases was slightly rougher than the RD. The average of all measurements was 0.11 µm (Ra), which was taken as the nominal surface roughness of the as received material, with a standard deviation of 0.02,

this value is higher compared to AA7075 used by Noder *et al.* [101], which had a surface roughness of 0.061 µm. However, it is still much smoother than the value for AA7075 reported by Schey [110] of 0.23 µm.

Material	AA7075			
Specimen state	**Smooth RD**	**Smooth TD**	**Scored RD**	**Scored TD**
Repeat 1 Ra (µm)	0.08	0.12	0.12	0.1
Repeat 2 Ra (µm)	0.08	0.12	0.1	0.14
Repeat 3 Ra (µm)	0.1	0.1	0.12	0.14
Average	0.09	0.11	0.11	0.13
Standard deviation	0.01	0.01	0.01	0.02
Average RD/TD	0.09		0.12	
Standard deviation RD/TD	0.02		0.02	
Average of both conditions	0.11			
Standard deviation all	0.0191			

Table 3: AA7075 sheet metal surface roughness (Ra) for scored and smooth samples in μm

2.2.4 TCT test parameters

In this work, the blank is not lubricated directly. Instead, the test cup is sprayed with the appropriate lubricant at the manufacturer's recommended concentrations using an air spray gun, prior to testing. This approach mimics hot stamping practice in which the tooling is lubricated instead of the blank since these lubricants tend to smoke or burn at the solutionizing temperature. Each test cup receives four passes and is left to dry. The lubricant dried evenly on each cup after which the cup is attached to cup holder via a setscrew.

The twist compression test procedure starts by heating the sheet specimen to the 470°C SHT temperature in a small convection furnace adjacent to the TCT apparatus. The specimen is heated for 15 min including heat up time of 8 mins [54]. The sheet specimen is quickly taken out of the furnace using a pair of metal tongs and is placed securely in the specimen holder. The transfer time was under five seconds during which time the specimen cooled by about 60-70°C. The TCT apparatus begins by using the annular test cup to apply an axial load on the sheet specimen, the load curve for the applied axial load is shown in Figure 30. The TCT test cup is either at RT or set to a specific temperature as per the test condition, the load curve takes 8 seconds to get to the full clamping pressure. Then, rotation of the test cup on the sheet specimen takes place. After full rotation is reached, the test cup is lifted from the sheet specimen and the cup and specimens are removed and inspected.

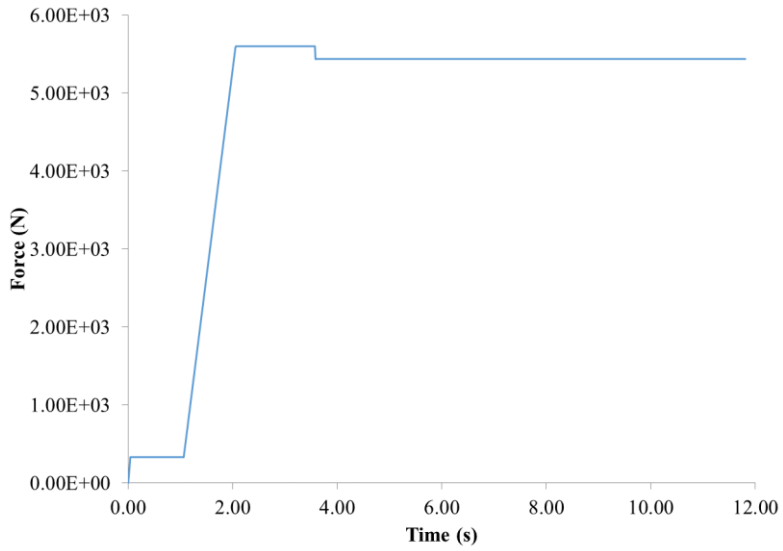

Figure 30: TCT Load-cell Force vs Time Profile

The parameters used for most tests conducted are as follows:

(i) The sliding speed was 30 mm/s, the maximum sliding speed possible while avoiding damage to the torque load cell.

(ii) A normal pressure of 30 MPa was adopted which is the highest axial pressure the TCT apparatus can apply.

(iii) The sliding distance was case dependent; it was used as a lubricant characterization parameter, rather than an operational parameter for a target process.

2.2.5 Characterization of Test Temperature

For tests requiring heated tooling, the cups are mounted within the heated cup holder and required about 15 min to reach steady state. The cup holder set temperature was offset + 20°C hotter than the required tool temperature for the given test condition, ensuring that the temperature at the contacting face of the test cup is at the nominal tooling temperature. The required temperature offset of the specimen holder is only + 10°C. These offsets were determined by measuring the cup and specimen temperatures directly while incrementing the input temperature until the measured temperature matched the desired value. Figure 31 shows an instrumented specimen, used for temperature validation testing for AA7075 friction characterization with RT and heated tooling. The design was achieved by milling a 1mm deep, 14.7 mm long slot that stops at the mean radius of the test cup when it is placed on the center of the sheet specimen. A National Instrument DAQ (USB-6000) was used for temperature data acquisition with a sampling frequency of 1 kHz. Figure 32 shows the temperature time history of the instrumented specimens for various tooling temperatures. Each temperature designation refers to the solutionization temperature and the set tooling temperature, for example 470-350°C corresponds to a solutionization temperature of 470°C and a tooling temperature of 350°C.

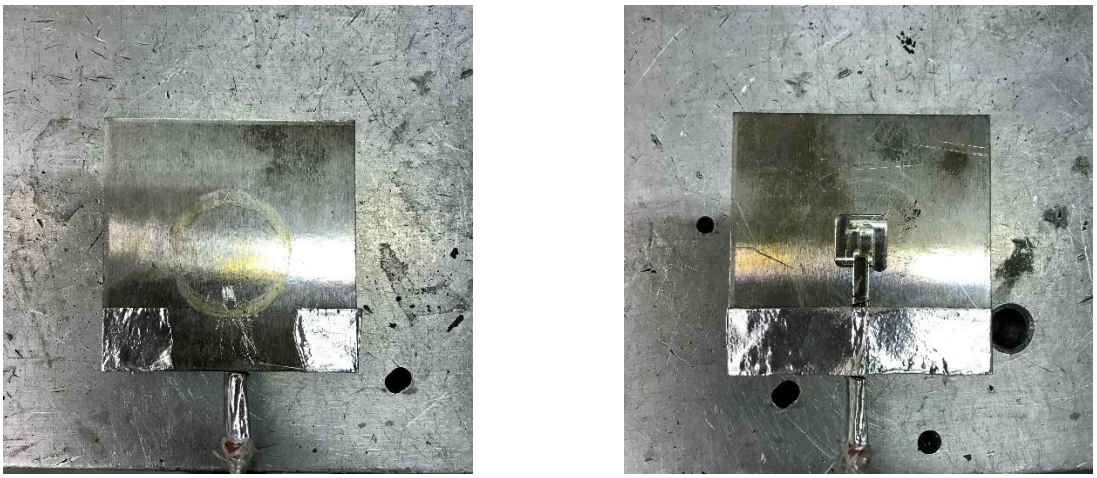

Figure 31: Thermocouple instrumented TCT sheet specimen

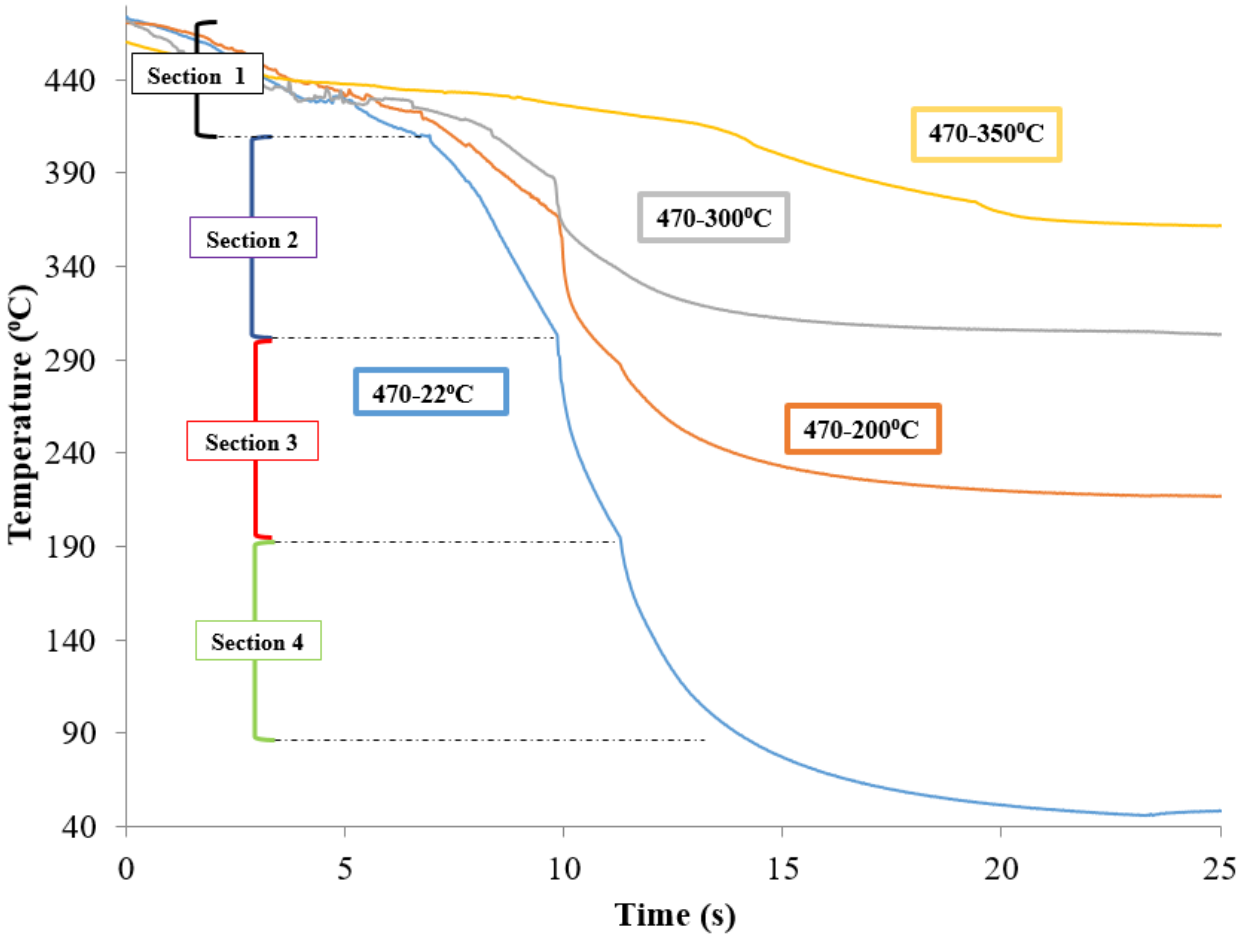

Figure 32: Cooling profiles of blank for various tooling temperatures for a blank quench from 470°C to tooling temperatures 22 (blue), 200 (orange), 300 (grey) and 350°C (yellow)

The transfer time of these instrumented specimens was under 7 seconds for all cases, which is slightly longer than the time to transfer the non-instrumented specimens due to manual thermocouple manipulation. Almost all the time-temperature curves have the same characteristic shape with four distinct sections:

- First highlighted in black: very low cooling rate for about 7 seconds.
- Second highlighted in dark purple: a low linear cooling rate for about two seconds at the beginning of clamping.
- Third highlighted in red: a higher cooling which continues for about 2 seconds while decreasing slightly past the mid point.
- Fourth highlighted in green: cooling rate increases slightly just past the second section then continues to decrease in a decaying fashion.

Considering a clamping time of eight seconds, Table 4 displays the average temperature the friction test was performed at for each test condition, along with cooling rates for section one, two and three of the time temperature curves. The cooling rate was obtained by taking the linear average of the temperature vs time at the appropriate section.

Temperature Range (^oC)	**Average Test Temperature (^oC)**	**Section One Cooling Rate ($^oC/s$)**	**Section Two Cooling Rate ($^oC/s$)**	**Section Three Cooling Rate ($^oC/s$)**
470-25	90	7	36.4	73.2
470-200	240	7	19.0	54.6
470-300	320	7	13.0	33.8
470-350	400	7	6.0	4

Table 4: Cooling rates of sheet specimen for tooling temperatures (25, 200, 300, 350^oC)

The cooling rates for both sections 2 and 3 of the curves decrease with increasing tooling temperature due to the reduced undercooling.

2.2.6 TCT Test Matrix

The TCT test matrix for AA7075 is presented in Table 5. This test matrix presents the testing completed in this study. Each test condition comprises a specific temperature and lubricant, *e.g.* 470-300ºC + Fuchs AL278 indicates a solutionization temperature for the blank of 470ºC and a TCT tooling temperature of 300ºC along with the Fuchs AL278 lubricant. Each test condition had a minimum of 3 repeats. All test conditions had a sliding speed of 30 mm/s and an axial pressure of 25 MPa, except for select conditions, which were tested at 30 MPa.

	Fuchs AL278	**Fuchs Renoform 10**	**Fuchs Renoform 25**	**Boron Nitride**	**Unlubricated**
470-400ºC	3				
470-350ºC	3				
470-300ºC	3				
470-200ºC	3	3	3	3	3
470-80ºC					3
470-22ºC	3	3	3	3	3
Total					42

Table 5: TCT test matrix including temperature condition and lubricant selection

The test procedure of the study highlighted in Table 6 is similar to the test procedure in Table 5 except the tooling remains at room temperature for all conditions and Fuchs AL278 is used for all conditions. However, the pressure and the speed are varied.

		Speed	
		5 mm/s	**30 mm/s**
Pressure	**10 MPa**		3
	30 MPa	3	3
Total			9

Table 6: TCT test matrix, testing different test velocities and interface pressures, with Fuchs AL278 lubricant and room temperature tooling

3 Friction Characterization Results

The presentation of the friction testing results starts with the dry unlubricated friction characterization followed by a comparison of the performance of different lubricants for uncoated TCT cups at room and elevated temperature. The best performing lubricant is then characterized using DLC coated cups at different tooling temperatures.

3.1 Dry Unlubricated Baseline COF

Testing began by measuring the friction response of an unlubricated cup with no coating to establish a baseline from which comparisons can be made. Three tooling temperatures were varied, from room temperature (RT) or 23 °C to 80°C and 200°C, to measure the friction response at different temperatures. Figure 33 shows the unlubricated friction response for the three temperatures mentioned above.

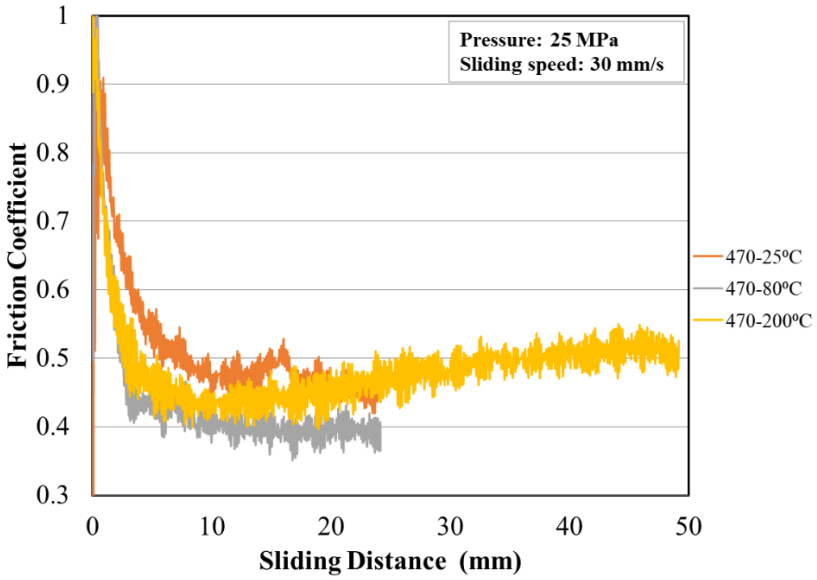

Figure 33: Unlubricated, uncoated TCT friction results with solutionized blanks and various tooling temperatures

For the unlubricated cups, adhesion between the test specimen and the cup takes place early in the test, which causes a very high initial coefficient of friction for all temperature conditions. This bond is broken as the cup starts to rotate, hence the reduction in the coefficient of friction. The

steady state friction level for the unlubricated condition is between 0.4 and 0.5 for all three-temperature conditions. This value is quite high as compared to a lubricated surface; however, it is typical of aluminum-on-steel dry sliding contact [115]. At these friction levels, excessive amounts of galling were observed on the test specimen for all temperature conditions.

3.2 Lubricant Performance – Uncoated Tools

Lubricant performance was initially tested without die coatings and using room temperature tooling. Figure 34 shows the results for all lubricants tested. Each lubricant had a minimum of three repeats per test condition. The worst performing lubricant is the Fuchs Renoform 10, although its initial COF was rather low and lay between the Fuchs Al 278 and the boron nitride values. The best performer (lowest COF) is the Fuchs Al 278. The boron nitride, along with the Fuchs Al 278, had a relatively stable COF over the entire sliding distance, generally indicating that no breakdown of the lubricant occurred.

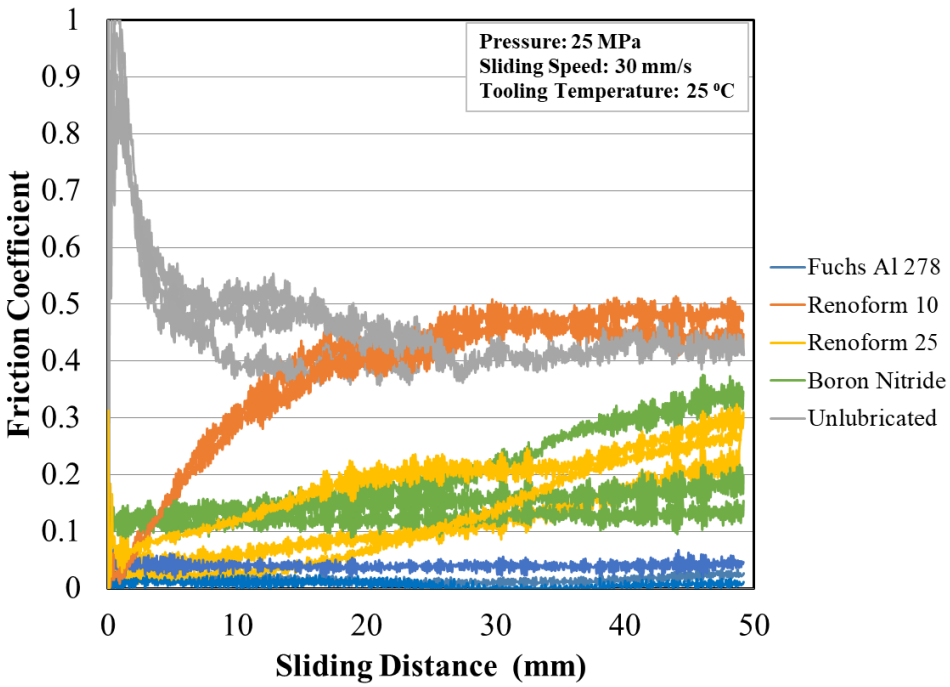

Figure 34: TCT results of different lubricants for solutionized blank and room temperature tooling

Figure 35 summarizes the average COF for each test condition along with the measured standard deviation over the repeat tests. The average of the unlubricated condition was taken using data from sliding distances of 6 mm or higher to avoid the initial static friction peak values. The boron nitride and Renoform 25 seem to offer similar levels of friction response for the first 10 mm (Figure 35). The Renoform 25 then experiences a continuous increase in the friction coefficient

over the sliding distance (COF= 0.13 at 5 mm and COF= 0.33 at 48 mm), giving rise to the higher standard deviation value seen in Figure 35. The Renoform 10 has the highest standard deviation due to early lubricant breakdown. The boron nitride and Fuchs Al 278 have the least variability in the data with no signs of lubricant breakdown. However, the Fuchs Al 278 produces an exceptionally low average coefficient of friction about 0.02; 7 times lower than that of boron nitride.

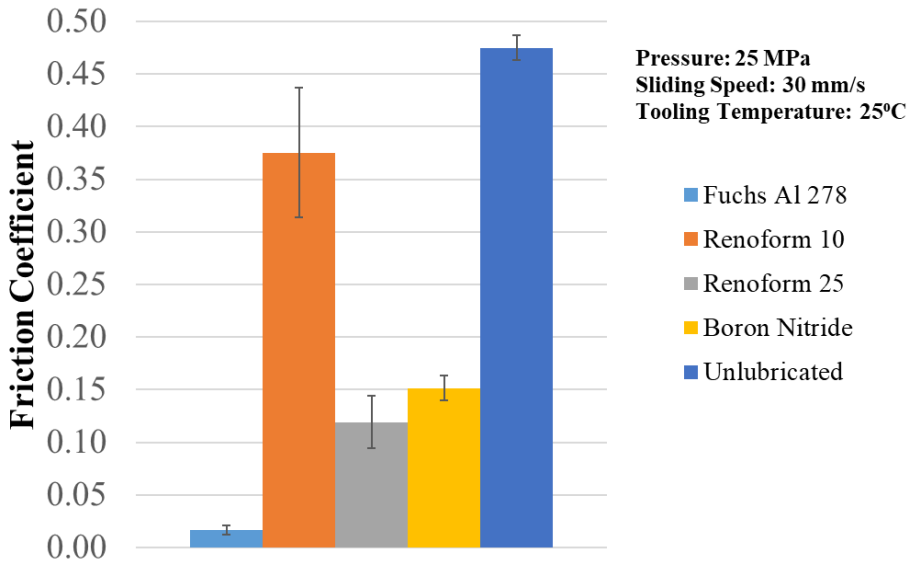

Figure 35: Summary of lubricant performance for solutionized blank (470ºC), RT tooling, 25 MPa pressure and a sliding speed of 30mm/s

Figure 36 shows the lubricant performance for a tooling temperature of 200°C, which results in a lower cooling rate, compared to the room temperature tooling condition (see Table 4). As a result, the temperature of the lubricant is higher during the test, compared to the room temperature tooling tests. The boron nitride experienced lubricant breakdown at this tooling temperature and resulted in a coefficient of friction higher than that of the unlubricated condition at large sliding distances. The Renoform 10 performance was somewhat superior to that exhibited for initially RT tooling, but it did experience a progressive breakdown for two of the three repeats. The Renoform 25

resulted in an initial coefficient of friction of 0.1 for two of the three repeats, which drops at about 7 mm sliding distance, but then increases again and somewhat stabilizes after 20 mm sliding distance at a COF equivalent to the unlubricated condition (~ 0.45). The Fuchs Al 278 experienced a 25% drop in the average COF to about 0.015 with the tooling temperature set to 200°C; this is similar to the behavior reported by Noder [101] for this lubricant at 170°C.

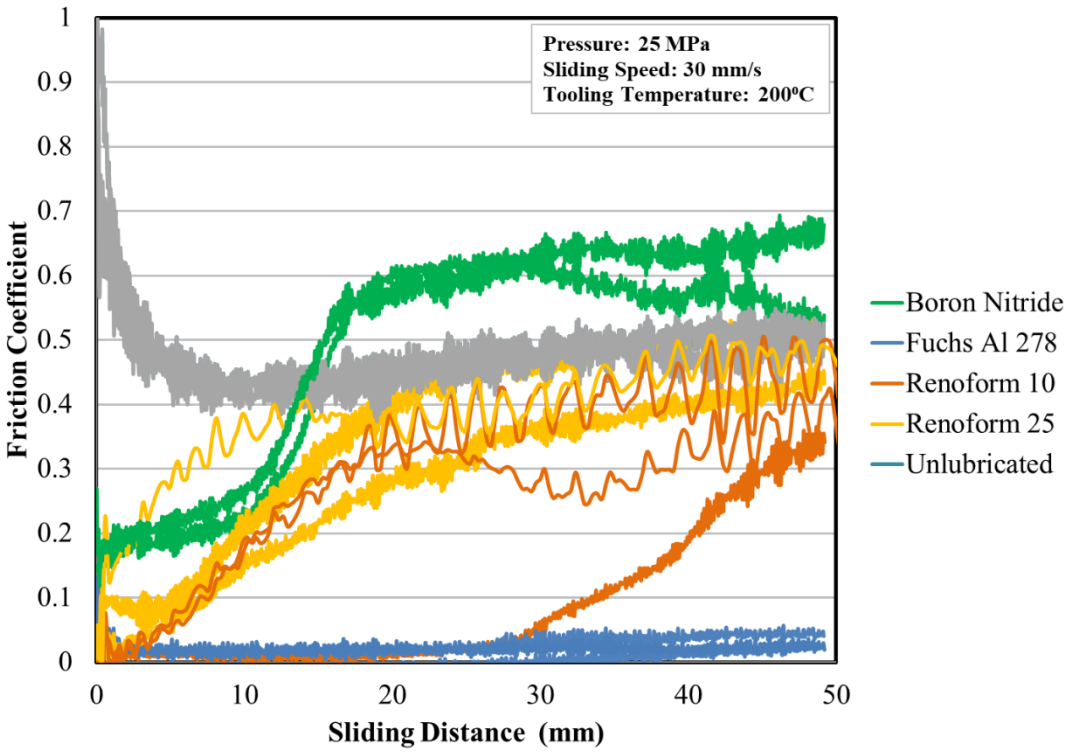

Figure 36: TCT test results of different lubricants for a solutionized blank and tooling temperature of 200°C

3.3 Effect of Die Coating on Lubricant Performance

The friction characterization experiments utilizing the DLC coating primarily considered the Fuchs AL278 lubricant, mainly due to the excellent performance obtained using the uncoated cups. The results for the Fuchs AL278 lubricant with DLC coated cups at room temperature tooling are shown in Figure 37. While the experiments exhibit a fair level of noise, it is evident that the Fuchs lubricant + DLC interface exhibited a gradual rise in friction from 0.038 to 0.075 over the duration of sliding. This increase is attributed to the cooling of the specimen during the test, as seen in Figure 32 and Table 4 in Section 2.2.5, which indicates the average test temperature to be 90°C. Interestingly, the average coefficient of friction increased from a value of 0.017 without coating to 0.055 with added DLC coating. Averages were taken from 6 mm of sliding onwards to avoid the including the static coefficient of friction in the averaging.

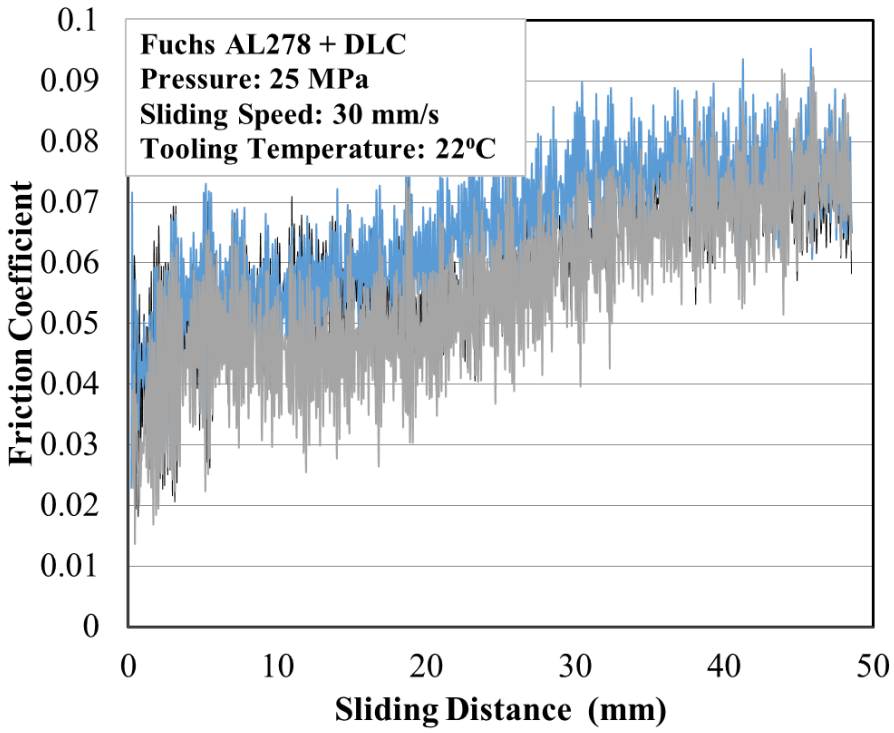

Figure 37: Friction versus sliding distance for DLC + Fuchs AL278 coated cups at 22°C Tooling Temperature and a solutionizing temperature of 470°C

Figure 38 highlights that the lubricant remains intact for a tooling temperature of 22ºC, as made evident by the layer of white film on the cup surface in the microscope image (bottom left). The surface of the test cup looks largely unchanged after the test is conducted. Only some minor burring on the edge of the cup occurs. Very minor scoring is exhibited on the sheet specimen, this is likely due to an imperfect cup edge, the dry white film on the test cup is characteristic of this lubricant.

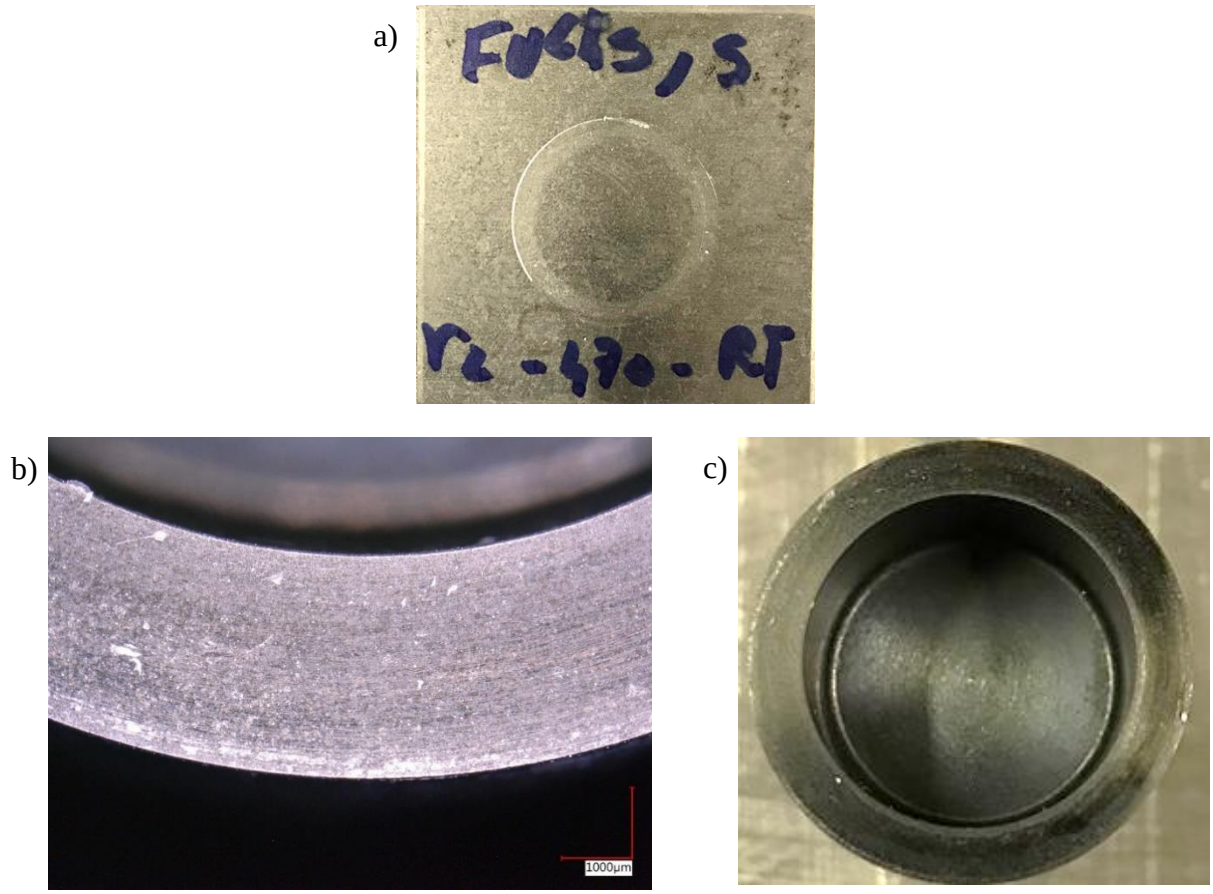

Figure 38: DLC + Fuchs AL278 coated cups at 22ºC tooling temperature and a solutionizing temperature of 470ºC: sheet specimen after testing (a), test-cup optical microscope photo after testing (b) and test cup after testing (c)

Figure 39 presents the friction response for DLC coated cups with Fuchs lubricant and a tooling temperature of 200°C. The TCT apparatus was slightly misaligned for this test condition causing some oscillatory measured frictional response; nonetheless, the measured friction coefficients remain very low. When the tooling temperature is set to 200°C, the average test temperature is

240ºC as seen in Table 4 in Section 2.2.5. The elevated test temperature reduces the friction coefficient compared to that for the RT tooling, since the Fuchs is primarily a warm forming lubricant and performs best at intermediate temperatures near 200ºC [133]. Similar to the non-coated tooling, the average coefficient of friction for this test condition is about 60% lower than that with the room temperature tooling. For uncoated cups the decrease in COF between room temperature tooling and a tooling temperature of 200ºC is 25%.

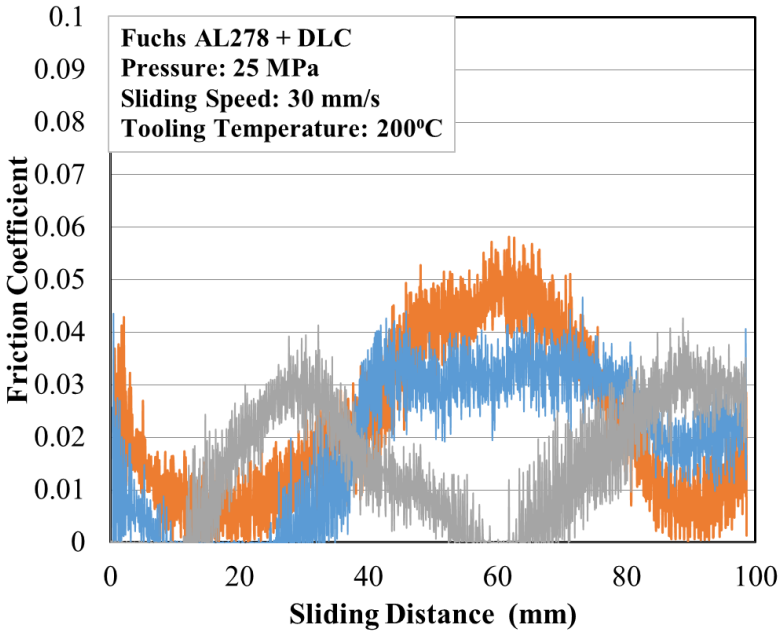

Figure 39: Friction versus sliding distance for DLC + Fuchs AL278 coated cups at 200ºC Tooling Temperature and a solutionizing temperature of 470ºC

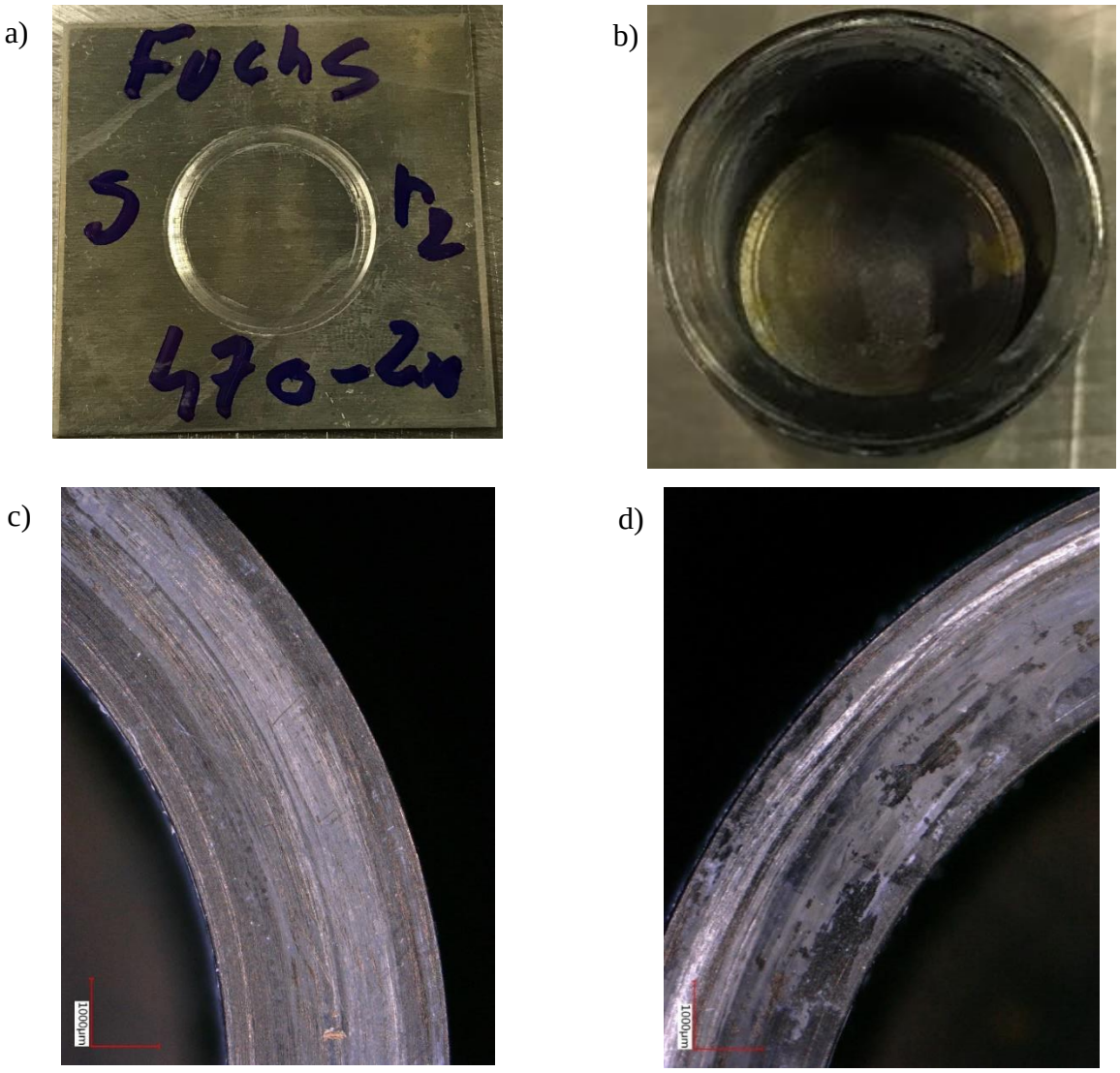

Figure 40: DLC + Fuchs AL278 coated cups at 200ºC Tooling Temperature and a solutionizing temperature of 470ºC TCT Friction Response; sheet specimen after testing (a), test cup after testing (b), test-cup microscope photo after testing (c, d)

As mentioned above, the lubricant is most effective at this temperature condition. The optical microscope of the cup surface seen in Figure 40 displays a “smearing” effect of the lubricant. According to Fuchs [101], this smearing is a physical indication of lubricant activation. The misalignment of the equipment caused some scoring on the sheet specimen.

Figure 41 presents the friction response for DLC coated cups with Fuchs AL278 lubricant and a tooling temperature of 300°C. At this high tooling temperature, lubricant performance is compromised and unstable for two of the three repeats. This lack of repeatability indicates a transition point to instability somewhere between tooling temperatures of 200 and 300°C. Noder *et al.* [101, 133] reported this transition temperature to be 230°C after 21 mm of sliding under warm forming conditions. The DLC coating did, however, prevent aluminum adhesion almost completely, as seen in Figure 42 for the somewhat stable test condition (light blue curve), and only minor adhesion was exhibited on the edge of that cup face. Note that higher levels of adhesion were exhibited for the breakdown cases.

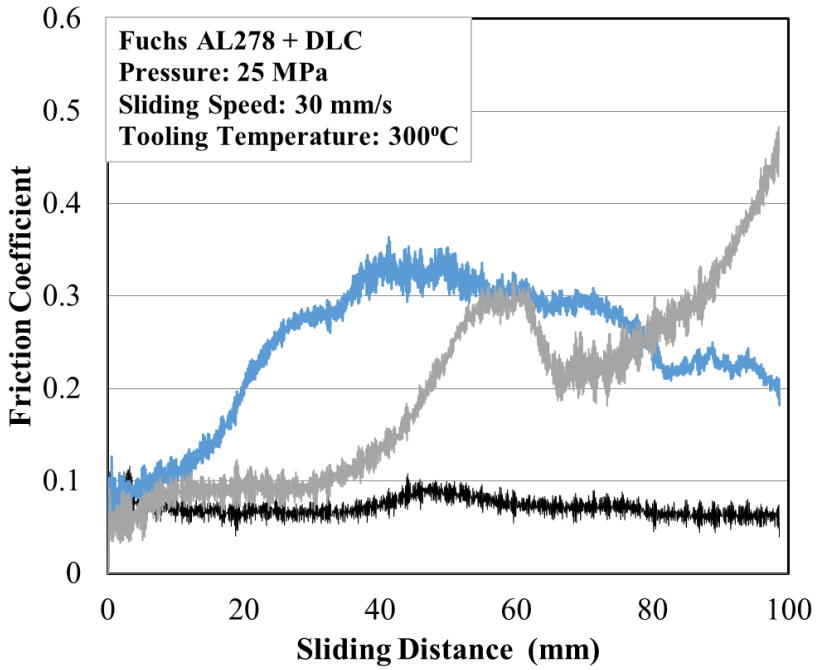

Figure 41:Friction versus sliding distance for DLC + Fuchs AL278 coated cups at 300°C Tooling Temperature and a solutionizing temperature of 470°C

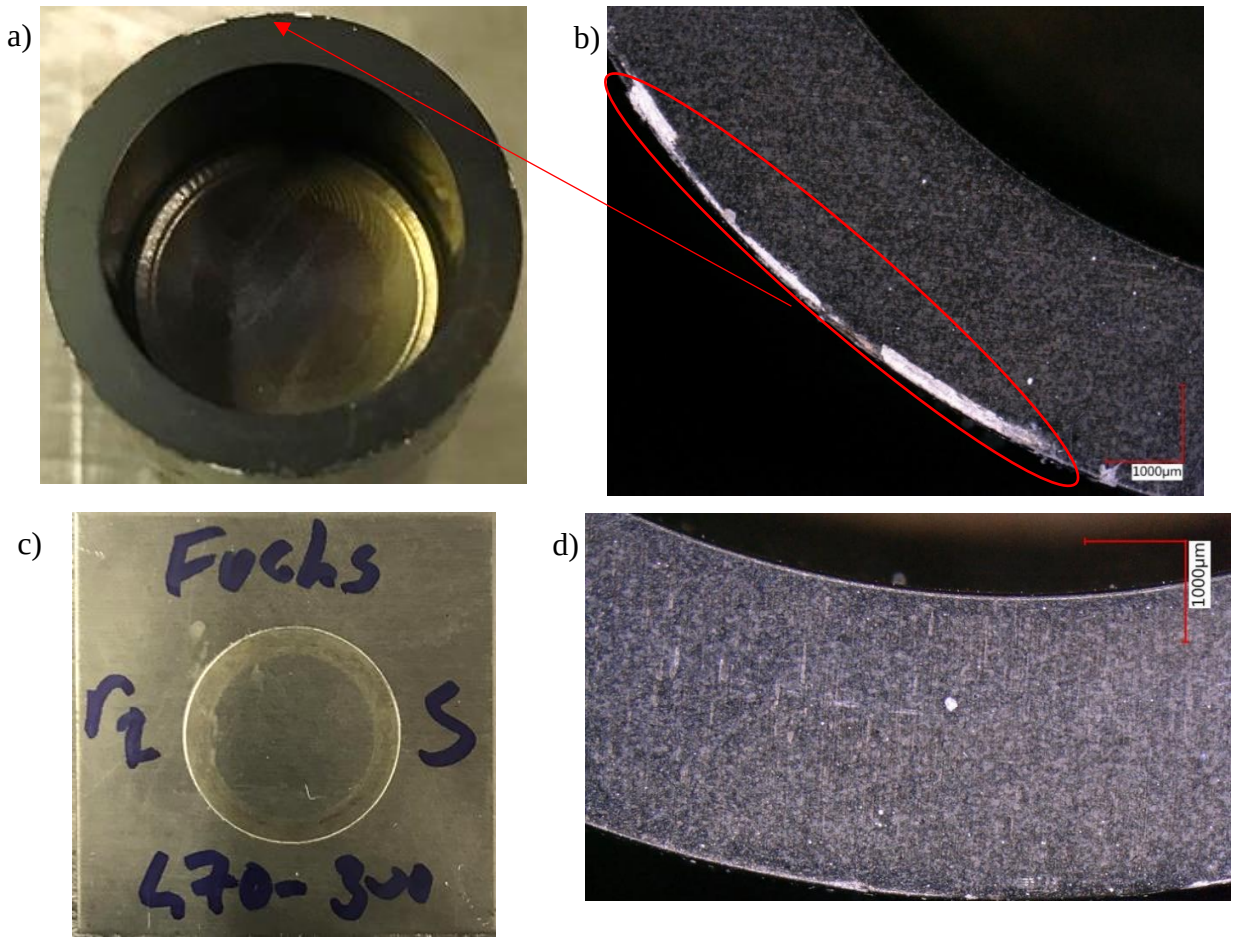

Figure 42: DLC + Fuchs AL278 coated cups at 300°C Tooling Temperature and a solutionizing temperature of 470°C TCT Friction Response; test-cup (a), test-cup under microscope (b), sheet specimen after testing (c), test-cup under microscope (d)

Figure 43 presents the friction response for DLC coated cups with Fuchs AL278 lubricant and a tooling temperature of 350°C. A complete breakdown of the Fuchs AL278 lubricant is exhibited for this test condition. The average friction coefficient is about ten times that seen with RT tooling. A higher amount of aluminum adhesion is seen on the cup specimen, especially on the edges, as made evident in Figure 44, in which aluminum is easily identifiable due to its high reflectivity (circled in red).

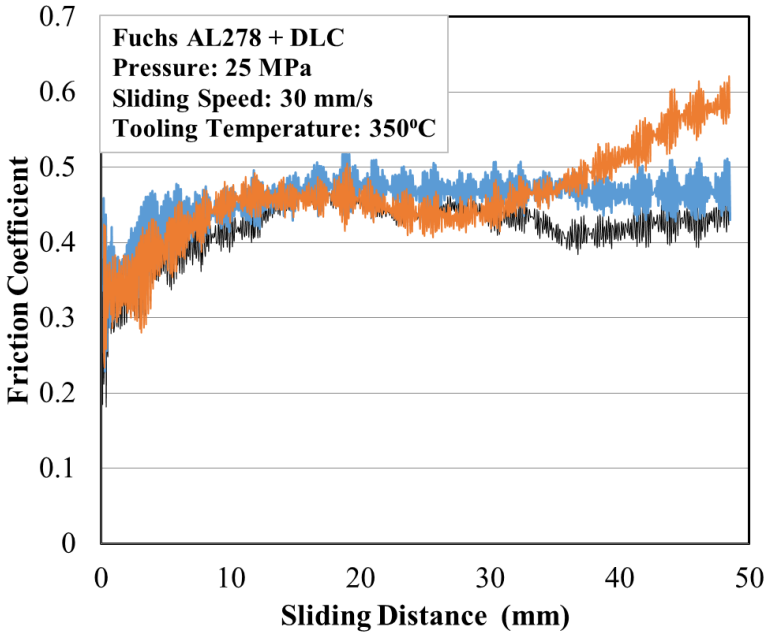

Figure 43: Friction versus sliding distance for DLC + Fuchs AL278 coated cups at 350°C Tooling Temperature and a solutionizing temperature of 470°C

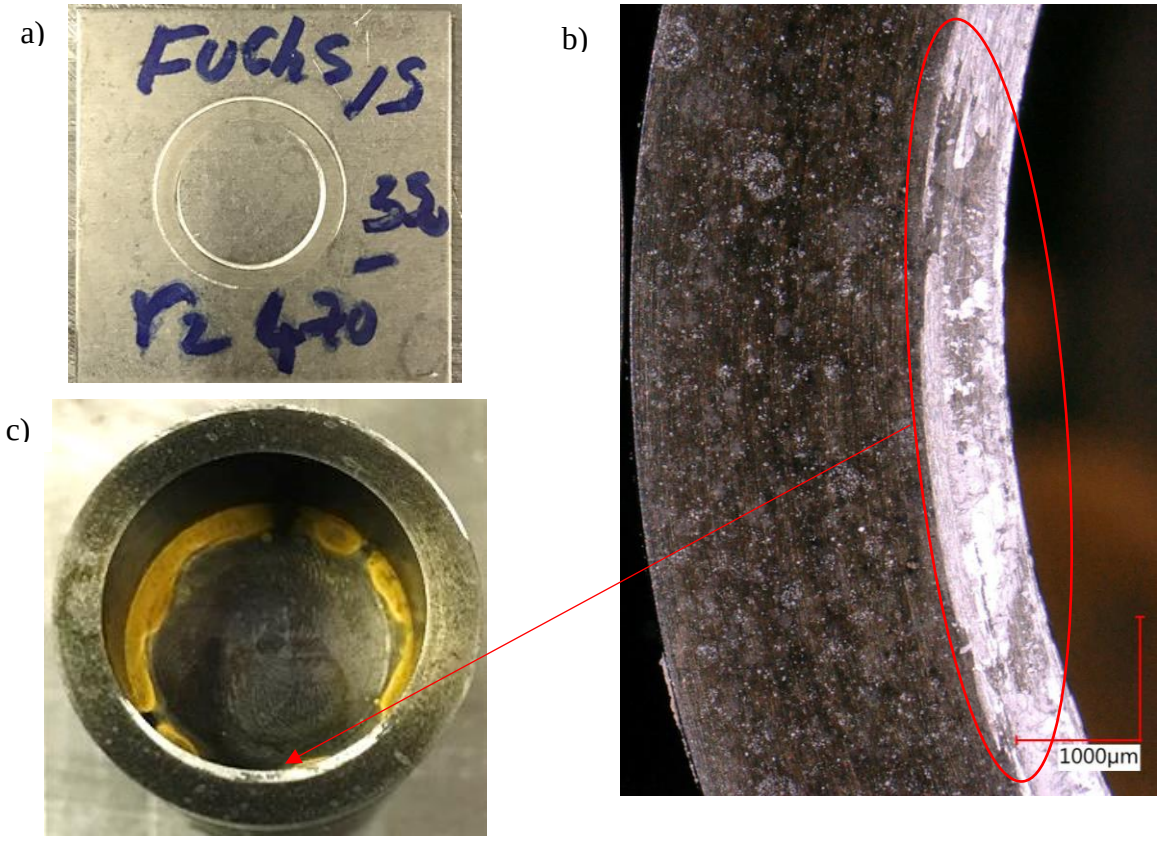

Figure 44: DLC + Fuchs AL278 coated cups at 350°C Tooling Temperature and a solutionizing temperature of 470°C TCT Friction Response; Sheet specimen after testing (a), test-cup microscope photo after testing (b) and test cup after testing (c)

Figure *45* presents the friction response for DLC coated cups with Fuchs lubricant and a tooling temperature of 400°C. Some adhesion of test cups to the sheet specimen was exhibited during this test; the cup would stick momentarily on the sheet and then break free. The friction coefficient is completely unstable and rises to an average value of 0.78 at 50 mm sliding distance. Excessive amounts of aluminum pickup are seen almost everywhere on the cup face (Figure 46c) as well as possible DLC coating failure.

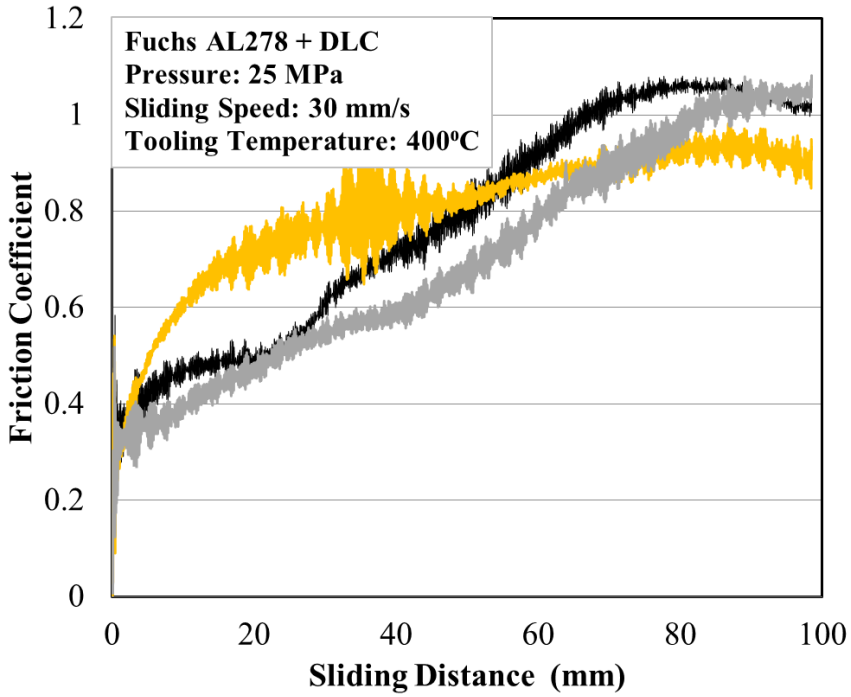

Figure 45: Friction versus sliding distance for DLC + Fuchs AL278 coated cups at 400°C Tooling Temperature and a solutionizing temperature of 470°C

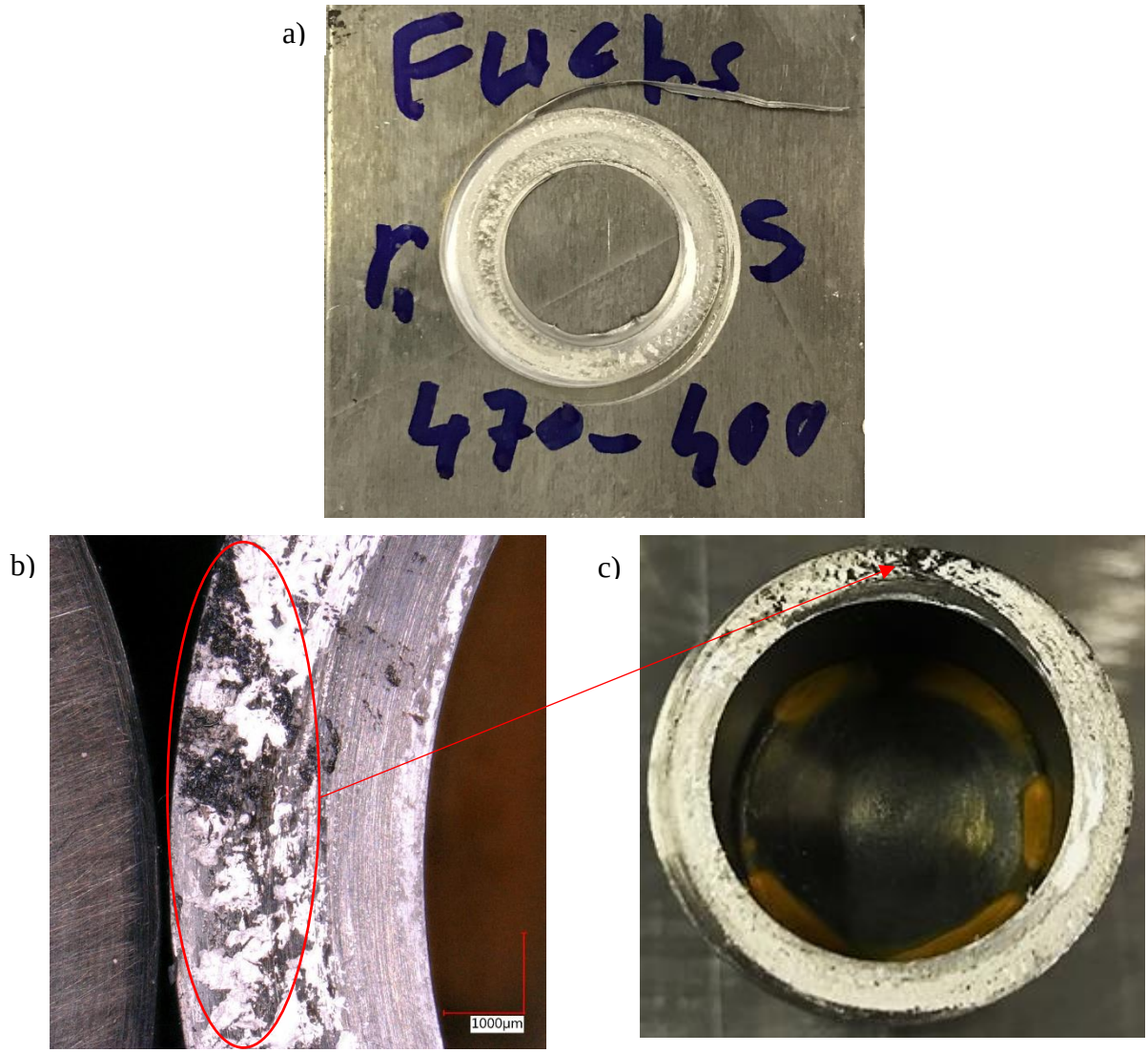

Figure 46: DLC + Fuchs AL278 coated cups at 400ºC Tooling Temperature and a solutionizing temperature of 470ºC TCT Friction Response; Sheet specimen after testing (a), test-cup microscope photo after testing (b) and test cup after testing (c)

Figure 47 serves to summarize the effect of the test temperature and die coating on the tribological response, comparing the average COF of the Fuchs lubricant with and without the DLC coating on the cup for different tooling temperature conditions. The COF was averaged from 6 mm of sliding distance onwards. The scatter bands correspond to the standard deviation between all repeats of each test condition. The COF values with room temperature cups with and without DLC coating are almost identical, with the DLC coated cups having a slightly higher coefficient overall. At 200ºC tooling, the COF for both coated and uncoated cups drops significantly, with uncoated

cups having a noticeably higher COF. As the tooling temperature increases beyond 200ºC the Fuchs AL278 lubricant loses lubricity (wax melting point: 275°C) resulting in a higher COF. Up to 300°C, the DLC coating provides additional stability by maintaining a relatively low COF at higher temperature by reducing adhesion to the cup. At 350°C, both the coated and uncoated cups perform similarly, with uncoated cups having a slightly lower COF. In general, the die coating increases surface hardness, which reduces affinity for adhesion of the aluminum to the die surface thereby increasing tool life. This, however, does increase the likelihood of a plow mechanism becoming operative, which means at low temperature, the cups with DLC coating will have a higher COF. The plow mechanism occurs when a tool surface is hardened. The asperities on the hardened surface are less likely to plastically deform when coming into contact with asperities of a softer surface. Therefore, the asperities of the hardened surface will plow through the softer surface. At high temperature, the adhesive mechanism for wear dominates and the addition of DLC coating will prevent the COF from increasing dramatically as compared to uncoated cups up to a threshold temperature, Noder [101] also reported similar conclusions.

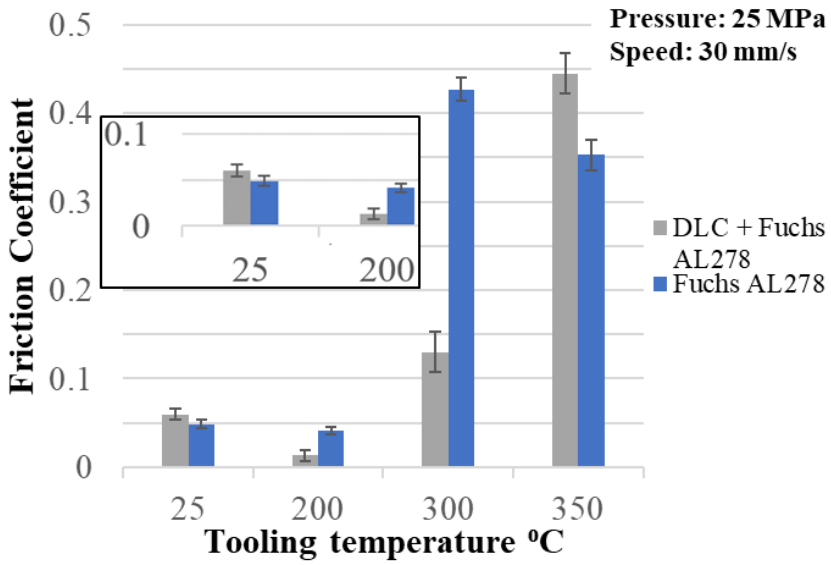

Figure 47: Influence of die coating on the coefficient of friction for solutionized blank, tooling temperatures 25, 200, 300 and 350ºC, 25 MPa contact pressure and 30mm/s sliding speed.

3.4 Effect of Interfacial Pressure and Sliding Speed

To expand the friction characterization for numerical model implementation, the effect of sliding speed and contact pressure were also considered since, in a real forming operation, both of these parameters are variables. This sub-section demonstrates the effect of contact pressure and sliding speed on tribological response.

For this set of experiments, the sheet specimens were solutionized at 470°C for 15 min and then quickly transferred to the TCT, as was done for the experiments reported above. The tooling temperature was set to 300°C. The cups used for this study were uncoated. To test the effect of axial pressure, two axial pressures were used, 10 MPa and 30 MPa. On the other hand, to test the effect of sliding speed, the sliding speeds used were 5 mm/s and 30 mm/s.

In any given forming operation, the interfacial pressure between the die and workpiece varies greatly, therefore, it is important to know the effect this has on tribological response. Figure 48 shows the COF response for a tooling temperature of 300°C and contact pressure of 10 MPa compared to 30 MPa. All three repeats of each test condition are also shown in Figure 48. Both the 10 and 30 MPa conditions start at similar COF values due to initial static coefficient of friction. The 30 MPa test condition has a relatively constant, high COF as the sliding distance increases. On the other hand, the COF for the 10 MPa test condition initially drops from 0.5 to ~ 0.28 as the cup starts to rotate, then it increases steadily until it reaches the COF level seen in the 30 MPa case at around 70 mm sliding distance. The lower pressure results in a smaller true contact area, which delays lubricant breakdown and reduces the effect of the tribological adhesion mechanism, therefore resulting in a lower initial COF. As the test progresses, adhesion of aluminum to the cup starts to build up and the COF rises.

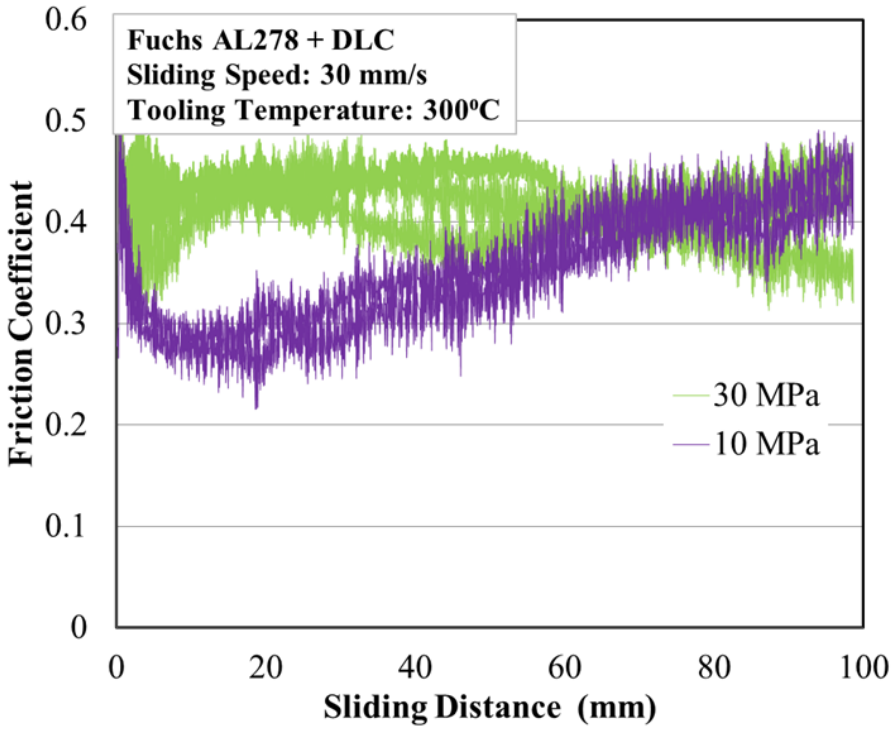

Figure 48: Effect of interface pressure on the coefficient of friction for a pressure of 10 MPa

Figure 49 presents the effect of sliding speed on tribological response, for sliding speeds of 5 and 30 mm/s. Similar to the lower pressure (10 MPa) test condition seen in Figure 48, a lower sliding speed (10 mm/s) results in an initial drop in the COF as the cup overcomes the static friction coefficient. The initial static coefficient is 0.34 and the COF drops to 0.22 shortly after sliding commences. The COF then steadily increases at a low rate until it reaches an average value of 0.32. At 30 mm/s the friction response is significantly elevated with a COF that fluctuates around 0.42.

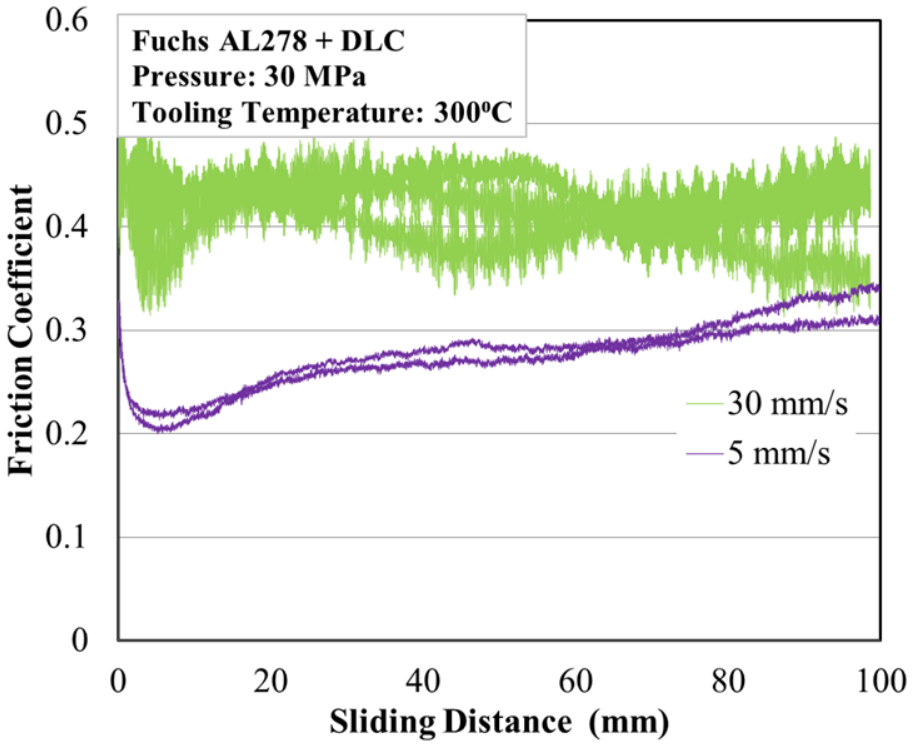

Figure 49: Effect of sliding speed on the coefficient of friction for a sliding speed of 5 and 30 mm/s with Fuchs AL 278 lubricant, tooling temperature of 300ºC and Pressure of 30 MPa

3.5 Friction Characterization - Summary

Friction characterization under die quench conditions using the TCT apparatus has revealed breakdown of the Renoform 25 and Renoform 10 both exhibited poor performance at 200°C. The boron nitride showed good performance at 200°C tooling temperature, but with an elevated friction coefficient. The Fuchs AL278 had the best performance with an average COF of 0.05 for tooling temperature of 200°C. The Fuchs AL 278 was tested with DLC coated cups at various tooling temperatures. The addition of the DLC coating was found to increase the COF for room temperature tooling; this trend is reversed for tooling temperatures of 200 and 300°C, whereas for tooling temperature of 350°C breakdown occurs. At 300°C tooling temperature, lubricant breakdown occurred for two of three repeat trials, while at tooling temperatures of 350 to 400°C mild to excessive aluminum adhesion onto the test cup was exhibited.

Variation of contact pressure study showed that a low contact pressure (10MPa) results in an initially low relative COF, which increases monotonically over the sliding distance. A high pressure (30 MPa) produces a high COF with oscillatory behaviour. Variation of sliding speed showed a low speed (5 mm/s) results in a low COF which increases monotonically as the test progresses whereas a high speed (30 mm/s) results in a high COF with oscillatory behaviour.

4 Constitutive Model for Simulation of DQ Forming

The experimental tensile test results used for fitting the constitutive model were obtained from two separate studies reported by Omer *et al.* [54] and Wang *et al.* [119]. Both data sets comprised a series of elevated temperature tensile tests at a range of strain rates. This chapter begins by presenting the constitutive fits put forward by Omer *et al.* and Wang *et al.* This is followed by the introduction of a proposed new constitutive model intended to capture the behaviour of AA7075 during die quenching. This model is first applied to fit the Omer *et al.* [54] dataset, designated the "Omer-fit". A tensile test FE model is presented next, which allows the direct comparison between the two experimental data sets and helps to identify differences in the hardening behavior between the two data sets. Lastly, the proposed constitutive fit for the Wang dataset, designated the "Wang-fit", is presented.

4.1 Previous Constitutive Characterization and Modeling Efforts

4.1.1 Omer *et al.* Constitutive Characterization Effort

The constitutive data acquired by Omer *et al.* [54] utilized a novel post-processing technique referred to as the Area Reduction Method to account for the minimum true cross-sectional area when calculating the true stress. Omer *et al.* [54] also utilized DIC technology to compute true strain locally rather than over the entire span of the gauge. In contrast, Wang *et al.* [119] obtained the engineering strain from the crosshead displacement of the tensile frame and obtained the engineering stress from the load cell data. The true stress-strain values were then computed from the engineering values using Eq. 2 and Eq. 3.

In this manner, the Wang *et al.* dataset should be viewed as a "bulk measure" corresponding to the average true strain within the gauge length of the specimen, whereas the Omer *et al.* dataset corresponds to the local true strain and stress at the minimum cross-section. This distinction complicates direct comparison of the two datasets, as addressed in Section 4.3.1. Omer et al. [54] fit a modified Voce model to their true stress-strain data of the form:

$$\sigma = A + \left(B + C\sqrt{\varepsilon_p}\right) - 1 - exp\left(-D\varepsilon_p\right) \quad \text{(Eq. 9)}$$

where A, B, C and D are phenomenological parameters. The coefficients in Eq. 9 are generally taken as constants for a given temperature and strain rate. In work by Omer *et al.* [54], each coefficient was replaced with a polynomial function to capture the temperature and strain rate sensitivity, as shown in Table 7.

Parameter	AA7075
***A* (MPa)**	$154.1 - 235.2T_r + 487.2T_r^2 - 381.7T_r^3$
***B* (MPa)**	$1643\dot{\varepsilon}^2 - 961\dot{\varepsilon} + 186 + (83.8\ln\dot{\varepsilon} + 3.2)T_r + (-404.8\dot{\varepsilon} + 209.2)T_r^2$
***C* (MPa)**	$251.3 - 142.5T_r - 113.5T_r^2$
***D* (mm/mm)**	$17.6 + 43.2T_r$

Table 7: Coefficients for Modified Voce Constitutive Formulation by Omer et al. [54]

4.1.2 Wang *et al.* Constitutive Characterization Effort

Wang *et al.* [119] used a similar approach for to model their data, utilizing a modified Misiolek constitutive model with embedded temperature and strain rate dependent polynomials, shown in Eq. 10 and in which C, m and n are equation coefficients,

$$\sigma = C\varepsilon^n \exp(m\varepsilon) \text{ (Eq. 10)}$$

which can also be expressed as:

$$\ln(\sigma) = I(C) + n\ln(\varepsilon) + m\varepsilon \text{ (Eq. 11)}$$

Parameter	Equation
$\ln(C)$	$\ln(C) = C_1T^5 + C_2T^4 + C_3T^3 + C_4T^2 + C_5T + C_6$
n	$n = n_1T^5 + n_2T^4 + n_3T^3 + n_4T^2 + n_5T + n_6$
m	$m = m_1T^5 + m_2T^4 + m_3T^3 + m_4T^2 + m_5T + m_6$
C_i	$C_i = C_{i1}\dot{\varepsilon}^3 + C_{i2}\dot{\varepsilon}^2 + C_{i3}\dot{\varepsilon} + C_{i4}$
n_i	$n_i = n_{i1}\dot{\varepsilon}^3 + n_{i2}\dot{\varepsilon}^2 + n_{i3}\dot{\varepsilon} + n_{i4}$

Table 8: Coefficients for Modified Misiolek constitutive formulation [119]

4.1.3 Accuracy and Validity of Previous Constitutive Models

The use of polynomial expressions to capture temperature- and strain rate-dependence, as proposed by Omer *et al.* [54] and Wang *et al.* [119], offered good correlation between the constitutive fits and the experimental results. However, the use of polynomial functions in physical problems can be misleading at times, especially if the model is extrapolated to other temperatures and strain rates, which is often the case in FE simulations. Another reason to consider a different constitutive fit is to extend the plastic strain range for which the model remains accurate; the modified Voce fit along with polynomial coefficients lacks accuracy, as made evident in Figure 50.

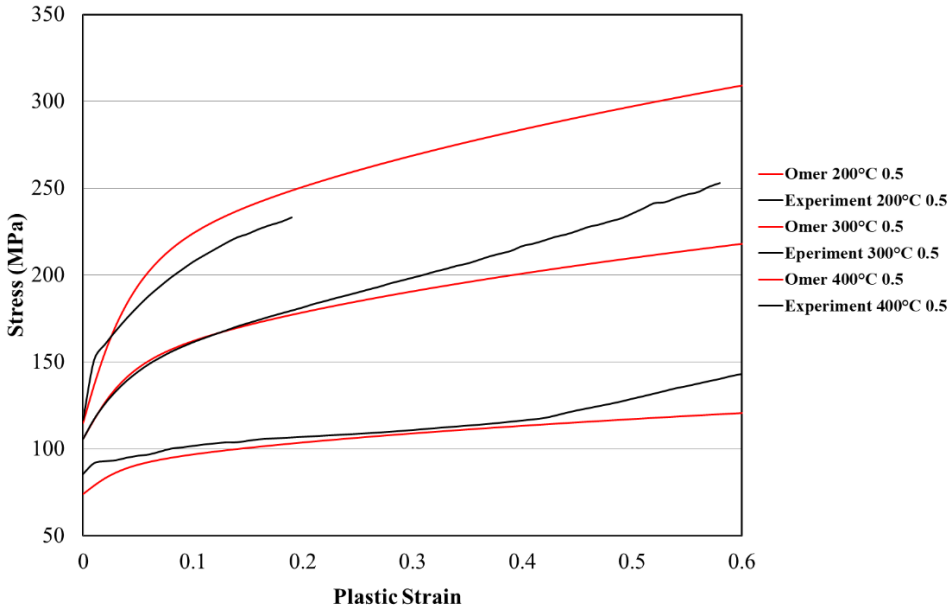

Figure 50: Modified Voce fit performed by Omer et al. [54] for 200, 300 and 400°C at 0.5 s^{-1} strain rate [54] and corresponding experimental data [54].

4.2 New Constitutive Model and Omer-fit

In the current work, a more physically based constitutive model was developed. The proposed constitutive model is derived starting with a version of the Zerilli-Armstrong model [135], which was originally proposed for HCP materials, given by Eq. 12.

$$\bar{\sigma} = C_0 + \left(C_1 + C_2\sqrt{\bar{\varepsilon_p}}\right)\exp\left((-C_3 + C_4 \ln \dot{\varepsilon}_p)\, T\right) + C_5\bar{\varepsilon_p}^n \qquad \text{(Eq. 12)}$$

The Zerilli-Armstrong model is a physically derived model in which C_0 presents the contribution due to solute content and initial dislocation density; the term $\left(C_1 + C_2\sqrt{\bar{\varepsilon_p}}\right) exp\left((-C_3 + C_4\, ln\, \dot{\varepsilon}_p)\, T\right)$ is derived based on the thermal activation energy needed for dislocation motion. This model features fixed value coefficients, which amounts to a single equation in which strain, temperatures and strain rates are independent variables from which the flow curve for a specific condition is predicted.

A modified version of the Zerilli-Armstrong model was developed, as given by Eq. 13. The modifications completely decouple the yield stress component C_1 from the initial hardening component C_2, by multiplying each coefficient with a separate term of the form $exp\left((-C_n + C_n\, ln\, \dot{\varepsilon}_p)\, T\right)$ term (the subscript *n* is a placeholder since this term is repeated multiple times in the constitutive equation). Additionally, the exponent of the plastic strain in the term $\left(C_1 + C_2\sqrt{\bar{\varepsilon_p}}\right)$ from Eq. 12, which is responsible for initial hardening response, is switched from 0.5 and made temperature dependent. Lastly, the prolonged hardening response, dominated by the term $C_5\bar{\varepsilon_p}^n$ in Eq. 13, is also made temperature dependent; this modification was first introduced by Kurukuri *et al.* [134] for a magnesium alloy (ZEK 100).

$$\bar{\sigma} = C_0 + C_1 \exp\left((-C_3 + C_4 \ln\ \dot{\varepsilon_p})T\right) + C_2 \bar{\varepsilon_p}^{C_{10} exp\left(1-\left(\frac{T-273}{743}\right)\right)} \exp((-C_5 + C_6 \ln\ \dot{\varepsilon_p})T) + (C_7 - C_8 T)\bar{\varepsilon}_p^{C_9} \quad \text{(Eq.13)}$$

Coefficient	Value
C_0 (MPa)	-1.711E+06
C_1 (MPa)	1.711E+06
C_2 (MPa)	6.079E+02
C_3 (1/K)	1.126E-07
C_4 (1/K)	1.126E-08
C_5 (1/K)	6.932E-04
C_6 (1/K)	1.386E-05
C_7 (MPa)	3.441E+02
C_8 (MPa/K)	9.046E-01
C_9	3.646E-01
C_{10}	2.193E-01

Table 9: Coefficients for modified Zerilli-Armstrong constitutive formulation

A subset of the temperature conditions considered by Omer *et al.* [54] were used for the modified Zerilli-Armstrong constitutive fit, namely the 200, 300, 400 and 470ºC temperature conditions. The range of temperature conditions considered was reduced since at low temperature, the rate sensitivity reverses signs and becomes negative due to the Portevin–Le Chatelier (PLC) effect. Under specific conditions of strain rate and temperature, the PLC effect appears as an unstable plastic flow during tensile testing. As the PLC effect takes place, the plastic strain localises as bands that move in a variety of ways along a specimen gauge. This change in rate sensitivity complicates the constitutive fitting unnecessarily since material deformation in the DQ process occurs in the range 200-470ºC. The resulting constitutive fits are seen in Figure 51; this constitutive fit will be referred to as the Omer-fit in the subsequent text.

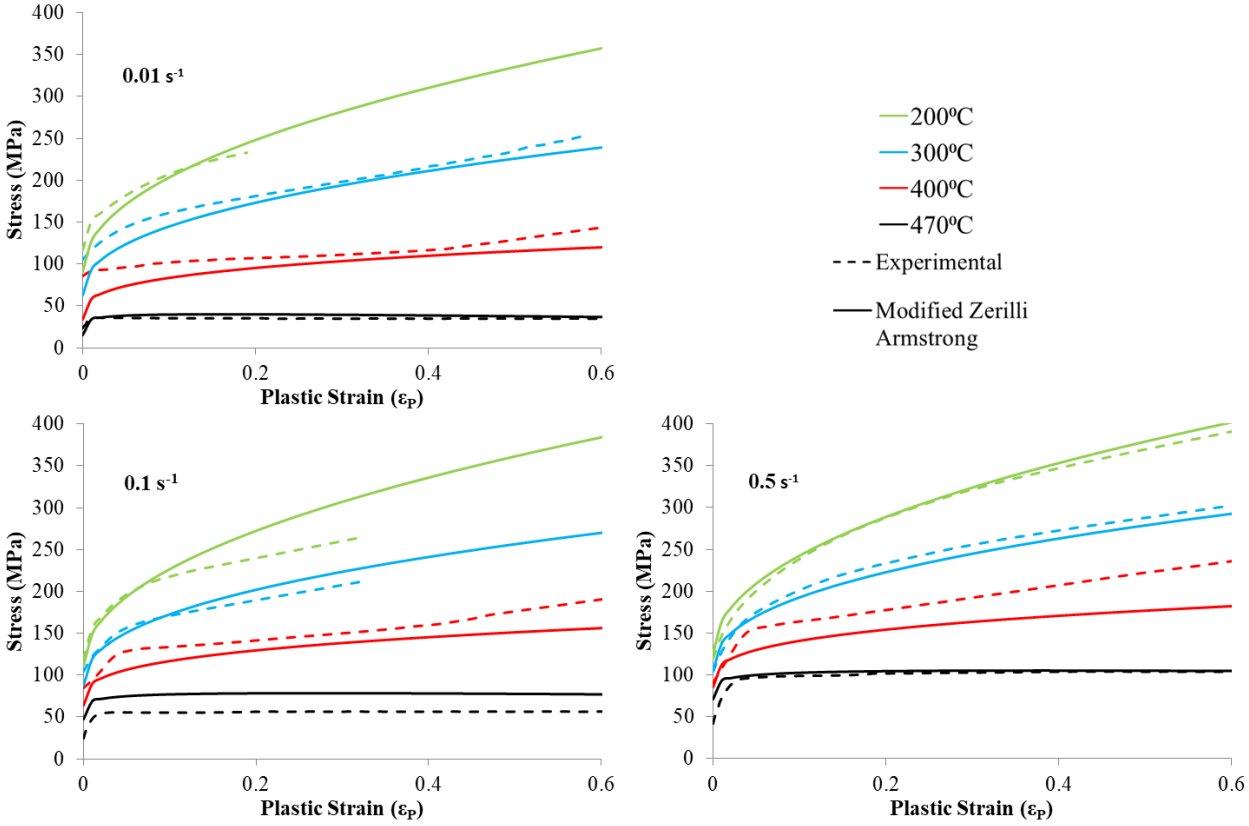

Figure 51: Modified Zerilli-Armstrong constitutive fits for Omer [54] experimental data

Table 10 presents the results of the R-squared error for all test conditions to highlight the goodness of the fit. Good correlation is exhibited between the Omer-fit and the experimental dataset, except for the 470°C case at a strain rate of 0.01 for which the R^2 value is 0.7798.

		Temperature			
		200°C	**300°C**	**400°C**	**470°C**
Strain Rate	**0.01 s^{-1}**	0.9982	0.9902	0.8776	0.7798
	0.1 s^{-1}	0.9876	0.9962	0.9556	0.8721
	0.5 s^{-1}	0.9983	0.9981	0.9820	0.9379

Table 10: R-squared residuals of the Omer-fit vs. experimental data for all temperature and strain rate conditions

4.3 Model Validation and Dataset Comparison

Since the strain and stress measurement method differs between the constitutive data reported by Omer *et al.* [54] and that published by Wang *et al.* [119], the hardening response is not directly comparable. Wang *et al.* [119] averages the strain over the entire gauge length whereas Omer *et al.* [54] measures the local strain using DIC and uses the so-called ARM method which corrects the strain and stress measurement past uniform elongation. The datasets also use different tensile geometries. Thus, to enable direct comparison of the hardening response between the two constitutive datasets, a finite element model of the tensile tests was developed, utilizing the specimen geometry in the experiments performed by Wang *et al.* [119].

4.3.1 Tensile FE Model Description

The FE model utilizes the Omer-fit to simulate the material constitutive behaviour but models the specimen geometry from Wang *et al.* [119]. The tensile model shown in Figure 52 is a quarter symmetry isothermal tensile model. The nodes at the specimen grip section are pulled in the positive "x" direction and symmetry boundary conditions are applied at the symmetry planes. The model has a first order quadrilateral mesh, with a 0.5 mm element size and uses fully integrated shell elements. The model utilized the Barlat YLD89 yield surface [120], in conjunction with the Omer-fit constitutive response. The FE model was run for three temperatures, namely 200, 400 and 480ºC, and three strain rates at each temperature, namely 0.01, 0.1 and 1 s^{-1}. These temperatures and strain rates match those tested by Wang *et al.* [119] and are close to the conditions considered by Omer *et al.* [54].

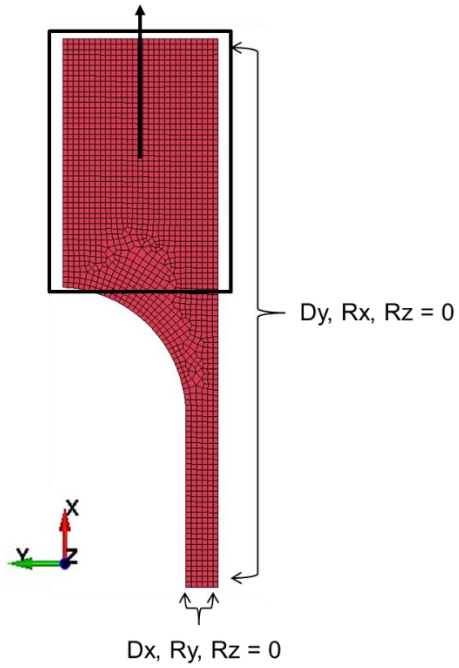

Figure 52: Isothermal Tensile Quarter Symmetry FE Model (modelled after Wang et al. [119] tensile geometry)

4.3.2 Comparison to experiment

The predicted hardening response from the FE tensile model with the Omer-fit is compared to the measured experimental data due to Wang *et al.* [119] for temperatures of 200, 400, 480ºC and strain rates 0.01, 0.1 and 1 in Figure 53. At 200°C, the Wang *et al.* [119] experimental data shows a negative rate hardening trend whereas the Omer *et al.* [54] dataset and the FE predictions exhibit a positive strain rate sensitivity (the Omer *et al.* [54] does not show negative rate sensitivity until temperatures drop below this level). The measured stress levels in the Wang *et al.* [54] experimental results is significantly lower than the predictions using the Omer-fit, although strain rate sensitivity is similar for the two datasets for the 480ºC and 400ºC test conditions. In general, the softer hardening response from the Wang *et al.* [119] experiments result is expected since the strain is averaged over the entire gauge length while at high temperature the local strain could be considerably higher that the average strain over the specimen gauge. Since the stress is calculated based on Eq. 9b, an under predicted strain measurement will result in an under predicted stress

calculation due to an under-estimate of the area reduction. The difference between the two data sets is further examined in Chapter 5 in which predictions are compared to measured load-displacement data from DQ LDH experiments.

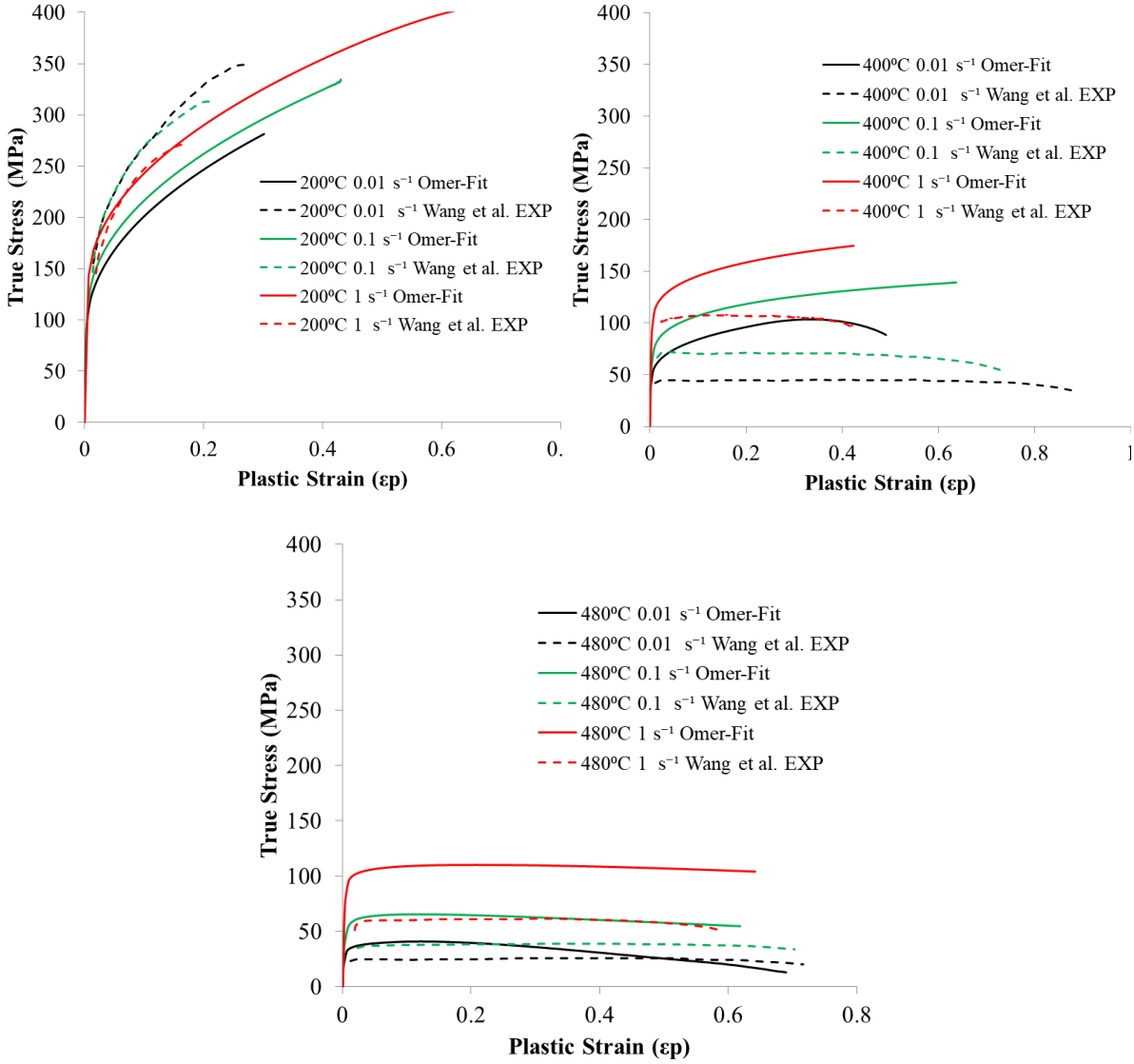

Figure 53: Stress strain curves of the Omer-fit at temperatures 480, 400, 480ºC and strain rates of 0.01, 0.1, 1 s^{-1} compared to the Wang et al. [119] experimental stress-strain curves

4.4 Current Constitutive Model Applied to Wang Dataset

As an alternative to the Omer-Fit, a modified version of Zerilli-Armstrong formulation, shown in Eq. 14, was fit to the Wang *et al.* [119] data set. A small difference exists in this equation versus that used to fit the Omer *et al.* [54] dataset, which is the removal of the second power-law hardening term $(C_7 - C_8 T)\bar{\varepsilon}_p^{C_9}$ which was not needed since the data set had little to no positive hardening at elevated temperature. In addition, the experimental approach taken averages the strain over the entire gauge length, which may exhibit a significant strain gradient at elevated temperature. Averaging the strain over a gauge that has a significant strain gradient could result in under-predicting the hardening rate, meaning the material will appear softer than it is physically. The coefficients resulting from the fitting process are given in Table 11.

$$\bar{\sigma} = C_0 + C_1\, exp\big((-C_3 + C_4 ln\ \dot{\varepsilon_p})T\big) + C_2 \bar{\varepsilon_p}^{\,C_7 exp\left(1-\left(\frac{T-273}{753}\right)\right)}\, exp((-C_5 + C_6 ln\ \dot{\varepsilon_p})T)$$

(Eq. 14)

Coefficient	Value
C_0 (MPa)	-6.064E+02
C_1 (MPa)	9.924E+02
C_2 (MPa)	2.254E+09
C_3 (1/K)	5.045E-03
C_4 (1/K)	2.330E-05
C_5 (1/K)	3.365E-02
C_6 (1/K)	-2.386E-05
C_7	2.457E-01

Table 11: Coefficients for modified Zerilli-Armstrong constitutive formulation, the Wang-fit, to the Wang et al. experimental data set [119]

Nearly all temperature conditions described in Wang *et al.* [119] were used for the modified Zerilli-Armstrong constitutive fit, namely the 200, 300, 360, 440 and 480ºC temperature conditions. The

280ºC temperature condition was the only condition omitted since it exhibited a highly negative hardening rate for a large portion of the flow curve, which would have affected the constitutive fit and caused additional problems with the FE model. The resulting constitutive fits are seen in Figure 54.

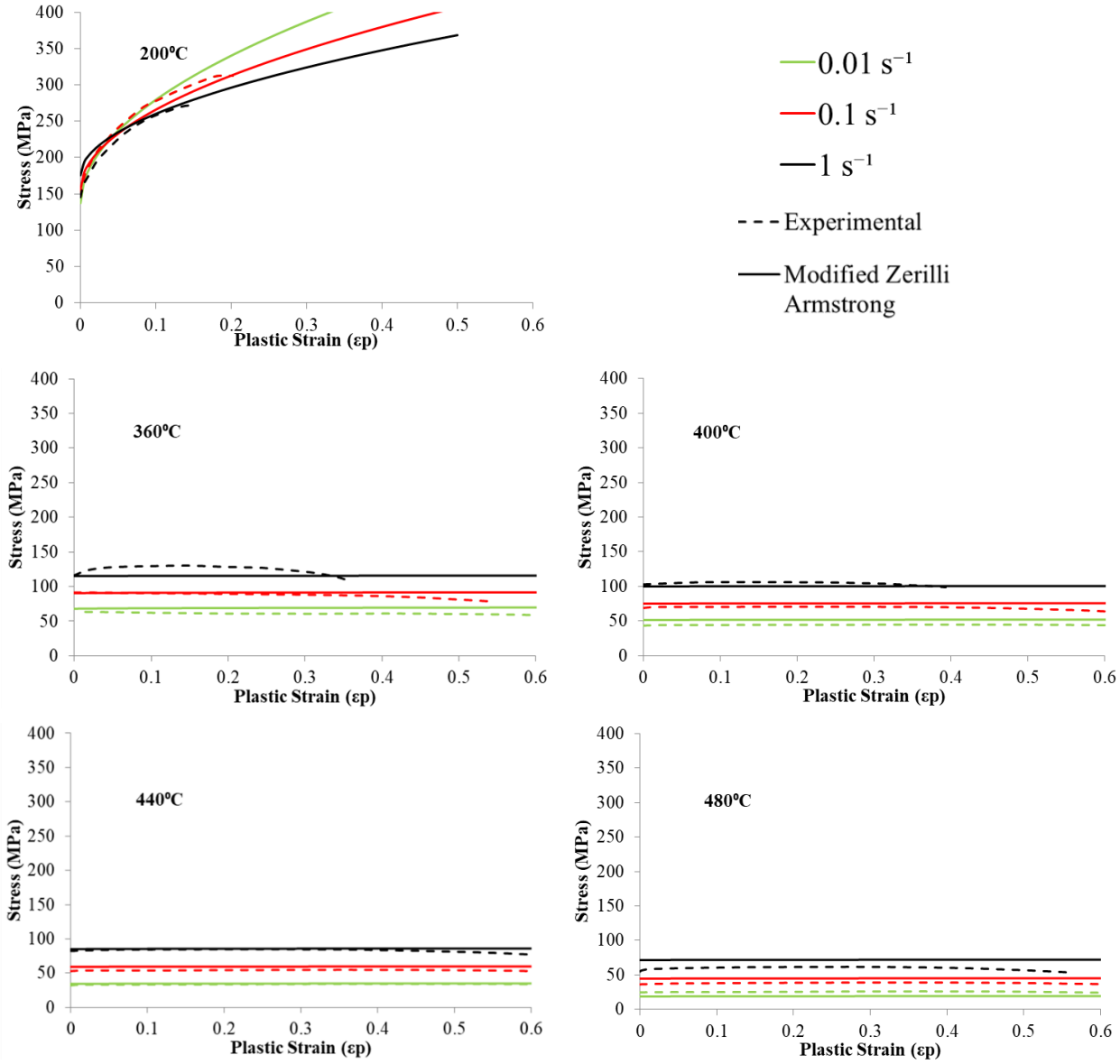

Figure 54: Modified Zerilli-Armstrong constitutive fits for the Wang et al. [119] experimental data

	Temperature

		200°C	360°C	400°C	440°C	480°C
Strain Rate	**0.01 s^{-1}**	0.9979	0.9403	0.9506	0.9843	0.9350
	0.1 s^{-1}	0.9955	0.9233	0.8992	0.9620	0.9933
	1 s^{-1}	0.9963	0.9556	0.9555	0.9855	0.9779

Table 12 presents the R-squared error values for all test conditions to highlight the goodness of the fit. Good to moderate correlation is exhibited between the Wang-fit and the experimental dataset.

		Temperature				
		200°C	**360°C**	**400°C**	**440°C**	**480°C**
Strain Rate	**0.01 s^{-1}**	0.9979	0.9403	0.9506	0.9843	0.9350
	0.1 s^{-1}	0.9955	0.9233	0.8992	0.9620	0.9933
	1 s^{-1}	0.9963	0.9556	0.9555	0.9855	0.9779

Table 12: R-squared residuals of the Wang-fit vs. experimental data for all temperature and strain rate conditions

5 Numerical Simulation of Elevated Temperature Limiting Dome Height Experiment – Model Description

To assess and validate the constitutive models presented in the previous chapter, elevated temperature limiting dome height (LDH) experiments performed by George *et al.* [130] were simulated using a finite element model incorporating the constitutive fits. The predictions of load-displacement response, temperature history, strain distribution and strain history during the LDH experiments for a range of forming conditions were used for validation of the constitutive model. This chapter opens by presenting the experimental set up (Section 0) for the DQ LDH testing by George *et al.* [130]. The chapter closes with a description of the FE model of the LDH DQ experiments (Section 0). The model predictions and comparison with the experimental data due to George *et al.* [130] is given in Chapter 6.

5.1 Limiting Dome Height Experiments

This section details the limiting dome height (LDH) experiments performed by George *et al.* [130] to characterize the formability of AA7075 aluminum alloy sheet under die quenching conditions. This testing was not done as part of the current research; however, the experiments were modelled as part of the validation effort, so an overview of the experimental methodology is presented here. The formability was assessed using temperature-dependent forming limit diagrams, produced via Nakazima hemispherical dome testing using tooling that adheres to the Nakazima test standard [119]. This task was completed using the automated fast form system at the University of Waterloo with *in-situ* Digital Image Correlation (DIC) technology used to evaluate strain. In the following text, the test set up will be presented first, followed by the specimen geometries used, and test parameters adopted and the rational behind the choices made.

The tooling utilized for the formability experiments is shown in Figure 55. The blank is clamped between a pair of flat dies with a 56 mm inner radius and a die entry radius of 8 mm. The fixed Nakazima hemispherical punch has a 50.8 mm radius, resulting in a radial clearance of 3.2 mm for a 2 mm blank. The binder uses spring-loaded lifters that hold the part above the binder until the die moves downwards to clamp the blank against the binder; this significantly reduces heat loss during the clamping stage.

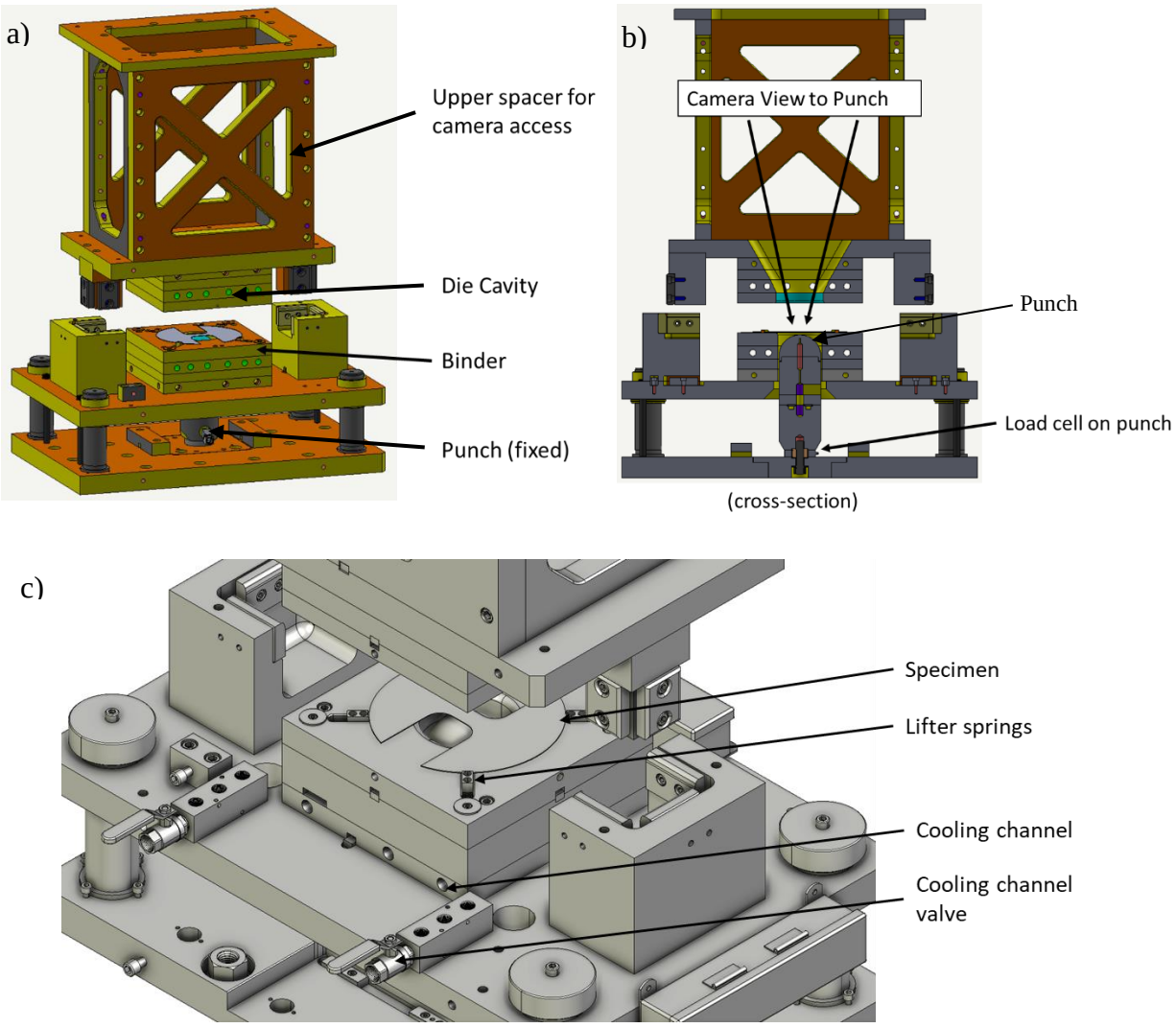

Figure 55: CAD of tooling assembly in isometric view (a) [130], cross section of CAD of tooling assembly (b) [130], close-up CAD isometric view of die assembly (c)

The dies and punch are made from H-13 steel with a measured surface hardness of 50 HRC. The upper die is mounted to the press upper ram, while the upper spacer provides clearance for the DIC cameras; the upper ram is mounted to the inner slide of the servo hydraulic press. Cooling channels are embedded in the die, binder, and punch assembly in which 12ºC chilled water circulates.

The tooling is mounted within a Macrodyne 900 Ton hydraulic forming press. The press capacity is 900 tons, which comprises a main 600-ton cylindrical actuator and a 300-ton outer actuator (not used for the DQ LDH testing). The main actuator can operate at 600-ton capacity for low-speed

approach or 60-ton for a fast speed approach, which was used for the LDH experimental set-up. Pressure transducers are installed in the cylinders and measure fluid pressure that, based on the cylinder cross-sectional area, allows calculation of tool force. The binder is connected to a 150-ton hydraulic cushion, which provides the clamping load required to prevent draw-in of the flange region of the part during forming. The displacement-controlled die has a fast approach speed of 254 mm/s, which is superior to the test speed of 64 mm/s. The die speed is then reduced to test speed, which operates under open-loop control. Once the die contacts the binder, the binder force operates under closed-loop control with a hydraulic actuator located beneath the press. The die and binder continue downwards, and the punch is fixed such that the sheet is formed over the fixed punch. The punch reaction force is measured using a load cell located under the punch mounting point. The binder load chosen was 356 kN which was sufficient to eliminate draw-in.

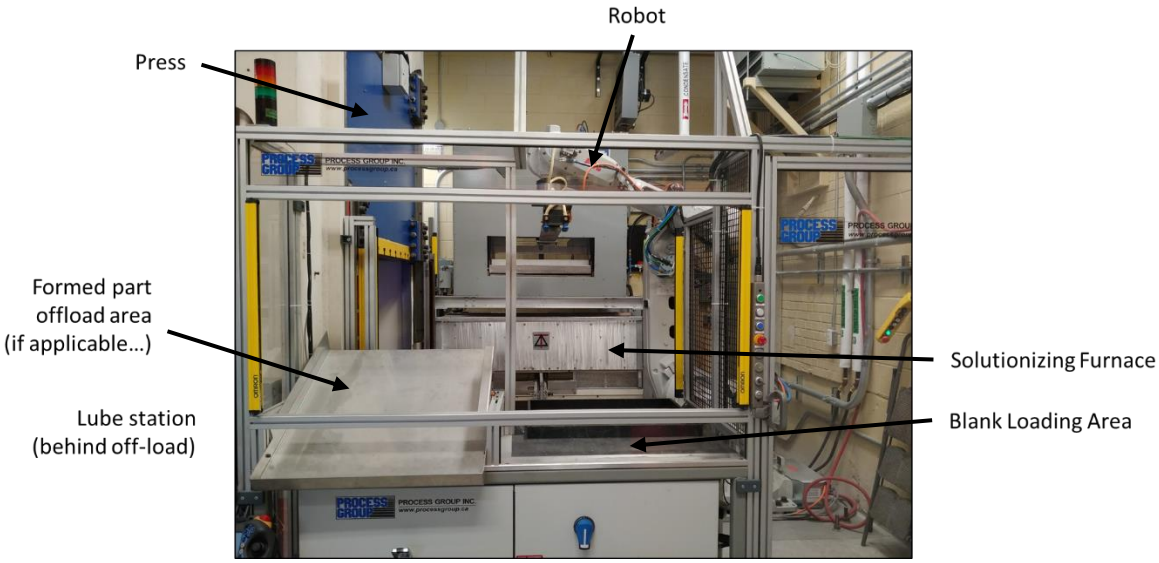

Figure 56: Fast forming set up with press robotic arm and solutionizing furnace [130].

A Deltech industrial convection furnace is used to solutionize the blanks. For rapid and repeatable transfer times, an ABB IRB 6700 industrial robotic arm was used, shown in Figure 56. The robot arm uses an attachment with two gripper systems on opposite ends of the arm. This allows the

robot to handle hot and cold parts. Cold parts going into the furnace are handled using pneumatically controlled suction cups, while hot parts coming out of the furnace are handled using a mechanical gripper that engages the edges of the blanks; both are shown in Figure 57.

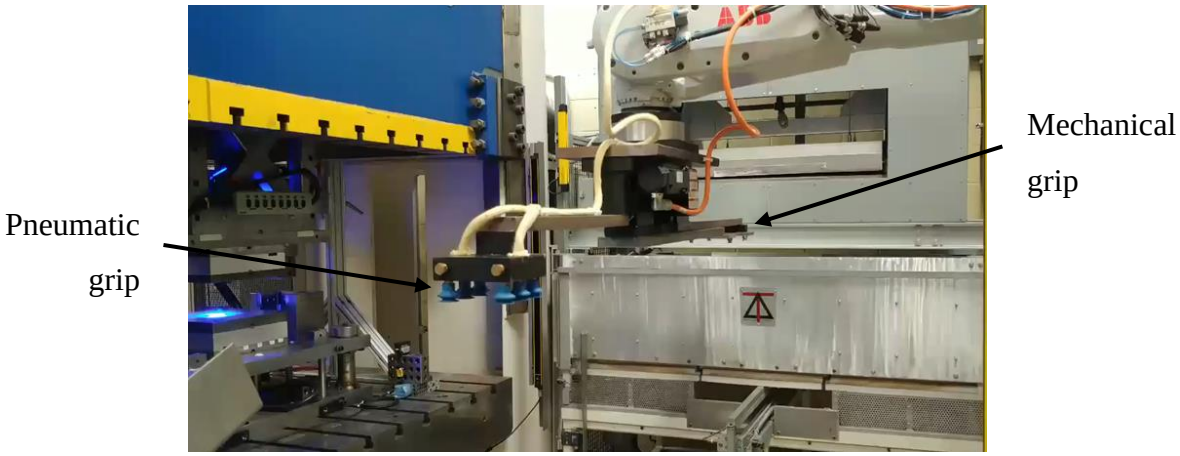

Figure 57: Robot Arm with Mechanical and Pneumatic grip [130].

Strain measurements during LDH testing were performed using stereo digital image correlation (DIC) technology. A pair of Photron AX100 FastCam cameras attached to a pair of 60 mm Nikkor lens with a blue light filter and a blue LED for illumination were used for image acquisition. All DIC analysis was done using Vic 3D [11], a commercial DIC software package. The basic parameters used within the Vic 3D software used for analyzing the DIC data included a step size of 4 pixels, a strain filter of 5 pixels, and a subset of approximately 35 pixels. Based on the physical test setup, the pixel resolution was 10.5 pixels/mm. Figure 58 shows an example of a speckled dome specimen used for DIC strain measurement. The strain limit detection was achieved using the ISO 12004-2:2008 [106] method. The specimens were first bead blasted to create a matte light background to contrast against the black speckle pattern. The black speckled pattern was produced using the VHT Flame Proof high-temperature black thermal paint [120].

Figure 58: Example of speckled LDH specimen for DIC strain measurement [130].

5.1.1 Specimen Geometry

Each Nakazima specimen geometry is designed to have a different strain path, which leads to a different strain state and forming limit. The strain path and forming limit are controlled by the aspect ratio of the gauge region of the specimen. Figure 59 displays the test geometries used in this study. The specimen geometries follow modified versions of the ISO12004-2:2008 standard, with gage widths: 25.4, 76.2 and 152.4 mm.

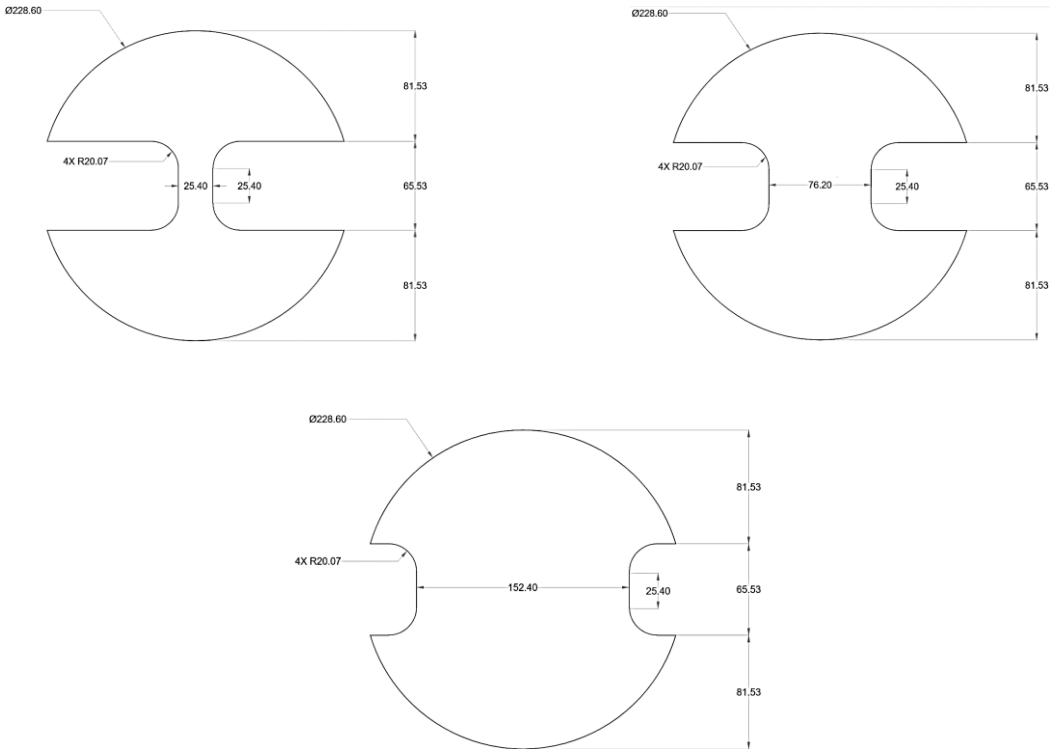

Figure 59: Specimen test geometries [130].

5.1.2 Lubricant

The lubricant used by George *et al.* [130] was a combination of five layers of Teflon sheet with Vaseline applied between layers. The lubricant used in the forming trials differs from those used in the friction characterization effort. The friction characterization work considered high temperature commercial lubricants and die coatings, which work well in a high-volume production setting. For the formability characterization effort, which was a low volume study, the Teflon sheets proved an ideal choice of lubricant choice. Future work should investigate the commercial lubricants and coating presented in this thesis using deep drawing experiments for which the extent of material sliding is much higher.

5.1.3 Temperature history validation

LDH specimens were instrumented with thermocouples by George *et al.* [130] to measure the temperature-time history during heat up and manual transfer of the specimens. Robotic transfer of instrumented specimens was not possible; therefore, instrumented specimens were transferred manually from the furnace to the tooling to measure convective cooling during transfer. Figure 60 shows the heat up time-temperature history of the LDH specimen. The furnace temperature was set to 480ºC. The heat-up time required to achieve a uniform temperature of 480ºC is about 12 min.

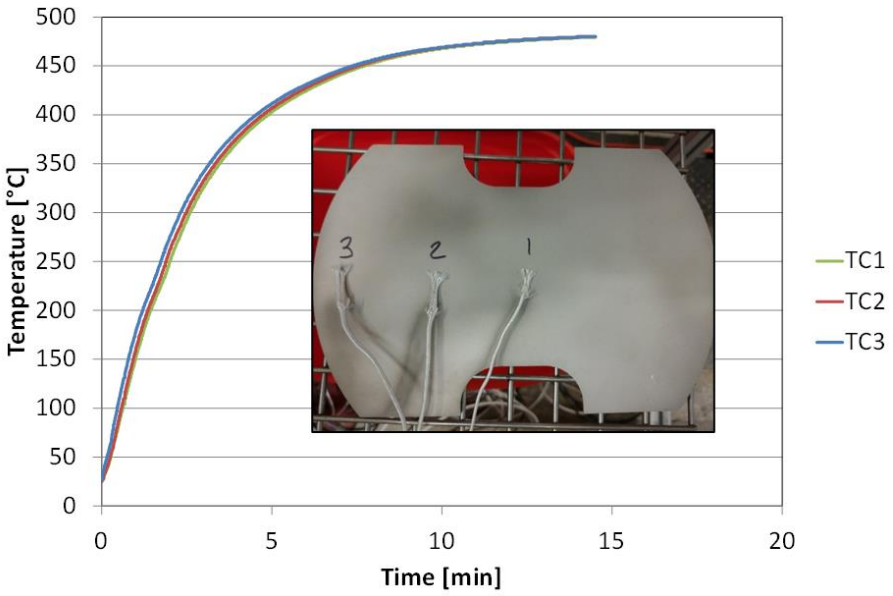

Figure 60: Time-temperature history of LDH specimen during heat up [130].

The temperature drop due to convective cooling during blank transfer from the furnace to the tooling can be seen in Figure 61. The rate of convective cooling of the blank (the slope of the first portion of the curve) while on the furnace rack is highlighted and is approximately 1.25 ºC/s. The second portion of the curve corresponds to the convective cooling rate of the blank during transfer which is about 3.1 ºC/s. These timings correspond to a manual transfer process. Given the robot transfer time of 5 seconds and the two cooling rates shown, the approximate temperature of the

blank at the beginning of forming is estimated to be 450 ºC. This value was used in the finite element simulations as the initial temperature at the beginning of the DQ forming operation, as described in Section 5.2.4.

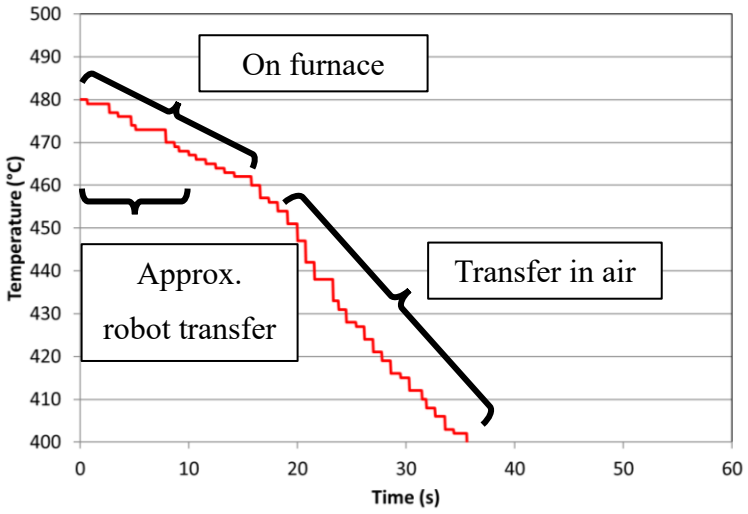

Figure 61: Robot convection cooling rate transfer [130].

5.1.4 Formability test procedure

The test procedure begins with robotic transfer of the cold blank into the Deltech furnace to be solutionized at 480ºC for 15 min. The hot blank is then transferred onto the spring-loaded lifters on the binder; the transfer is complete in 5 seconds. The die set and punch are water-cooled to 12ºC. Once the die is 25 mm from contacting the blank, the data acquisition system is initiated, and the die speed is reduced to 64 mm/s for the remainder of the forming stroke. Once the die contacts the blank, it is pressed against the binder, which provides a constant resistance to movement (356 kN) under closed-loop control. The die, blank and binder continue moving downwards and the blank is formed over the hemispherical punch, which is fixed in position. Once the forming operation is completed, the cushion actuator raises the binder to the starting position, which completes the cycle.

5.1.5 Formability Test Matrix

The test matrix for the formability experiments performed by George *et al.* [130] on AA7075 is presented in Table 13. The test highlighted in Table 13 includes a hot solutionized blank with chilled die (12°C) and punch and a fast-forming speed of 64 mm/s.

		DQ + chilled tooling + 64 mm/s
Geometry	**25.4 mm**	3
	76.2 mm	4
	152.4 mm	3
Total		10

Table 13: DQ Formability Test Matrix

5.2 Numerical Model of the DQ LDH Test

A numerical model of the die quenching (DQ) limiting dome height (LDH) experiments was developed using commercial FE explicit dynamic code LS-DYNA. This section documents the numerical model, which considered the two constitutive fits developed in Chapter 4. A comparison between the predictions and the measured data from George *et al.* [130] is given in Chapter 6 and is used to assess the two constitutive fits.

5.2.1 Discretization

The three different blank geometries were implemented; the mesh used to discretize the model with the 76.2 mm geometry is shown in Figure 62. The model comprises the blank, punch, binder, and die. The model is one-quarter of the total geometry; this reduction was possible due to the symmetry about the X and Z-axes, which reduced the computational time. Symmetry boundary conditions were enforced to maintain full geometry deformation behavior.

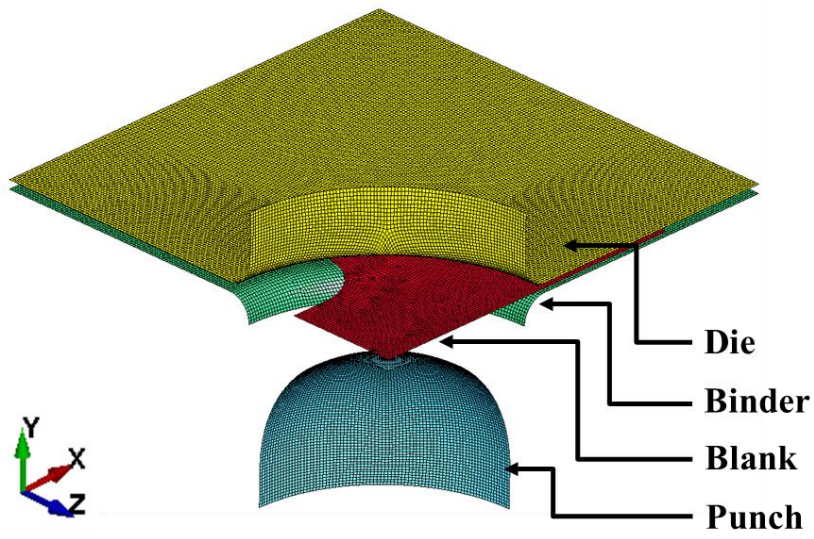

Figure 62: Quarter symmetry model tooling set-up

First-order quadrilateral shell elements were used to model the blank and tool surfaces. All blank geometries were discretized with an element size ranging from 1 to 3 mm, while the tooling element size ranges from 0.5 to 1 mm. To reduce computational time, selective mass scaling was introduced by prescribing a time step of 2×10^{-6} s as a lower bound of the explicit time step, this forces the solver to locally increase the density of the material accordingly to preserve the Courant criterion. Fully integrated Belytschko-Lin-Tsay shell elements based on the Reissner-Mindlin kinematic assumption [113] were used for the blank; this was done to eliminate hourglassing zero-energy modes. The blank elements had five through-thickness integration points, following standard Lobatto integration. Mass elements are added to the tooling nodes corresponding to the mass of the upper and lower die; this is used to compute the contact stiffness. All tooling elements were modeled as a rigid non-deformable material.

5.2.2 Material Model

The blank material used was a temperature and strain-rate-dependent tabulated Barlat YLD89 [120] plane stress model, which utilized the hardening curves derived from the modified Zerilli-Armstrong formulations mentioned previously. The Lankford coefficients used to describe the anisotropy of the material were obtained from Rahman *et al.* [132] and are shown in Table 14.

$\mathbf{r_0}$	$\mathbf{r_{45}}$	$\mathbf{r_{90}}$
0.78	0.95	1.34

Table 14: Lankford Coefficients for AA7075 [132]

The tabulated Barlat YLD89 constitutive model utilized a three-dimensional table containing temperatures, strain rates and their corresponding hardening curves. The FE software uses the input hardening curves to interpolate the flow stress as a function of temperature and strain rate conditions. This data will also be extrapolated if the conditions go out of the input range. A material

physics-based constitutive model, such as the Modified Zerilli-Armstrong model, described in Section 4.2 and Section 0, allows, to some degree, the computation of hardening curves for strain rate conditions that fall outside the experimental material characterization dataset. The DQ process is likely to have peak strain rates that fall outside the material characterization dataset, thus, the usage of the physics based Modified Zerilli-Armstrong constitutive model is aimed at reducing extrapolation errors associated with polynomial fits. A local coordinate system is used to define material direction, with X being parallel to the rolling direction, this information is utilized by the material card to describe material anisotropy.

5.2.3 Mechanical Boundary Conditions and Motion

The die and binder were constrained in all rotational degrees of freedom (DOF) and in the X and Z translational degrees of freedom (Figure 62. The punch was constrained in all rotational and translational DOF. The outer surfaces of the blank in the model are initially 0.05 mm above the binder and 0.05 mm below the top die, while the punch is fixed, initially 1.5 mm below the blank outer surface. The die was velocity controlled. A binder load of 89 kN was assigned to the quarter symmetry model, corresponding to 356 kN for the full-scale experiment; this force was applied in the positive Y direction. A rigid body stopper was applied to the binder, preventing any positive Y displacement and limiting its velocity to that of the die. At the start, the die ramps up to a velocity of 64 mm/s and contact is established between the die, blank and binder. Once the binder load is overcome, the die, blank and binder start moving down at the same velocity and the blank contacts the punch such that the dome is formed. The termination time for the model is 1 s or about 50 mm of stroke. A penalty function-based automatic one-way surface-to-surface contact algorithm is defined for the blank and tooling shell element contacts, with a COF of 0.04 [101, 130] for punch to blank contact and a COF of 0.65 [101, 130] for die and binder to blank contact.

5.2.4 Thermal Boundary Conditions

The model utilized a coupled thermomechanical solver and a Crank-Nicolson solution algorithm for the thermal time step, with a symmetric direct solver. The blank initial temperature was set to 450°C, which corresponds to the measured value prior to forming (Section 5.1.3). The nodes of the die and binder as well as the nodes of the punch are given a set temperature of 12°C, which is the temperature of the chilled water in the die and binder cooling channels. The heat transfer coefficients for conduction as a function of interfacial pressure, shown in Figure 63 corresponded to the measured data published by Omer *et al.* [30]. The maximum distance for thermal contact detection was set to 0.1 mm.

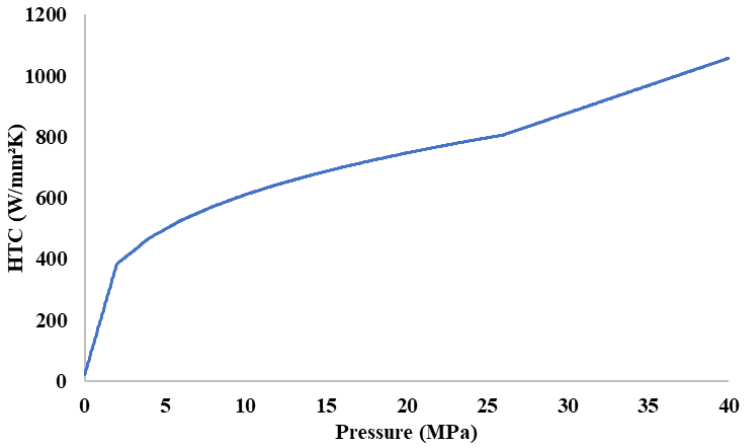

Figure 63: Conduction Heat Transfer Coefficient (HTC) vs. Interfacial Pressure [30]

Convection and radiation heat transfer were active during the entire forming operation. A convection heat transfer coefficient of 0.018 W/mm^{2}K was assigned to the blank; this resulted in a convective cooling rate similar to thermocouple measurements taken from the instrumented blanks shown in as seen in Figure 64.

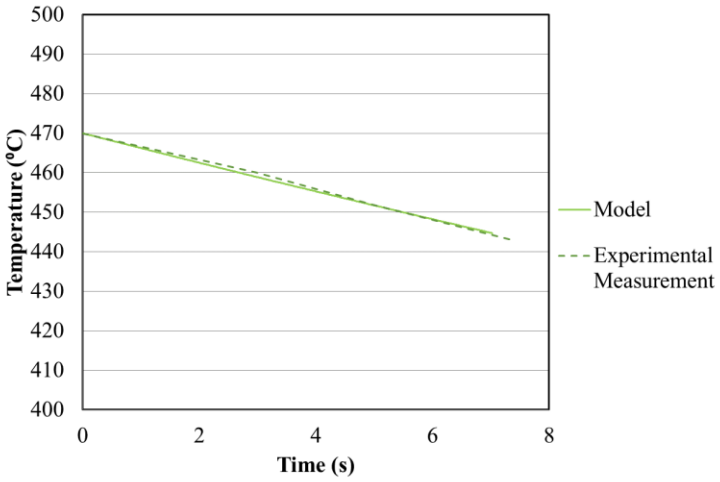

Figure 64: FE Predicted Convection Heat Transfer prior to forming vs. Experimental Measurement [130]

6 DQ LDH Numerical Modeling Results

The following chapter describes the results from the current finite element simulations of the AA7075 die quenching LDH experiments performed by George *et al.* [130]. Simulations were performed using the two constitutive fits, designated the Omer-fit and the Wang-fit, that were developed as part of this research (see Section 4.2 and 0 respectively). The accuracy of the two fits were assessed in terms of the resulting predictions of load-displacement response, strain paths and major strain distributions, which were compared to the experimental results. The models were also used to predict the temperature distributions and time histories during the forming operations.

6.1 Force *versus* Displacement Relation

The predicted and measured force *versus* displacement history for the DQ LDH experiments using the 25.4 mm, 76.2 mm and 152.4 mm wide samples are shown in Figure 65. Using the Omer-fit, the model exhibits a significantly higher hardening response for all test geometries when compared to the experimental measurements or the predictions using the Wang-fit. The Wang-fit, on the other hand, yields a hardening response which tracks the experimental results more closely. The force predictions made by the Omer-fit and Wang-fit for both the 25.4 mm (Figure 65a) and 76.2 mm (Figure 65b) geometries diverge, just past 20 mm of displacement. In the case of the 152.4 mm geometry (Figure 65c), divergence between the two models occurs from the start of the test. For the 25.4 mm and 76.2 mm wide test geometries, the Wang-fit tends to under predict force at larger punch displacement near the end of the test. For the 152.4 mm geometry the force is slightly over predicted using the Wang-fit for the entire displacement range, however, slight softening is exhibited at elevated displacement similar to the other test geometries. At lower displacement, the Wang-fit tends to slightly over predict the force when compared to the experimental results for all test geometries.

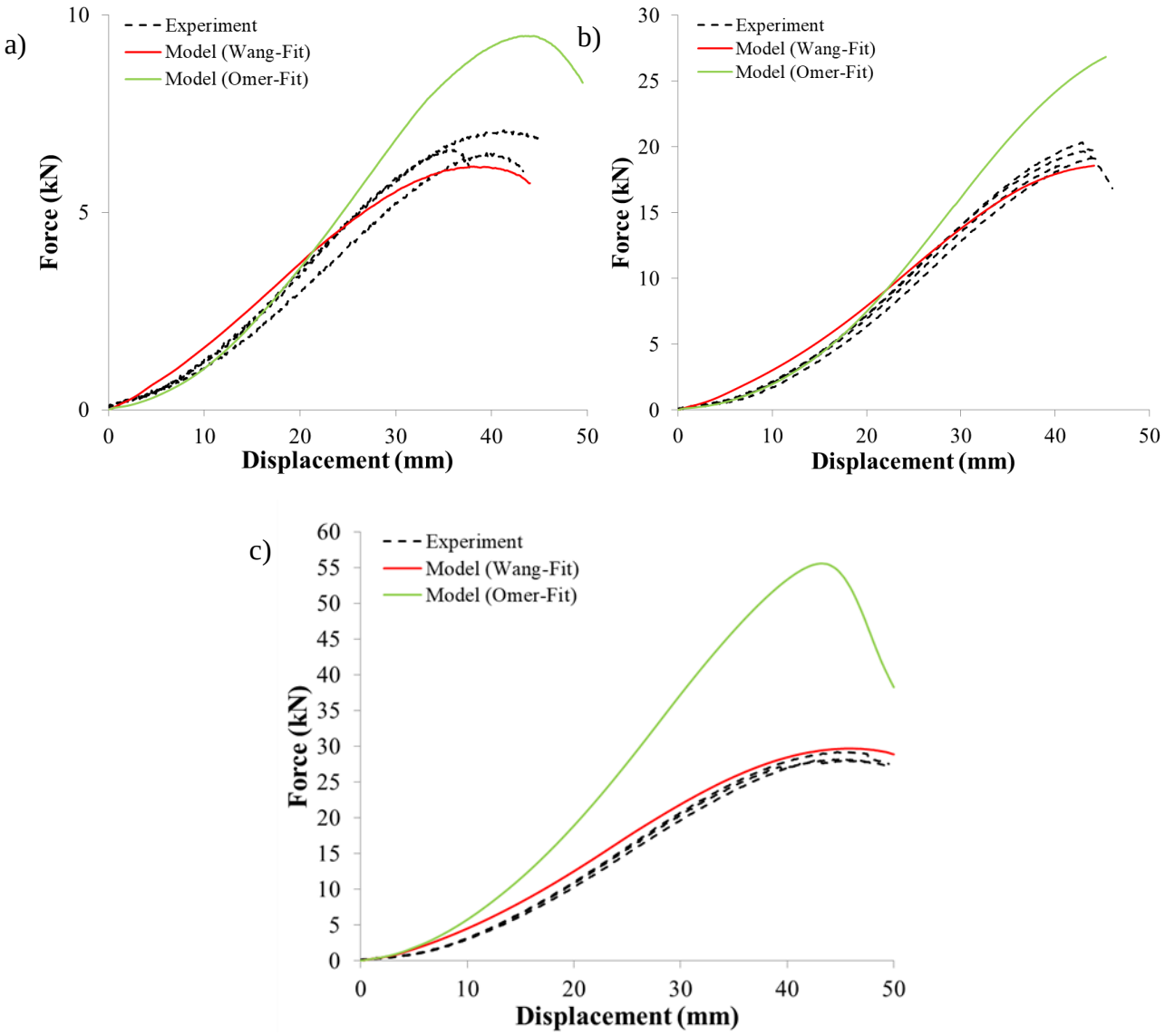

Figure 65: Predicted and measured load-displacement curves during DQ for the (a) 25.4 mm, (b) 76.2 mm and (c) 152.4 mm specimens.

Table 15 shows the average peak force and associated dome height for the experimental results, Omer-fit and Wang-fit models. The peak force and dome height percentage difference between the experimental results and each model (Omer-fit and Wang-fit) for all geometries are also shown.

The peak force for the 76.2 mm geometry for both models is reported at the same displacement as the experimental results (42.5 mm). The Wang-fit has overall lower percentage difference for both peak force and associated dome height, as compared to the Omer-fit.

Geometry	Measurement	Experiment	Omer-fit	Wang-fit
25.4 mm	Peak Force (kN)	6.8	9.5	6.2
	Percent Difference	--	34	8.7
	Dome Height at Peak Force (mm)	38.7	48.4	37.9
	Percent Difference	--	22.0	2.1
76.2 mm	Peak Force (kN)	18.8	25.6	18.4
	Percent Difference	--	30.5	2.2
	Dome Height at Peak Force (mm)	42.5	42.5	42.5
	Percent Difference	--	--	--
152.4 mm	Peak Force (kN)	28.6	55.5	29.6
	Percent Difference	--	94.2	3.5
	Dome Height at Peak Force (mm)	44.2	44.8	43.2
	Percent Difference	--	1.4	2.2

Table 15: Peak Force and Associated Dome Height - Experimental versus Numerical Results Summary

6.2 Predicted Thermal History and Distribution

The predicted thermal histories and temperature distributions for all three test geometries (25.4, 76.2 and 152.4 mm), presented in this section, provide insight into the experimental results. Since the thermal numerical formulation for the models using the Omer-fit and Wang-fit are identical, only one set of predictions are presented.

Figure 66a shows the thermal history for the 25.4 mm wide specimen at the dome tip. The associated temperature contour plot is shown in Figure 66b. The temperature at the dome tip decreases by 23ºC during the forming process from 450 to 427ºC. The transition region between the specimen gauge section and the grip section remains the hottest part of the specimen at the end of forming, largely since this region does not contact the tooling so experiences a lower cooling rate. The average temperature of the transition region at the end of forming is 443ºC, which is only 7ºC below the starting temperature. In the experiments, deformation within the specimens localized within this transition region, which is attributed to the temperature differential between the dome tip and the transition region. The higher temperatures give rise to a relatively softer hardening response at the transition region as compared to the dome tip, which shifts localization from the dome tip to the transition region.

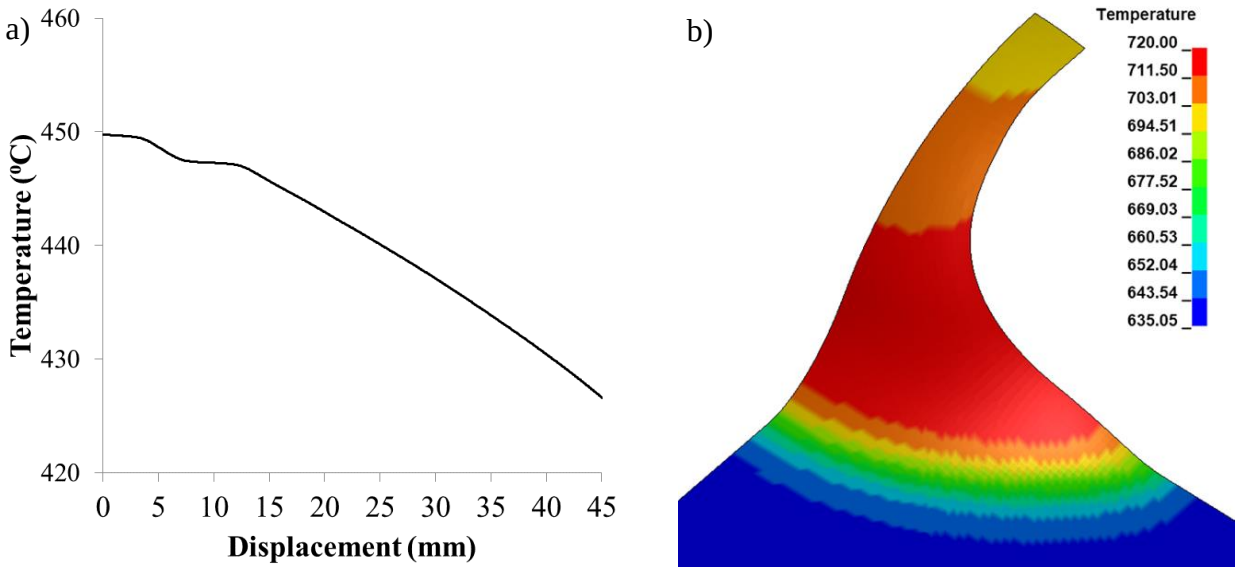

Figure 66: (a) Predicted temperature versus displacement history for 25.4 mm specimen numerical results and (b) predicted temperature distribution in °K for the 25.4 mm specimen at 40 mm displacement.

The thermal history of the 76.2 mm wide specimen at the dome tip is shown in Figure 67a. The associated temperature contour plot is shown in Figure 67b. The 76.2 mm wide specimen exhibits thermal distribution that is similar to that of the 25.4 mm geometry. The transition region is again the hottest part of the specimen with an average temperature of 446ºC. Furthermore, the dome tip exhibits a 27º C decrease in temperature by the end of forming. The hotter transition region and cooler dome tip can explain the onset of localization at the transition region, also seen in the experiments.

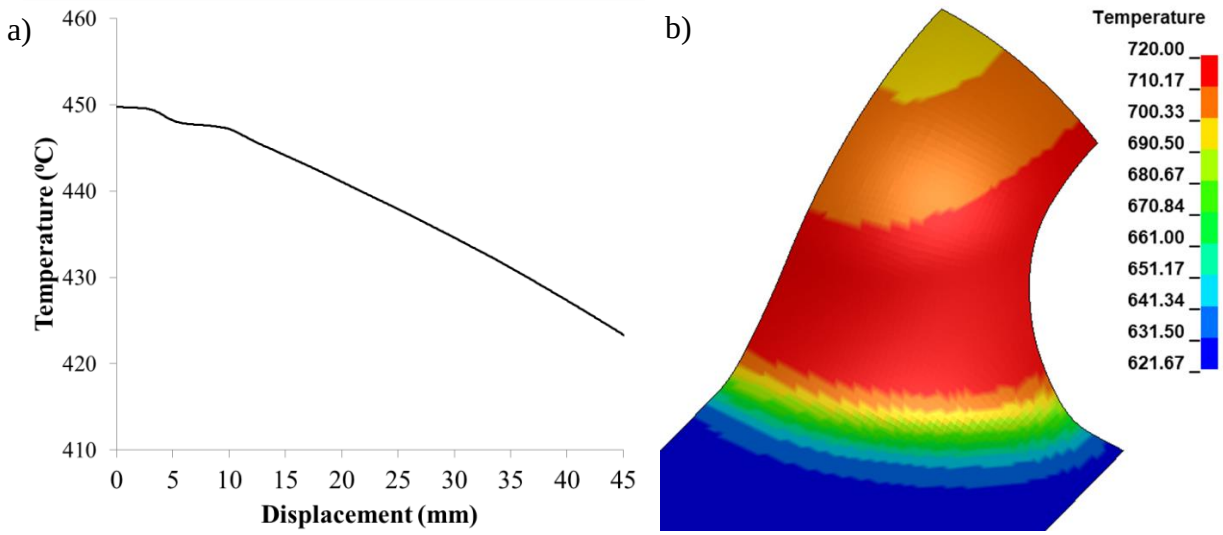

Figure 67: (a)Predicted temperature versus displacement history for 76.2 mm specimen and (b) predicted temperature distribution in °K for the 76.2 mm specimen) at 40 mm displacement.

The thermal history of the dome tip for the 152.4 mm geometry is shown in Figure 68a, while the temperature contour plot is shown in Figure 68b. The specimen experiences significant heat loss at the punch contact area during forming. The tip of the dome experiences a 40°C drop in temperature from 450ºC to 410ºC. For this geometry, the specimen failure occurred at the dome tip, likely due to fact that the unsupported region of the sample (between the punch and die) encompasses the full circumference of the punch. This lowers the stress in the unsupported region, forcing strain localization to the punch tip.

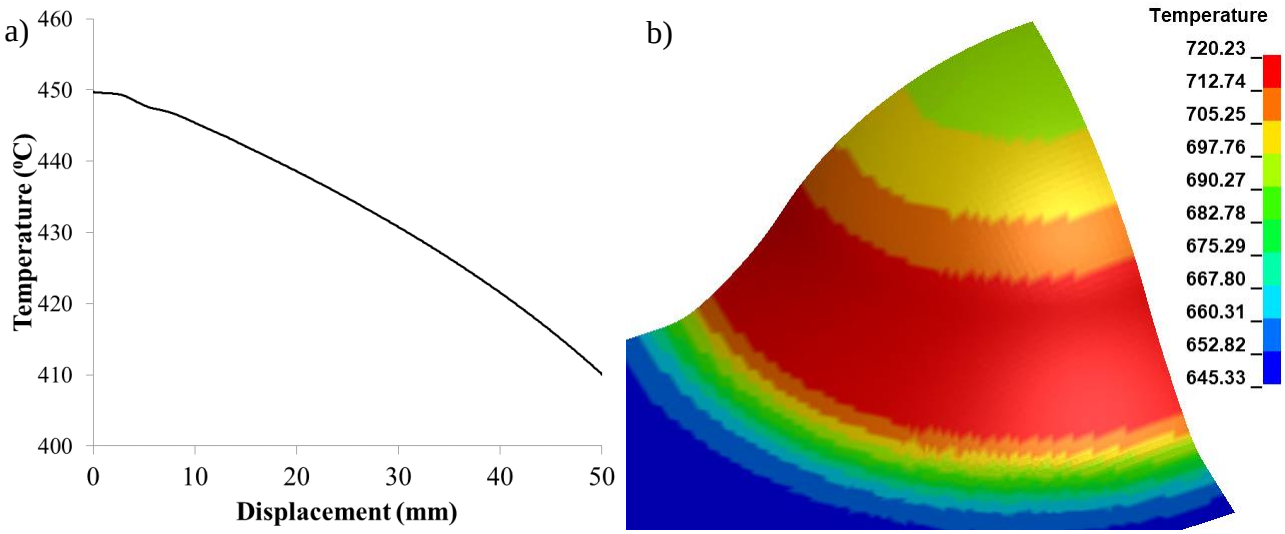

Figure 68: (a) Predicted temperature and major strain versus displacement history for 152.4 mm specimen and (b) predicted temperature distribution in °K for the 152.4 mm specimen at 40 mm displacement.

6.3 Strain History and Strain Distributions

Figure 69a shows the measured and predicted strain paths using the Omer- and Wang-fits for the 25.4 mm wide geometry. The strain path plot shows that the predictions using the Wang-fit fall on top of two of the experimental repeats while the Omer-fit model falls just to the right of those repeats. Both predicted strain paths lie close to the measured repeats with strain path curves furthest to the left on the major *versus* minor strain plot.

The predicted major strain at the dome tip *versus* dome height is plotted in Figure 69b. The predictions using the Wang-fit lie slightly below the predictions using the Omer-fit for the first 15 mm of the form. A lower major strain indicates a higher hardening response at lower strain, which is consistent with the same trend shown in the load-displacement plot shown in Figure 65a. Beyond 15 mm of displacement, the predicted strain of the Wang-fit increases at a much faster rate compared to the Omer-fit predictions, indicating a softer hardening response. This behaviour is also consistent with the trends in the load-displacement plot shown in Figure 65a. The major strain at the end of the form is 0.90 and 0.66 for the predictions using the Wang- and Omer-fits, respectively. Whereas the localization strain of the experimental repeat with the closest strain path to the FE models had a major strain of 0.97, as seen in Figure 69a.

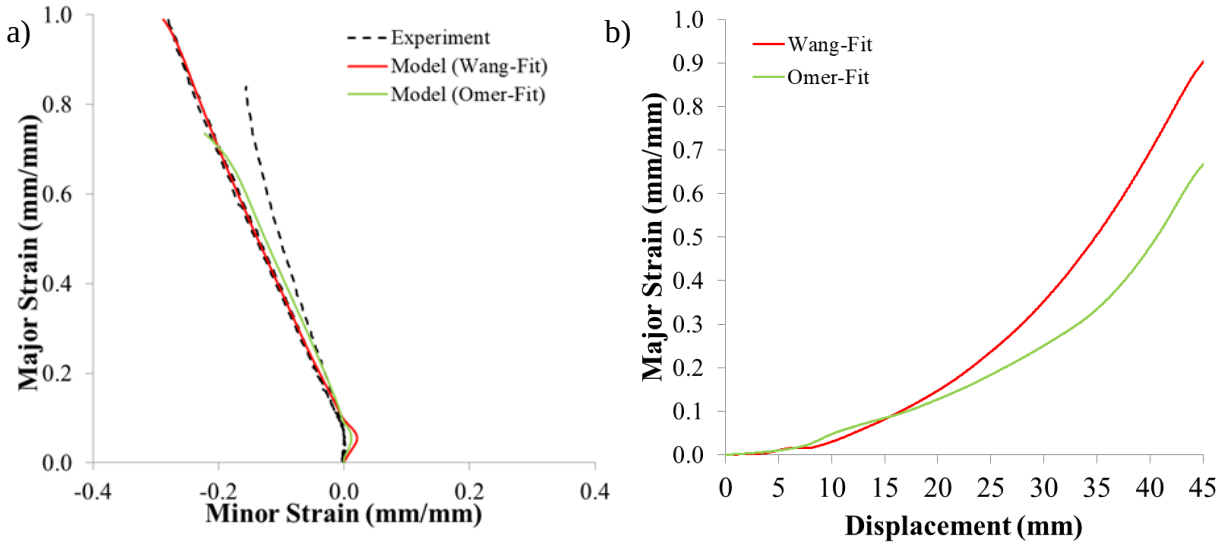

Figure 69: Predicted and measured strain path for (a) the 25.4 mm specimen and (b) predicted major strain versus displacement history for 25.4 mm specimen numerical

Figure 70a shows the measured major strain contours at approximately 40 mm dome height for the 25.4 mm specimen. All experimental repeats for this test condition localized at the die entry radius, as seen in Figure 70a. This figure also shows the line slice along which the experimental major strain measurements were taken. DIC measurements were utilized in the LDH experiments to obtain the strain profile perpendicular to the crack location on the specimen. Figure 70b shows the major strain profile of the 25.4 mm specimen perpendicular to the crack location at dome heights of 20, 30 and 40 mm. The predicted strain distributions using the Wang- and Omer-fit constitutive models are also plotted for the same dome heights and at an approximately similar location. The experimental repeat with the closest strain path to the numerical models is the one chosen for Figure 70b. In the experimental results, the 0 mm position corresponds to the centre of the punch. The dome heights for specific strain distributions were not directly measured by the DIC system; dome heights were rather calculated based on the nominal stroke rate and test time measurements. Experimental position measurements were taken from the deformed specimen prior to failure, which were used to map the major strain measurements in Figure 70b. Since, these measurements were taken from a deformed specimen, the line length will be different compared

to an undeformed specimen. Figure 70c presents the predicted contours of major strain using the Wang-fit at 40 mm dome height, while Figure 70d presents the corresponding predictions using the Omer-fit. The numerical models show the location of predicted localization to be closer to the center of the specimen. The Wang-fit over-predicts the strain profile for all three dome heights while the Omer-fit under-predicts the strain profile for all three dome heights. The Omer-fit strain profile lies significantly below the measured strains for dome heights of 30 and 40 mm, which reflects the higher hardening response. These significant differences between the measured and predicted strain profiles are attributed to the difference in the location where the specimen starts to localize.

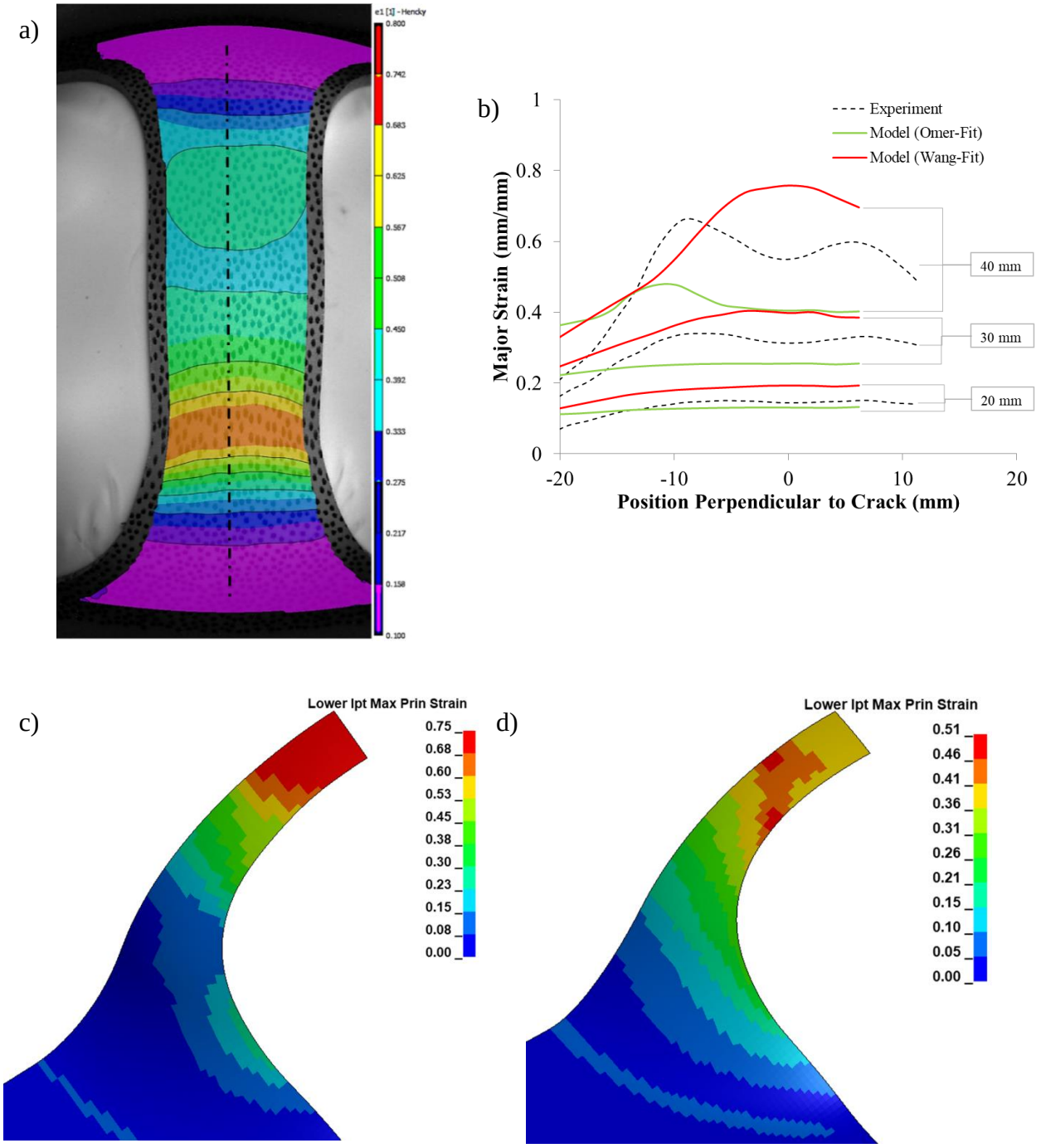

Figure 70: (a) Measured major strain contours at 40 mm dome height with dashed line indicating line along which strain distribution was extracted, (b) major strain along specimen length perpendicular to the crack for 25.4 mm specimen at 20, 30 and 40 mm dome height, (c) predicted major strain contour plot using Wang-fit at 40 mm dome height and (d) predicted major strain contour plot using Omer-fit at 40 mm dome height.

Figure 71a shows the measured and predicted strain paths using the Omer- and Wang-fits for the 76.2 mm wide geometry. The strain path plot shows that the predictions using the Wang-fit fall on

top of the rightmost experimental repeat while the model using the Omer-fit falls just to the right of that same repeat. This repeat has a $\varepsilon_2/\varepsilon_1$ ratio at failure of approximately -0.015 which corresponds to near-plane strain conditions.

In Figure 71b, the predicted major strain at the punch tip *versus* dome height using the Wang-fit is slightly below the predictions using the Omer-fit from 7 to 19 mm of the forming stroke. A lower major strain indicates a higher hardening response for the displacement range, which is consistent with the trend shown in the load-displacement plot shown in Figure 65b. The major strain at the end of forming is 0.50 and 0.34 for the predictions using the Wang- and Omer-fits, respectively, whereas the major strain at localization for the experimental repeat with the closest strain path to the FE models was 0.52, as seen in Figure 71a.

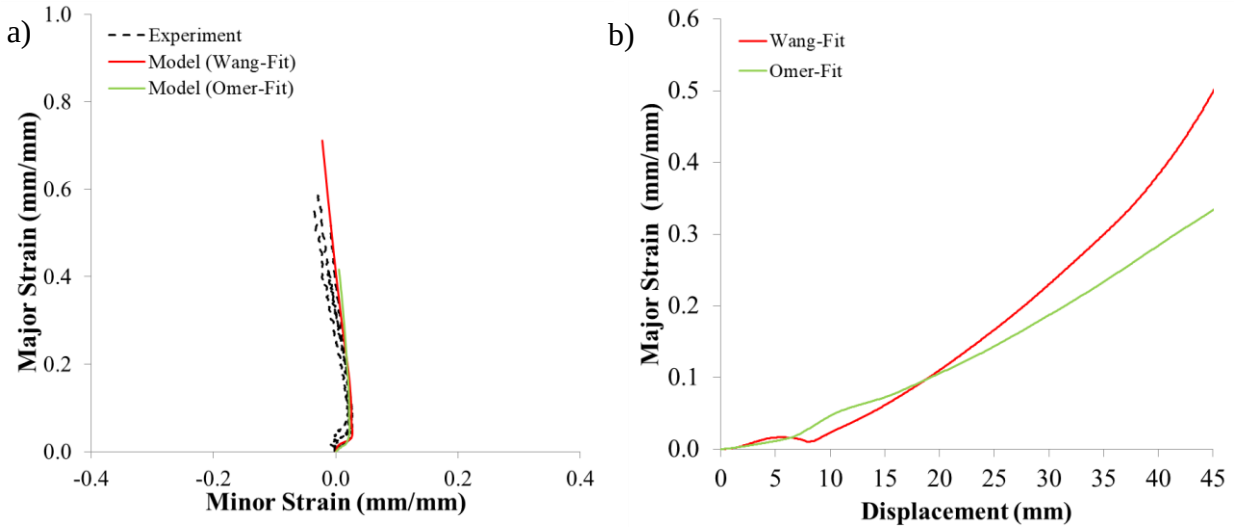

Figure 71: a) Predicted and measured strain path for the 76.2 mm specimen and (b) predicted major strain versus displacement history for the 76.2 mm specimen

Figure 72a shows the measured major strain contour at approximately 40 mm dome height for the 76.2 mm specimen. Figure 72b shows the predicted and measured major strain profiles perpendicular to the crack location at dome heights of 20, 30 and 40 mm. The experimental repeat with the closest strain path to the numerical models was considered for Figure 72b.

Figure 72c presents the predicted major strain contour using the Wang-fit at 40 mm dome height for the 76.2 mm geometry; likewise, Figure 72d presents the corresponding major strain contour using the Omer-fit. All experimental repeats for this test condition localized at the entry radius as seen in the DIC major strain contour at 40 mm dome height in Figure 72a. The numerical models show a location of predicted localization, which was also at the entry radius, with the Wang-fit also showing a milder localization at the dome center. The Wang-fit strain profiles for 20 mm dome height matches the experimental results closely, at 30 mm dome height it has a strain profile that increases linearly with position. At 40 mm, dome height the Wang-fit still has a strain profile which increases linearly with respect to position. It has lower stain than the experimental result from -19 to -4 mm; this region is where localization takes place in the experimental specimen. However, since the numerical model does not localize at the same location, the strain profile is linear and does not exhibit a peak between -19 and -4 mm. The Omer-fit has an overall significantly lower strain profile compared to the experimental result for all three dome heights at positions larger than -24 mm; this indicates an over-predicted hardening response. All Omer-fit strain profiles are very flat due to lack of localization along the line where the experimental strain measurements were extracted.

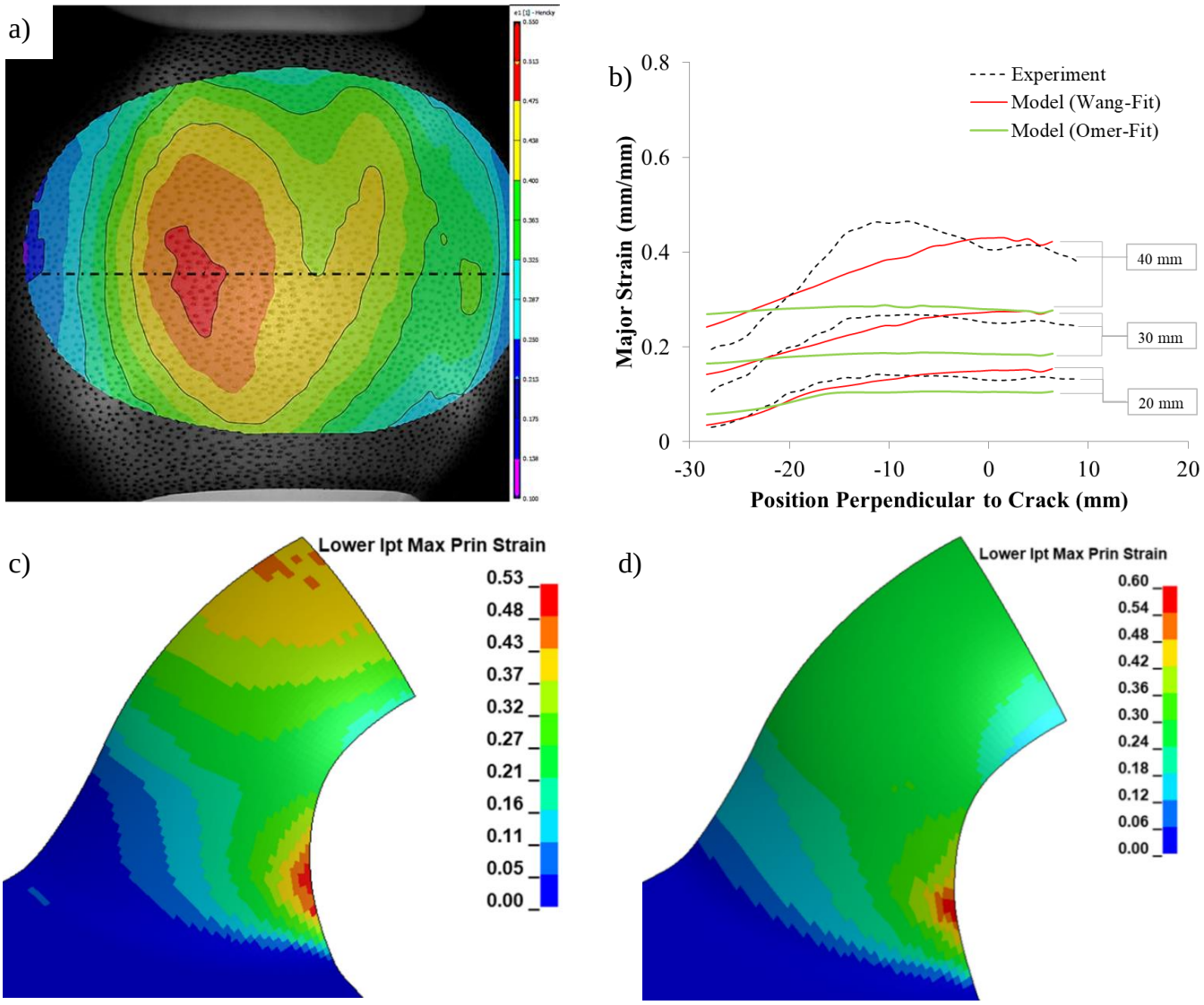

Figure 72: (a) Measured major strain contours at 40 mm dome height with dashed line indicating line along which the strain distribution was extracted, (b) major strain along specimen length perpendicular to the crack for 76.2 mm specimen at 20, 30 and 40 mm dome height, (c) predicted major strain contour plot using Wang-fit at 40 mm dome height and (d) predicted major strain contour plot using Omer-fit at 40 mm dome height.

Figure 73a shows the measured and predicted strain paths using the Omer- and Wang-fits for the 152.4 mm wide geometry. The strain path plot shows that the predictions using the Wang-fit model falls on top of the left most experimental repeat, while the Omer-fit model localizes near the unsupported region of the dome which results in stagnation of the deformation at the dome tip after this point.

The predicted major strain at the punch tip *versus* dome height (Figure 73b) using the Wang-fit is significantly above the predictions using the Omer-fit for most of the form. The major strain at the dome tip is 0.69 and 0.22 for the predictions using the Wang- and Omer-fits, respectively, at 50 mm dome height. The Wang-fit strain prediction compares well to the final strain in the experiments of 0.63 and 0.68 seen in Figure 73a for the two repeats closet to the model.

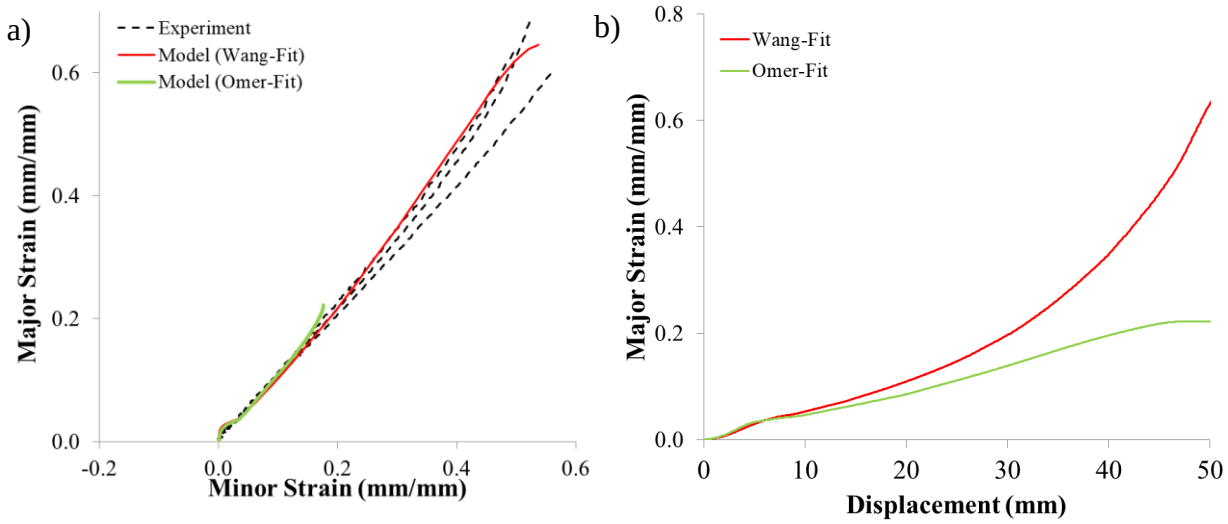

Figure 73: (a) Predicted and measured strain path for the 152.4 mm specimen and (b) predicted major strain versus displacement history for 152.4 mm specimen

Figure 74a shows the measured major strain contour for a dome height of approximately 40 mm. All experimental repeats for this test condition localized at the center of the dome. Figure 74b shows the major strain profile of the 152.4 mm specimen perpendicular to the crack location at dome heights of 20, 30 and 40 mm. The predicted curves are only for one-half of the geometry due to symmetry. Since this test specimen localized at the center, the rest of the strain profile would be on the other side of the symmetry plane. Figure 74c presents the predicted major strain contour using the Wang-fit at 40 mm dome height for the 152.4 mm geometry, while Figure 74d presents the corresponding Omer-fit predictions. At 20 mm, 30 mm and 40 mm dome height, the Wang-fit predictions accurately track the experimental results, while the Omer-fit exhibits significantly

lower strain at the center of the specimen near 0 mm. The Wang-fit correctly predicts localization at the centre of the specimen (Figure 74c), while the Omer-fit predicts a failure near the transition region in the TD. The difference in region of localization seen in the Omer-fit can explain the inaccuracies in strain profile and load-displacement (Figure 65c) predictions. The higher hardening exhibited in the Omer *et al.* [54] material characterization data causes the tip of the dome to harden significantly at lower temperature forcing the localization at the transition region, which increases the forming force.

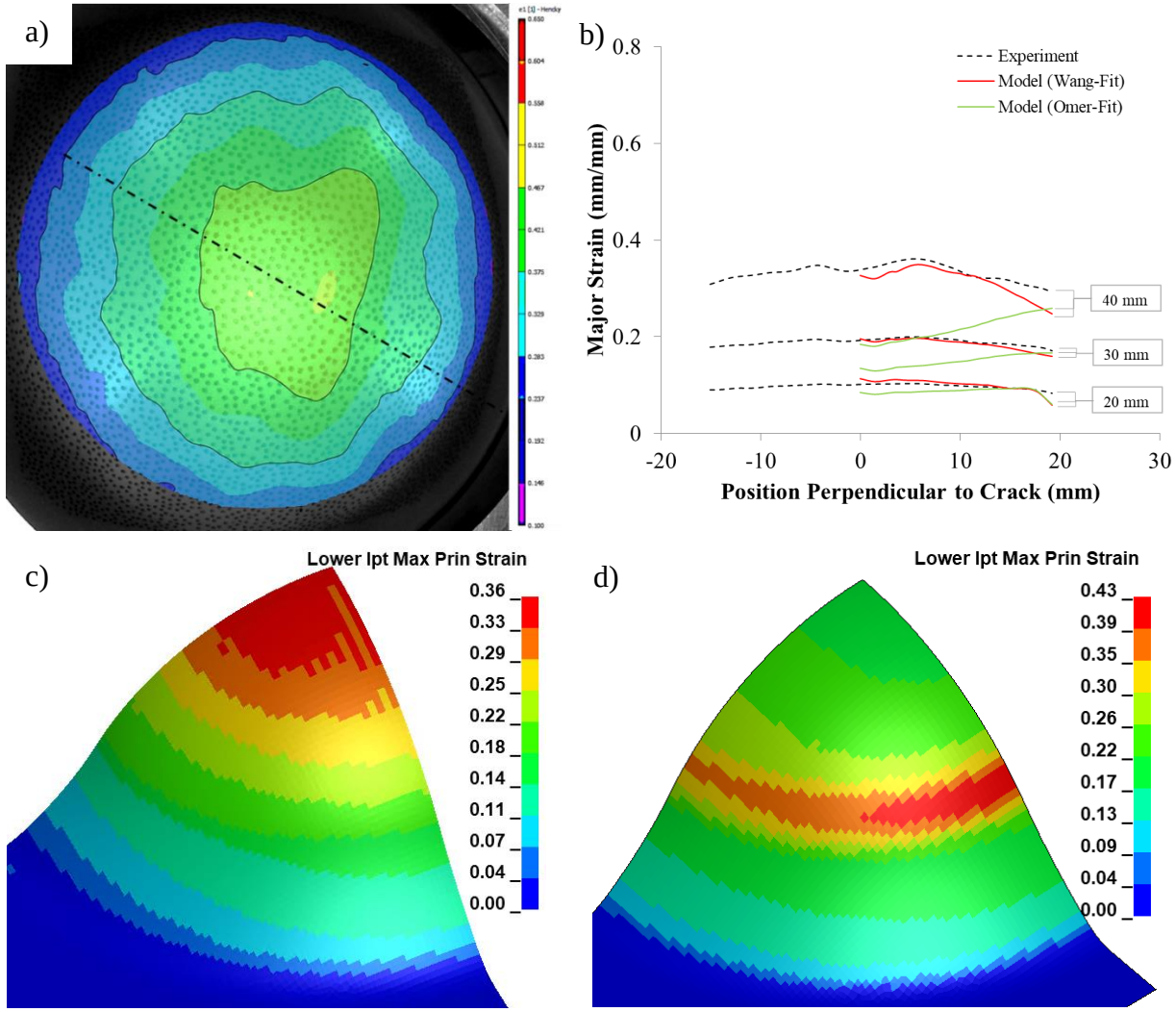

Figure 74: (a) Measured major strain contours at 40 mm dome height with dashed line indicating line along which strain distribution was extracted, (b) major strain along specimen length perpendicular to the crack for 152.4 mm specimen at 20, 30 and 40 mm dome height, (c) predicted major strain contour plot using Wang-fit at 40 mm dome height and (d) predicted major strain contour plot using Omer-fit at 40 mm dome height.

6.4 Numerical Modeling Summary

Numerical models of the LDH die quench experiments were developed utilizing the modified Zerilli-Armstrong constitutive model fit to the Omer *et al.* [54] and Wang *et al.* [119] material characterization datasets. The Omer-fit predicted a significantly higher forming force overall as compared to the measured data and the Wang-fit. The model utilizing the Wang-fit predicted the forming force *versus* displacement response more accurately for all three-test geometries (25.4 mm, 76.2 mm and 152.4 mm). However, the Wang-fit resulted in a slightly softer response at large dome heights near the end of the stroke for the 25.4 mm and the 76.2 mm specimen geometries, as compared to the experiments. The Wang-fit model shows comparable results for strain profiles at lower dome heights for all geometries, as compared to the experimental results, with the greatest accuracy in the case of the 152.4 mm wide specimen. The differences in strain profiles are primarily due to the difference in location of localization between the model and experiments for some cases. The Omer-fit had a significantly lower strain overall for all geometries as compared to the experimental result, which signifies a higher hardening response. The Wang-fit strain prediction is a little lower compared to the experimental result at elevated dome height. The high hardening response of the Omer-fit and the slightly softer response of the Wang-fit are a direct result of the methods used to measure the strain and calculate the stress in the original experiments. Since the Wang-fit is based on measurement that assumed a uniform strain throughout the gauge, this fit under-predicts the strain level, especially at high temperature and low strain rate for which necking is more pronounced. Since the strain in the Wang *et al.* [119] dataset may not capture localization within the gauge section, the stress, which is calculated using the strain, will also be low. On the other hand, the Omer-fit used DIC to accurately determine local strain. The stress is calculated by dividing the load cell force from the tensile test machine by the

true or local cross-sectional area through the novel ARM method. The combination of the load cell reading and ARM method resulted in an over-predicted stress response in the LDH model.

The temperature at the transition region between the punch surface and the die entry radius remained the hottest part within the test specimen geometry, which was the failure location for the 25.4 mm and 76.2 mm experimental LDH geometries. The numerical models of the 25.4 mm and 76.2 mm geometries predicted a center and an entry radius localization, respectively. The numerical model for the 152.4 mm geometry predicted a temperature drop of 40°C at the centre of the specimen; the Wang-fit numerical model predicted a center localization for this geometry.

7 Conclusions and Recommendations

7.1 Conclusions

This research has resulted in the development of a validated numerical model of die quench forming process for AA7075. This work has also comprised friction characterization of AA7075 under die quench process conditions. The numerical model will serve as a virtual test bench for process window control as well as prediction of load-displacement response and, when combined with forming limit data due to George *et al.* [130], formability of parts being forming under the die quench process.

From this research effort, the following conclusions can be drawn:

(1) The best performing lubricant, of those considered, was the Fuchs AL278 with an average COF of 0.05 for a tooling temperature of 200°C. The addition of the DLC coating was found to increase the COF for RT tooling from 0.048 to 0.059. With the addition of the DLC coating, the lubricant was more stable under a high tooling temperature of 200°C.

(2) The boron nitride showed good performance at 25°C tooling temperature for two out of three repeats, but with an elevated friction coefficient of 0.15. The Renoform 25, and Renoform 10 exhibited poor performance for RT and 200°C tooling temperature. Boron Nitride also exhibited poor performance for tooling temperatures of 200°C.

(3) A modified Zerilli-Armstrong constitutive equation was used to fit the Omer *et al.* [54] and Wang *et al.* [119] datasets, designated the Omer-fit and Wang-fit, respectively. Both fits exhibited R^2 values near unity for most test conditions. In terms of the conditions corresponding to the lowest quality fits, the Omer-fit had a minimum R^2 value of 0.7798 for the 470°C and 0.1 s^{-1} test condition, while the Wang-fit had a minimum R^2 value of 0.8992 for the 400°C and 0.1 s^{-1} test condition.

(4) The LDH model using the Omer-fit predicted a significantly higher forming force and significantly lower strain overall as compared to the experimental LDH test data and the model using the Wang-fit. The model using the Wang-fit predicted the force *versus* displacement relationship more accurately for all geometries, except at elevated dome heights where the response was slightly softer. The excessive hardening of the Omer-fit and the softer response of the Wang-fit are attributed to the methods used to measure the strain and calculate the stress in the material characterization datasets in the original experiments.

(5) The unsupported region between the punch tip and die entry radius (transition region) exhibited the highest temperatures for all specimen geometries. This hotter region will correspond to the lowest flow stress which accounts for the localization within this region observed by George *et al.* [130] for the 25.4 and 76.2 mm experimental LDH geometries. The Wang-fit numerical model correctly predicted a center failure location (strain localization) for the 152.4 mm geometry and an entry radius failure for the 76.2 mm geometry, whereas a center failure was predicted for the 25.4 mm geometry which was inconsistent with the experiments.

7.2 Recommendations

(1) Additional lubricant evaluation should be performed using the fast-forming set-up with die quench circular cup draw testing. These experiments would show the effect of each lubricant on specimen scoring and formability within the process temperature range.

(2) The contact pressure chosen for all Fuchs AL278 TCT tests (30 MPa) is on the order of the material tensile yield strength for the highest temperature conditions. In future work, the contact pressure should instead be set as a fixed percentage of the yield strength for each temperature condition. The TCT experiment utilizing the Fuchs AL278+DLC and 200°C tooling temperature should be re-evaluated due to oscillatory behavior exhibited due to tooling misalignment.

(3) Further investigation of the Omer *et al.* [54] material characterization dataset should be done by developing a tensile numerical model using solid elements with a fine mesh and the modified Zerilli-Armstrong constitutive fit to the Wang dataset [119]. A yield surface other than the 2-D Barlat YLD89 would have to be used for the numerical model. The true cross-sectional area of the specimen can be predicted using this model and the reaction force can be extracted, which in turn can be compared to the Omer *et al.* [54] true cross-sectional area calculations and force from load cell measurements. This can help to understand the differences between the Omer- and Wang-fits made apparent in the current research.

(4) Elevated temperature shear tests could be implemented as part of a new material characterization dataset to enhance the large-strain characterization of hardening behaviour, as an alternative to the ARM method.

(5) The numerical forming models shown in this manuscript used a temperature- and strain-rate-dependent Barlat YLD89 [120] yield surface which will lack some accuracy in predicting cup draw earing profile. YLD89 also lacks accuracy for stress states between biaxial and uniaxial. A temperature- and strain-rate-dependent Barlat YLD2000 yield surface is now available in LS-Dyna R12, which would offer more accurate anisotropy predictions.

(6) Artificial and natural ageing cycles should be explored experimentally to characterize and optimize post forming mechanical properties.

References

[1] E. Canada, "Greenhouse gas emissions performance for 2011 to 2015 light-duty vehicles - Canada.ca", Canada.ca, 2020. [Online]. Available: https://www.canada.ca/en/environment-climate-change/services/canadian-environmental-protection-act-registry/greenhouse-gas-emissions-performance-2011-2015.html.

[2] K.U. Kainer, “Potential von Magnesium in der Karosserie — Möglichkeiten und Entwicklungsbedarf,” in Stahl, Aluminium und Magnesium im Wettbewerb, EUROFORUM-Konferenz, 1998.

[3] O. El Fakir, L. Wang, D. Balint, J. Dear, J. Lin and T. Dean, "Numerical study of the solution heat treatment, forming, and in-die quenching (HFQ) process on AA5754", *International Journal of Machine Tools and Manufacture*, vol. 87, pp. 39-48, 2014.

[4] P. Rambabu, N. E. Prasad, K. V.V., and R. J. H. Wanhill, “Aluminum Alloys for Aerospace Applications,” in Aerospace Materials and Material Technologies, Springer Science+Business Media, 2017, pp. 29–52.

[5] S. Kurukuri, A. van den Boogaard, M. Ghosh and A. Miroux, "Thermo-mechanical Forming of Al-Mg-Si Alloys: Modeling and Experiments", *AIP Conference Proceedings*, vol. 1252, no. 1, 2010 [Online]. Available: https://aip.scitation.org/doi/abs/10.1063/1.3457638. [Accessed: 31- Dec- 2019]

[6] Mendiguren, E. de Argandona and L. Galdos, "Hot stamping of AA7075 aluminum sheets", *IOP Conference Series: Materials Science and Engineering*, vol. 159, p. 012026, 2016..

[7] W. Xiao, B. Wang, Y. Kang, W. Ma and X. Tang, "Deep drawing of aluminum alloy 7075 using hot stamping", *Rare Metals*, vol. 36, no. 6, pp. 485-493, 2017.

[8] G. Kridli, P. Friedman and J. Boileau, "Manufacturing processes for light alloys", Materials, Design and Manufacturing for Lightweight Vehicles, pp. 235-274, 2010.

[9] M. Mohamed, A. Foster, J. Lin, D. Balint and T. Dean, "Investigation of deformation and failure features in hot stamping of AA6082: Experimentation and modeling", *International Journal of Machine Tools and Manufacture*, vol. 53, no. 1, pp. 27-38, 2012.

[10] N. Abedrabbo, F. Pourboghrat and J. Carsley, "Forming of AA5182-O and AA5754-O at elevated temperatures using coupled thermo-mechanical finite element models", International Journal of Plasticity, vol. 23, no. 5, pp. 841-875, 2007.

[11] J. Mendiguren, R. Ortubay, E. de Argandoña and L. Galdos, "Experimental characterization of the heat transfer coefficient under different close loop controlled pressures and die temperatures", Applied Thermal Engineering, vol. 99, pp. 813-824, 2016.

[12] K. Mori *et al*., "Hot stamping of ultra-high strength steel parts", CIRP Annals, vol. 66, no. 2, pp. 755-777, 2017.

[13] H. Karbasian, "A review on hot stamping", Journal of Materials Processing Technology, vol. 210, no. 15, 2019.

[14] W. Xiao, B. Wang and K. Zheng, "An experimental and numerical investigation on the formability of AA7075 sheet in hot stamping condition", The International Journal of Advanced Manufacturing Technology, vol. 92, no. 9-12, pp. 3299-3309, 2017.

[15] N. Sotirov, P. Simon, C. Chimani, D. Uffelmann and C. Melzer, "Warm Deep Drawability of Peak-Aged 7075 Aluminium Sheet Alloy", Key Engineering Materials, vol. 504-506, pp. 955-960, 2012..

[16] M. Rokni, A. Zarei-Hanzaki, A. Roostaei and H. Abedi, "An investigation into the hot deformation characteristics of 7075 aluminum alloy", Materials & Design, vol. 32, no. 4, pp. 2339-2344, 2011.

[17] S. Esmaeili, D. Lloyd and W. Poole, "Modeling of precipitation hardening for the naturally aged Al-Mg-Si-Cu alloy AA6111", Acta Materialia, vol. 51, no. 12, pp. 3467-3481, 2003.

[18] J. Hatch, "METALLURGY OF HEAT TREATMENT AND GENERAL PRINCIPLES OF PRECIPITATION HARDENING", in Aluminum Properties and Physical Metallurgy, J. Hatch, Ed. ASTM International, 1984, pp. 134-199.

[19] P. PRANGNELL, "Precipitation Behaviors in MMCs", Comprehensive Composite Materials, pp. 61-90, 2000.

[20] L. Cheng, W. Poole, J. Embury and D. Lloyd, "The influence of precipitation on the work-hardening behavior of the aluminum alloys AA6111 and AA7030", Metallurgical and Materials Transactions A, vol. 34, no. 11, pp. 2473-2481, 2003.

[21] D. MacKenzie, "Heat Treatment Practice of Wrought Age-Hardenable Aluminum Alloys", ASTM Handbook, vol. 2, 2018.

[22] K. Anderson, J. Weritz, J. Kaufman and D. MacKenzie, Aluminum science and technology, Metallurgy of Heat Treatable Aluminum Alloys. ASTM, pp. 411-438.

[23] "Heat Treating of Aluminum Alloys", in Heat Treating Volume 4, ASTM International, 1991, pp. 841-879.

[24] B. Shang, Z. Yin, G. Wang, B. Liu and Z. Huang, "Investigation of quench sensitivity and transformation kinetics during isothermal treatment in 6082 aluminum alloy", Materials & Design, vol. 32, no. 7, pp. 3818-3822, 2011.

[25] A. Miodownik, N. Saunders, J. Schille and Z. Guo, "Metastable Phase Formation in Multi-Component Aluminium Alloys", Defect and Diffusion Forum, vol. 263, pp. 31-40, 2007.

[26] J. Ferguson, B. Schultz, J. Mantas, H. Shokouhi and P. Rohatgi, "Effect of Cu, Zn, and Mg Concentration on Heat Treating Behavior of Squeeze Cast Al-(10 to 12)Zn-(3.0 to 3.4)Mg-(0.8 to 1)Cu", Metals, vol. 4, no. 3, pp. 314-321, 2014. Available: 10.3390/met4030314.

[27] A. Leacock, C. Howe, D. Brown, O. Lademo and A. Deering, "Evolution of mechanical properties in a 7075 Al-alloy subject to natural ageing", Materials & Design, vol. 49, pp. 160-167, 2013.

[28] S. Liu, Q. Zhong, Y. Zhang, W. Liu, X. Zhang and Y. Deng, "Investigation of quench sensitivity of high strength Al–Zn–Mg–Cu alloys by time–temperature-properties diagrams", Materials & Design, vol. 31, no. 6, pp. 3116-3120, 2010.

[29] Y. Lee, D. Koh, H. Kim and Y. Ahn, "Improved bake-hardening response of Al-Zn-Mg-Cu alloy through pre-aging treatment", Scripta Materialia, vol. 147, pp. 45-49, 2018.

[30] K. Omer, A. Abolhasani, S. Kim, T. Nikdejad, C. Butcher, M. Wells, S. Esmaeili and M. Worswick, "Process parameters for hot stamping of AA7075 and D-7xxx to achieve high performance aged products", Journal of Materials Processing Technology, vol. 257, pp. 170-179, 2018.

[31] R. Boulis, S. DiCecco and M. Worswick, "Die Quench Process Sensitivity of AA7050", IOP Conference Series: Materials Science and Engineering, vol. 651, p. 012106, 2019.

[32] S. Liu, Q. Zhong, Y. Zhang, W. Liu, X. Zhang and Y. Deng, "Investigation of quench sensitivity of high strength Al–Zn–Mg–Cu alloys by time–temperature-properties diagrams", Materials & Design, vol. 31, no. 6, pp. 3116-3120, 2010. Available: 10.1016/j.matdes.2009.12.038.

[33] A. Deschamps and Y. Bréchet, "Influence of quench and heating rates on the ageing response of an Al–Zn–Mg–(Zr) alloy", Materials Science and Engineering: A, vol. 251, no. 1-2, pp. 200-207, 1998. Available: 10.1016/s0921-5093(98)00615-7.

[34] S. Liu, X. Zhang, M. Chen and J. You, "Influence ofageingon quench sensitivity effect of 7055 aluminum alloy", Materials Characterization, vol. 59, no. 1, pp. 53-60, 2008.

[35] P. LI *et al.*, "Quench sensitivity and microstructure character of high strength AA7050", Transactions of Nonferrous Metals Society of China, vol. 22, no. 2, pp. 268-274, 2012. Available: 10.1016/s1003-6326(11)61170-9.

[36] Y. Zhang, D. Pelliccia, B. Milkereit, N. Kirby, M. Starink and P. Rometsch, "Analysis of age hardening precipitates of Al-Zn-Mg-Cu alloys in a wide range of quenching rates using small angle X-ray scattering", Materials & Design, vol. 142, pp. 259-267, 2018. Available: 10.1016/j.matdes.2018.01.037.

[37] J. Buha, R. Lumley and A. Crosky, "Secondary ageing in an aluminium alloy 7050", Materials Science and Engineering: A, vol. 492, no. 1-2, pp. 1-10, 2008.

[38] Z. Katz and N. Ryum, "Precipitation kinetics in Al-alloys", Scripta Metallurgica, vol. 15, no. 3, pp. 265-268, 1981.

[39] K. Dehghani, A. Nekahi and M. Mirzaie, "Optimizing the bake hardening behavior of Al7075 using response surface methodology", Materials & Design, vol. 31, no. 4, pp. 1768-1775, 2010.

[40] N. Harrison and S. Luckey, "Hot Stamping of a B-Pillar Outer from High Strength Aluminum Sheet AA7075", SAE International Journal of Materials and Manufacturing, vol. 7, no. 3, pp. 567-573, 2014.

[41] F. Andreatta, H. Terryn and J. de Wit, "Corrosion behaviour of different tempers of AA7075 aluminium alloy", Electrochimica Acta, vol. 49, no. 17-18, pp. 2851-2862, 2004.

[42] B. Jegdić, B. Bobić, B. Gligorijević and V. Mišković-Stanković, "Corrosion properties of an aluminium alloy 7000 series after a new two step precipitation hardening", Zastita materijala, vol. 55, no. 4, pp. 387-394, 2014. Available: 10.5937/zasmat1404387j.

[43] M. Bobby Kannan, P. Bala Srinivasan and V. Raja, "Stress corrosion cracking (SCC) of aluminium alloys", Stress Corrosion Cracking, pp. 307-340, 2011.

[44] C. Bonnet, F. Valiorgue, J. Rech, C. Claudin, H. Hamdi, J. Bergheau and P. Gilles, "Identification of a friction model—Application to the context of dry cutting of an AISI 316L austenitic stainless steel with a TiN coated carbide tool", International Journal of Machine Tools and Manufacture, vol. 48, no. 11, pp. 1211-1223, 2008.

[45] Z. Yang, Y. Sun, X. Li, S. Wang and T. Mao, "Dry sliding wear performance of 7075 Al alloy under different temperatures and load conditions", Rare Metals, 2015.

[46] M. Kumar and N. Ross, "Investigations on the Hot Stamping of AW-7921-T4 Alloy Sheet", Advances in Materials Science and Engineering, vol. 2017, pp. 1-10, 2017.

[47] J. Zhang, Y. Deng and X. Zhang, "Constitutive modeling for creep age forming of heat-treatable strengthening aluminum alloys containing plate or rod shaped precipitates", Materials Science and Engineering: A, vol. 563, pp. 8-15, 2013.

[48] W. MA, B. WANG, L. FU, J. ZHOU and M. HUANG, "Effect of friction coefficient in deep drawing of AA6111 sheet at elevated temperatures", Transactions of Nonferrous Metals Society of China, vol. 25, no. 7, pp. 2342-2351, 2015.

[49] J. Béland and G. D'Amours, "Hot Forming of 7075 Aluminium Alloy Tubes to Produce Complex and Strong Components", SAE Technical Paper Series, 2012.

[50] J. Werenskiold, A. Deschamps and Y. Bréchet, "Characterization and modeling of precipitation kinetics in an Al–Zn–Mg alloy", Materials Science and Engineering: A, vol. 293, no. 1-2, pp. 267-274, 2000.

[51] L. Doan, Y. Ohmori and K. Nakai, "Precipitation and Dissolution Reactions in a 6061 Aluminum Alloy", Materials Transactions, JIM, vol. 41, no. 2, pp. 300-305, 2000. Available: 10.2320/matertrans1989.41.300.

[52] A. van den Boogaard, P. Bolt and R. Werkhoven, "Modeling of AlMg Sheet Forming at Elevated Temperatures", International Journal of Forming Processes, vol. 4, no. 3-4, pp. 361-375, 2001.

[53] P. Bolt, R. Werkhoven and T. Van den Boogaard, "Effect of elevated temperatures on the drawability of aluminium sheet components", 2001 [Online]. Available: https://www.researchgate.net/publication/254858786. [Accessed: 31- Dec- 2019]

[54] K. Omer, C. Butcher and M. Worswick, "Characterization and application of a constitutive model for two 7000-series aluminum alloys subjected to hot forming", International Journal of Mechanical Sciences, vol. 165, p. 105218, 2019.

[55] Y. Liu, Z. Zhu, Z. Wang, B. Zhu, Y. Wang and Y. Zhang, "Flow and friction behaviors of 6061 aluminum alloy at elevated temperatures and hot stamping of a B-pillar", The International Journal of Advanced Manufacturing Technology, vol. 96, no. 9-12, pp. 4063-4083, 2018

[56] T. Rahmaan, A. Abedini, C. Butcher, N. Pathak and M. Worswick, "Investigation into the shear stress, localization and fracture behaviour of DP600 and AA5182-O sheet metal alloys under elevated strain rates", International Journal of Impact Engineering, vol. 108, pp. 303-321, 2017.

[57] J. Peirs, P. Verleysen and J. Degrieck, "Novel Technique for Static and Dynamic Shear Testing of Ti6Al4V Sheet", Experimental Mechanics, vol. 52, no. 7, pp. 729-741, 2011.

[58] J. Peirs, P. Verleysen, W. Tirry, L. Rabet, D. Schryvers and J. Degrieck, "Dynamic shear localization in Ti6Al4V", Procedia Engineering, vol. 10, pp. 2342-2347, 2011.

[59] J. Peirs, P. Verleysen, W. Van Paepegem and J. Degrieck, "Determining the stress–strain behaviour at large strains from high strain rate tensile and shear experiments", International Journal of Impact Engineering, vol. 38, no. 5, pp. 406-415, 2011.

[60] A. Fallahiarezoodar and P. Taylan Altan, "R&D Update: Lightweighting in the automotive industry using sheet metal forming, Part 1", Thefabricator.com, 2019. [Online]. Available: https://www.thefabricator.com/stampingjournal/article/stamping/r-d-update-lightweighting-in-the-automotive-industry-using-sheet-metal-forming-part-1. [Accessed: 30- Dec- 2019]

[61] S. Keeler, Plastic instability and fracture in sheets stretched over rigid punches.

[62] Z. Marciniak and K. Kuczyński, "Limit strains in the processes of stretch-forming sheet metal", International Journal of Mechanical Sciences, vol. 9, no. 9, pp. 609-620, 1967.

[63] J. Danckert and T. Wanheim, "The use of a square grid as an alternative to a circular grid in the determination of strains", Journal of Mechanical Working Technology, vol. 3, no. 1, pp. 5-15, 1979.

[64] Ozturk, F. *et al*., "Grid Marking and Measurement Methods for Sheet Metal Formability", International Conference and Exhibition on Design and Production of Machines and Dies/Molds, vol.5, 2009.

[65] M. Sutton, "Image Correlation for Shape, Motion and Deformation Measurements: Basic Concepts, Theory and Applications". 2010.

[66] W. Volk and P. Hora, "New algorithm for a robust user-independent evaluation of beginning instability for the experimental FLC determination", International Journal of Material Forming, vol. 4, no. 3, pp. 339-346, 2010.

[67] K. Wang, J. Carsley, B. He, J. Li and L. Zhang, "Measuring forming limit strains with digital image correlation analysis", Journal of Materials Processing Technology, vol. 214, no. 5, pp. 1120-1130, 2014.

[68] H. Swift, "Plastic instability under plane stress", Journal of the Mechanics and Physics of Solids, vol. 1, no. 1, pp. 1-18, 1952.

[69] P. Hora, L. Tong and B. Berisha, "Modified maximum force criterion, a model for the theoretical prediction of forming limit curves", International Journal of Material Forming, vol. 6, no. 2, pp. 267-279, 2011.

[70] P. Hora, L. Tong and J. Reissner, "A Prediction Method for Ductile Sheet Metal Failure in FE-Simulation", Numisheet, 1996 [Online]. Available: https://www.researchgate.net/publication/273318278. [Accessed: 31- Dec- 2019]

[71] A. Martínez-Donaire, F. García-Lomas and C. Vallellano, "New approaches to detect the onset of localised necking in sheets under through-thickness strain gradients", Materials & Design, vol. 57, pp. 135-145, 2014.

[72] J. Min, T. Stoughton, J. Carsley and J. Lin, "Compensation for process-dependent effects in the determination of localized necking limits", International Journal of Mechanical Sciences, vol. 117, pp. 115-134, 2016.

[73] A. van den Boogaard, P. Bolt and R. Werkhoven, "Modeling of AlMg Sheet Forming at Elevated Temperatures", International Journal of Forming Processes, vol. 4, no. 3-4, pp. 361-375, 2001. Available: 10.3166/ijfp.4.361-375.

[74] S. Toros, F. Ozturk and I. Kacar, "Review of warm forming of aluminum–magnesium alloys", Journal of Materials Processing Technology, vol. 207, no. 1-3, pp. 1-12, 2008. Available: 10.1016/j.jmatprotec.2008.03.057.

[75] K. Holmberg and A. Erdemir, "Influence of tribology on global energy consumption, costs and emissions", Friction, vol. 5, no. 3, pp. 263-284, 2017.

[76] H. Kim, “Prediction and elimination of galling in forming galvanized advanced high strength steels (AHSS),” The Ohio State University, 2008

[77] W. D. WILSON, "FRICTION AND LUBRICATION IN SHEET METAL FORMING", Mechanics of Sheet Metal Forming, pp. 157-177, 1978. [Accessed 14 January 2020].

[78] D. Dowson, History of tribology. London: Professional Engineering Publishing, 1998.

[79] G. Li, X. Long, P. Yang and Z. Liang, "Advance on friction of stamping forming", The International Journal of Advanced Manufacturing Technology, vol. 96, no. 1-4, pp. 21-38, 2018.

[80] G. Amontons, "De la resistance causée dans desmachines, tant par les frottements des parties que les composent, que par la roideur des cordes qu’on y'employe, et la maniere de calculer l’un et l’autre", Paris, 1699.

[81] C. Coulomb, "Théorie des machines simples, en ayant égard au frottement de leurs parties età roideur des cordages", Paris, 1821.

[82] J. Desaguliers, "A Course of Experimental Philosophy", London, 1763.

[83] F. Bowden, D. Tabor and F. Palmer, "The Friction and Lubrication of Solids", American Journal of Physics, vol. 19, no. 7, pp. 428-429, 1951.

[84] "Asperities", Nano-world2.cs.unibas.ch, 2019. [Online]. Available: http://nano-world2.cs.unibas.ch/frictionmodule/content/0200makroreibung/0500asperities/?lang=en. [Accessed: 30- Dec- 2019]

[85] N. Suh, "Update on the delamination theory of wear in fundamentals of friction and wear of materials", American Society for Metals, 1981.

[86] K. Hyunok, "Friction and Lubrication", in Sheet Metal Forming Fundamentals, T. Altan and A. Tekkaya, Ed. ASM International, 2020, pp. 89-98 [Online]. Available: https://www.asminternational.org/documents/10192/1849770/05340G_Sample.pdf. [Accessed: 01- Jan- 2020]

[87] W. Wilson, "Friction Models for Metal Forming in the Boundary Lubrication Regime", Journal of Engineering Materials and Technology, vol. 113, no. 1, pp. 60-68, 1991.

[88] J. Schey and M. Shaw, "Tribology in Metalworking: Friction, Lubrication and Wear", Journal of Tribology, vol. 106, no. 1, pp. 174-174, 1984.

[89] "FORGE EASE AL 278 | Special applications | FUCHS LUBRICANTS CO. (United States)", Fuchs.com, 2019. [Online]. Available: https://www.fuchs.com/us/en/special/product/product/132830-forge-ease-al-278/. [Accessed: 30- Dec- 2019]

[90] "RENOFORM 10 ALWF | Special applications | FUCHS LUBRICANTS CO. (United States)", Fuchs.com, 2019. [Online]. Available: https://www.fuchs.com/us/en/special/product/product/132831-renoform-10-alwf/. [Accessed: 30- Dec- 2019]

[91] K. Dohda, C. Boher, F. Rezai-Aria and N. Mahayotsanun, "Tribology in metal forming at elevated temperatures", Friction, vol. 3, no. 1, pp. 1-27, 2015.

[92] J. Eriksson and M. Olsson, "Tribological testing of commercial CrN, (Ti,Al)N and CrC/C PVD coatings — Evaluation of galling and wear characteristics against different high strength steels", Surface and Coatings Technology, vol. 205, no. 16, pp. 4045-4051, 2011.

[93] W. Wang, X. Zheng, M. Hua and X. Wei, "Influence of surface modification on galling resistance of DC53 tool steel against galvanized advanced high strength steel sheet", Wear, vol. 360-361, pp. 1-13, 2016.

[94] "TD Coatings | TRD Coatings | Thermoreactive Diffusion Coatings | Thermal Diffusion Coatings | TRD Coatings | Thermo-Reactive Diffusion | TDkote Tri Cp", Richterprecision.com, 2019. [Online]. Available: http://www.richterprecision.com/services/td-trd-coatings/. [Accessed: 30- Dec- 2019]

[95] A. Riahi and A. Alpas, "Adhesion of AA5182 aluminum sheet to DLC and TiN coatings at 25 °C and 420 °C", Surface and Coatings Technology, vol. 202, no. 4-7, pp. 1055-1061, 2007.

[96] B. Podgornik, S. Hogmark and J. Pezdirnik, "Comparison between different test methods for evaluation of galling properties of surface engineered tool surfaces", Wear, vol. 257, no. 7-8, pp. 843-851, 2004.

[97] "TriboForm - Novel-T", Novel-T, 2019. [Online]. Available: https://novelt.com/en/success-stories/triboform/. [Accessed: 30- Dec- 2019]

[98] N. Bay, D. Olsson and J. Andreasen, "Lubricant test methods for sheet metal forming", Tribology International, vol. 41, no. 9-10, pp. 844-853, 2008.

[99] C. Vergne, C. Boher, C. Levaillant and R. Gras, "Analysis of the friction and wear behavior of hot work tool scale: application to the hot rolling process", Wear, vol. 250, no. 1-12, pp. 322-333, 2001.

[100] A. Yanagida, T. Kurihara and A. Azushima, "Development of tribo-simulator for hot stamping", Journal of Materials Processing Technology, vol. 210, no. 3, pp. 456-460, 2010.

[101] J. Noder, R. George, C. Butcher, M.J. Worswick, Friction characterization and application to warm forming of a high strength 7000-series aluminum sheet, Journal of Materials Processing Technology, Volume 293, 2021, 117066.

[102] P. Saha and W. Wilson, "Influence of plastic strain on friction in sheet metal forming", Wear, vol. 172, no. 2, pp. 167-173, 1994.

[103] E. Heide, Lubricant failure in sheet metal forming processes. [S.l.: s.n.], 2002.

[104] J. Andreasen, N. Bay and L. De Chiffre, "Quantification of galling in sheet metal forming by surface topography characterisation", International Journal of Machine Tools and Manufacture, vol. 38, no. 5-6, pp. 503-510, 1998.

[105] M. Hanna, "Tribological evaluation of aluminum and magnesium sheet forming at high temperatures", Wear, vol. 267, no. 5-8, pp. 1046-1050, 2009.

[106] M. Merklein, A. Kuppert and M. Geiger, "Time dependent determination of forming limit diagrams", CIRP Annals, vol. 59, no. 1, pp. 295-298, 2010. Available: 10.1016/j.cirp.2010.03.001.EN ISO 12004-2:2008: Metallic materials, Sheet and strip, Determination of forming-limit curves, 2008

[107] J. Kelly, J. Sullivan, A. Burnham and A. Elgowainy, "Impacts of Vehicle Weight Reduction via Material Substitution on Life-Cycle Greenhouse Gas Emissions", Environmental Science & Technology, vol. 49, no. 20, pp. 12535-12542, 2015. Available: 10.1021/acs.est.5b03192 [Accessed 8 June 2020].

[108] International Council on Clean Transportation (ICCT) White Paper, 2010, Size or Mass? The Technical Rationale for Selecting Size as an Attribute for Vehicle Efficiency Standards

[109] IHS Automotive Supplier Business report, Weight Reduction in Automotive Design and Manufacture, 2014.

[110] J. A. Schey, Tribology in Metalworking : Friction, Lubrication and Wear. Metals Park: American Society for Metals, 1984.

[111] T. Kobayashi, E. Suzuki and Y. Uchiyama, "Pin-on-disk type wear testing device", US4966030A, 1989.

[112] "BN Lubricoat and Lubricoat Blue - ZYP Coatings Inc.", ZYP Coatings Inc., 2022. [Online]. Available: https://www.zypcoatings.com/top-selling-boron-nitride-coatings/bn-lubricoat-lubricoat-blue/. [Accessed: 13- Apr- 2021].

[113] Uflyand, Ya. S.,1948, Wave Propagation by Transverse Vibrations of Beams and Plates, PMM: Journal of Applied Mathematics and Mechanics, Vol. 12, 287-300

[114] B. Osborne, "Why Use a Surface Finish Chart? | Metal Surface Finish", Metal Cutting Corporation. [Online]. Available: https://metalcutting.com/knowledge-center/why-use-a-surface-finish-chart/. [Accessed: 13- Apr- 2021].

[115] "Friction - Friction Coefficients and Calculator", Engineeringtoolbox.com. [Online]. Available: https://www.engineeringtoolbox.com/friction-coefficients-d_778.html. [Accessed: 13- Apr- 2021]. “MSDS Lubricant datasheet Forge Ease AL278,” Fuchs Lubricants Co.

[116] "RENOFORM 25 ALWF | Metal processing | FUCHS LUBRICANTS CO. (United States)", Fuchs.com. [Online]. Available: https://www.fuchs.com/us/en/product/product/132832-renoform-25-alwf/. [Accessed: 13- Oct- 2021].https://www.edro.com/wp-content/uploads/2020/06/CARBON-X_EN_EDRO1.pdf

[117] "Report on the 23rd Committee on Reference Materials (REMCO) Meeting of the International Organization for Standardization (ISO), ISO Headquarters, 15–17 May 2000, Geneva, Switzerland", Chemistry International -- Newsmagazine for IUPAC, vol. 22, no. 6, 2000. Available: 10.1515/ci.2000.22.6.167. Metallic materials. Geneva: International Organization for Standardization, 2008.

[118] "VHT Flameproof™ Coating -- High Heat Coating", VHT Very High Temperature Flameproof Automotive Paint. [Online]. Available: https://www.vhtpaint.com/high-heat/vht-flameproof-coating. [Accessed: 13- Apr- 2021].

[119] N. Wang, A. Ilinich, M. Chen, G. Luckey and G. D'Amours, "A comparison study on forming limit prediction methods for hot stamping of 7075 aluminum sheet", International Journal of Mechanical Sciences, vol. 151, pp. 444-460, 2019. Available: 10.1016/j.ijmecsci.2018.12.002.

[120] F. Barlat and K. Lian, "Plastic behavior and stretchability of sheet metals. Part I: A yield function for orthotropic sheets under plane stress conditions", International Journal of Plasticity, vol. 5, no. 1, pp. 51-66, 1989. Available: 10.1016/0749-6419(89)90019-3.

[121] F. Barlat et al., "Plane stress yield function for aluminum alloy sheets—part 1: theory", International Journal of Plasticity, vol. 19, no. 9, pp. 1297-1319, 2003. Available: 10.1016/s0749-6419(02)00019-0.

[122] Garrett, R.P., Lin, J., Dean, T.A., Solution Heat Treatment and Cold Die Quenching in Forming AA 6xxx Sheet Components: Feasibility Study, Advanced Materials Research, Vols 6-8 (2005) pp. 673-680.

[123] Garrett, R.P., Lin, J., Dean, T.A., I.J.Plast., 21, 1640–1657, 2005.

[124] Lin, J., Dean, T.A., Garrett, R.P., Foster, A., Process for Forming Metal Alloy Sheet Components, WIPO, WO2008059242, Priority Date 14.11.2006, Published 22.05.2008.

[125] Foster, A., Dean, TA.., Lin, J., Process for Forming Metal Alloy Sheet Components, WIPO, WO 201032002, Priority Date 19.09.2008, Published 25.03.2010.

[126] Foster, A., Dean, T.A., Lin, J., Process for forming aluminium alloy sheet components, CIPO, CA2737800C, Priority Date 25.03.2010, Published 07.12.2016.

[127] DiCecco S, Butcher C, Worswick M, Chu C, Boettcher E and Shi C, Application of Time and Position Dependent Localized Necking Criteria to High Strength Aluminum Alloys at Elevated Temperatures, 2016 Ohlstadt, Germany Forming Technology Forum

[128] DiCecco S, Di Ciano M, Butcher C and Worswick M, Numerical and experimental investigation of the formability of AA6013-T6, 2017 J. Phys. Conf. Ser. 896 1 012114

[129] DiCecco, S., Di Ciano, M., Butcher, C., Worswick, M., Die-Quench Formability of a Developmental AA7xxx Aluminum Alloy Sheet, Proceedings International Deep Draw Research Group (IDDRG) 37th International Conference, Waterloo, Ontario, June 3-7, 2018.

[130] George, R., Cheong, K., DiCecco, S., Private Communication, 2021.

[131] “Aluminum 7075-T6; 7075-T651", Matweb.com, 2022. [Online]. Available: https://www.matweb.com/search/datasheet.aspx?matguid=4f19a42be94546b686bbf43f79c51b7d. [Accessed: 30- Apr- 2021].

[132] T. Rahmaan, C. Butcher and M. Worswick, "Constitutive Response of AA7075-T6 Aluminum Alloy Sheet in Tensile and Shear Loading", Conference Proceedings of the Society for Experimental Mechanics Series, pp. 115-122, 2016. Available: 10.1007/978-3-319-42028-8_14 [Accessed 1 February 2022].

[133] J. Noder, R. George, C. Butcher and M. Worswick, "Friction characterization and application to warm forming of a high strength 7000-series aluminum sheet", Journal of Materials Processing Technology, vol. 293, p. 117066, 2021. Available: 10.1016/j.jmatprotec.2021.117066.

[134] Kurukuri, S., Worswick, M., Bardelcik, A., Mishra, R. and Carter, J., 2014. Constitutive Behavior of Commercial Grade ZEK100 Magnesium Alloy Sheet over a Wide Range of Strain Rates. Metallurgical and Materials Transactions A, 45(8), pp.3321-3337.

[135] Zerilli, F. and Armstrong, R., 1994. Constitutive relations for the plastic deformation of metals. AIP Conference Proceedings,.Zheng, K., Dong, Y., Zheng, D., Lin, J. and Dean, T., 2019. An experimental investigation on the deformation and post-formed strength of heat-treatable aluminium alloys using different elevated temperature forming processes. Journal of Materials Processing Technology, 268, pp.87-96.

[136] G. R. COWPER and P. S. SYMONDS, “Strain-hardening and strain-rate effects in the impact loading of cantilever beams,” 1957.